

RARE EVENT SEARCHES WITH THE DARKSIDE-50 DETECTOR

A Dissertation Presented to
the Faculty of the Department of Physics
University of Houston

In Partial Fulfillment
of the Requirements for the Degree
Doctor of Philosophy

By
Parth N. Singh
December 2018

RARE EVENT SEARCHES WITH THE DARKSIDE-50 DETECTOR

Parth N. Singh

APPROVED:

Prof. Ed Hungerford, Chairman
Department of Physics

Prof. Andrew Renshaw
Department of Physics

Prof. Lawrence Pinsky
Department of Physics

Prof. Gemunu Gunaratne
Department of Physics

Prof. Randall Lee
Department of Chemistry

Dean, College of Natural Sciences and Mathematics

Acknowledgements

Dissertations are rarely realized by the effort of a single individual. There are several people I would like to thank who played major roles in the production of this particular one.

My advisor, Ed Hungerford, is an absolute inspiration and an exemplary scientist. He has always been extremely supportive, and an endless source of insight. Observing his work ethic has been energizing. I am also extremely fortunate to have worked directly with Andrew Renshaw. He is an extraordinary physicist, from whom I have learned an incredible amount about physics and analysis methods. Without him, this work would not have been possible. Their careful criticism has greatly improved the quality of my work and this dissertation.

The work on cosmogenic backgrounds was realized because of the collaboration with Anton Empl. He has been an exceptionally patient mentor and friend. I am indebted to him for his guidance.

Many many thanks to Paolo Agnes, not only for his thorough advice through the years but also for his work on G4DS, without which, the analyses presented in Chapters 5 and 6 could not have been accomplished. He was always available to help, and discussions with him have been very fruitful. I would also like to thank him for his careful reading of this document.

Masayuki Wada has been able to answer all of my questions about DarkSide-50 throughout my journey, and his mastery of data analysis has been a blessing for me. I would also like to thank him for getting me acquainted with the analysis of DarkSide-50 data. Alden Fan and Yann Guardincerri were particularly helpful when I was getting started with DarkArt. Peter Meyers' constructive comments have been extremely beneficial to the evolution of my work, especially the study on cosmogenic neutron backgrounds. I must thank Xinran Li and Valerio Ippolito for their extensive help in utilizing and de-bugging the S2-only analysis code.

I would like to thank my committee members for their time and participation in my

professional development as a scientist. A big thank you to Lawrence Pinsky for being a constant source of encouragement. He was also directly responsible for introducing me to the DarkSide experiment.

Many thanks to a number of close friends that eased the journey of graduate school. I truly cherish some of these precious friendships.

My family has consistently supported and encouraged me on so many different levels. For their inexhaustible love, I am indebted. My father helped me realize my passion for physics, while my mother has imparted invaluable wisdom to me. Conversations with my sister are directly responsible for my growth as a holistic individual. My uncle and aunt have always made Houston feel like home, for which I am grateful.

RARE EVENT SEARCHES WITH THE DARKSIDE-50 DETECTOR

An Abstract of a Dissertation
Presented to
the Faculty of the Department of Physics
University of Houston

In Partial Fulfillment
of the Requirements for the Degree
Doctor of Philosophy

By
Parth N. Singh
December 2018

Abstract

While the Standard Model of particle physics has exhibited great success at describing much observed phenomena over the years, vast astrophysical evidence exists suggesting most of the matter in the universe is non-luminous and does not fit within the Standard Model.

There is consensus among cosmologists that most of this missing matter, referred to as dark matter, is composed of particles which are non-baryonic. Two of the leading candidates for this dark matter are Weakly Interacting Massive Particles (WIMPs) and axions. Dark matter has eluded laboratory detection, primarily due to the fact that it is predicted to be very weakly interacting. Several experiments have been built to detect a nucleus recoiling from a WIMP colliding with a known atom.

Liquid noble gas detectors have demonstrated, that using novel background rejection techniques, rare events like WIMP recoils could be detected. DarkSide-50 (DS-50) is one such detector using liquid argon (LAr) technology. Over the years of operation in a background-free mode, DS-50 has not observed any WIMP events but has produced some competitive limits on WIMP-nucleon interaction cross sections for liquid argon detectors.

The low-background levels of DS-50 present the possibility to search for other hypothesized physics phenomena which are also predicted to rarely occur. Two of which are investigated in this dissertation.

One such search presented here is the hunt for neutrino-less double electron capture on an isotope of argon, ^{36}Ar . The observation of such a decay would signify a substantial increase in our understanding of neutrinos, further providing a window of inspection into the observed matter anti-matter asymmetry in the universe.

Yet another search presented is the interaction of axions, coming from the Sun, with electrons in the LAr. An observation of such an interaction would validate the theory that solves the strong CP problem of the Standard Model, simultaneously providing evidence of the existence of a dark matter candidate.

Contents

1	Dark Matter	1
1.1	Brief History of Dark Matter	1
1.2	Dark Matter Candidates	8
1.2.1	Weakly Interacting Massive Particles (WIMPs)	8
1.2.2	Other Theories	12
1.3	WIMP Recoil Spectra	13
1.3.1	WIMP-Nucleon Scattering	13
1.3.2	Detector Sensitivity	18
1.4	WIMP Detection Experiments	20
1.4.1	Indirect Detection	20
1.4.2	Direct Detection	20
1.4.3	Current Status	22
2	DarkSide-50	24
2.1	Liquid Argon (LAr)	24
2.1.1	Scintillation Mechanism	24
2.1.2	Underground Argon (UAr)	27
2.2	Dual Phase LAr Time Projection Chamber (LAr TPC)	28
2.3	PMT Calibration Procedure and Analysis	32
2.3.1	Conventional Methods	32
2.3.2	Model-Independent Method	33
2.4	Veto Detectors	44
2.4.1	Liquid Scintillator Veto (LSV)	45

2.4.2	Organic Liquid Scintillator	46
2.4.3	Lumirror reflector	48
2.4.4	LSV PMTs	49
2.4.5	Calibration system	50
2.4.6	Water Cherenkov Veto	50
2.4.7	Tyvek reflector	53
2.4.8	WCV photomultiplier tubes	53
2.5	G4DS - The DarkSide Monte Carlo Tool	55
3	Background Sources	58
3.1	Radiogenic Backgrounds	58
3.1.1	^{39}Ar	59
3.1.2	^{85}Kr	60
3.1.3	^{238}U	61
3.1.4	^{235}U	63
3.1.5	^{232}Th	64
3.2	Cosmogenic Backgrounds	64
3.2.1	Neutron Production Mechanisms	65
3.2.2	The FLUKA Code	67
3.2.3	Physics Models in FLUKA	67
3.2.4	Physics Related User Options	69
3.3	Cosmogenic Background Simulation at LNGS	70
3.3.1	Muon Radiation Field	70
3.3.2	Muon-induced Secondaries	74
3.3.3	Connection of Simulation to Measured Muon Event Flux	76
3.4	Validation	77
3.4.1	The Borexino Experiment	77
3.5	Cosmogenic Neutron Background for DS-50	79
3.5.1	Simulation Procedure	79
3.5.2	Results	83

4	WIMP Searches with DS-50	89
4.1	Atmospheric Argon (AAr) 50 Day Search	89
4.2	Underground Argon (UAr) 70 Day Search	92
4.2.1	Basic Quality Cuts	93
4.2.2	TPC Cuts	94
4.2.3	Veto Cuts	95
4.2.4	Results	96
4.3	UAr 500 Day Blind Analysis	99
4.3.1	Data Set	100
4.3.2	Blinding Scheme	100
4.3.3	Cuts	100
4.3.4	Background Modeling	102
4.3.5	Unbinding and Results	103
4.4	Low Mass WIMP Search	106
4.4.1	S2-Ionization Signals	106
4.4.2	Ionization Yield	107
4.4.3	Results	108
4.5	Search for Sub-GeV Dark Matter-Electron Scattering	111
4.5.1	Electron Recoil Scale	111
4.5.2	Results	112
5	Neutrino-less Double Electron Capture on ^{36}Ar	115
5.1	Neutrino : Majorana or Dirac Particle?	115
5.2	^{36}Ar	120
5.2.1	Search in DS-50	121
5.2.2	Backgrounds	121
5.2.3	Extracting a Limit - Preliminary Results	130
5.2.4	Uncertainties	132
6	Search for Solar Axions	137
6.1	Motivation	137

6.2	Solar Axions	138
6.2.1	Axio-Electric Effect	140
6.3	S1 Sensitivity Check	142
6.3.1	Rate in DS-50	142
6.3.2	Data Set and Cuts	144
6.3.3	Spectral Fitting	146
6.3.4	Preliminary Results	147
6.3.5	Uncertainties	149
6.4	S2-Based Search	151
6.4.1	Backgrounds	151
6.4.2	The Electron Recoil Energy Scale	151
6.4.3	Profile Likelihood Fit	152
6.4.4	Preliminary Results	155
6.4.5	Possible Improvements	157
7	DarkSide : The Future	160
7.1	DarkSide-20k	160
7.1.1	Detector Overview	160
7.1.2	Backgrounds	161
7.1.3	Underground Argon	162
7.1.4	Sensitivity	162
7.2	Cosmogenic Background Simulation	163
7.2.1	Prompt Background	165
7.2.2	Results	166
8	Summary and Future Outlook	168
	Bibliography	171

Chapter 1

Dark Matter

Despite the recent progress in our understanding of the Standard Model, there are several open problems in particle physics and cosmology. One of these is the mysterious nature of dark matter. There is almost unanimous agreement between astronomers, cosmologists and particle physicists that most of the mass in the universe is non-luminous or dark. In fact, this “missing matter” accounts for more than 80% of the matter content and 27% of the universe’s energy budget while the remaining 67% is dark energy and is not the topic of this dissertation. The evidence for these estimates mostly comes from gravitational effects. The properties of what constitutes this dark matter is yet unknown. A step towards understanding the essence of dark matter is to detect its interactions with known particles well described by the Standard Model. A variety of experiments have been set up in the last few years to try and detect these elusive particles which may compose dark matter. This chapter covers an introduction to dark matter and WIMPs in particular.

1.1 Brief History of Dark Matter

Astronomical Evidence

The first major evidence which suggested that dark matter may be much more abundant

than previously thought, was provided by Fritz Zwicky. He calculated the velocity dispersion of galaxies in the Coma cluster by measuring the red shift and subsequently used the virial theorem to compute the average mass of the individual galaxies [1]. He was able to combine these results with the mean luminosity measurements and obtain a mass to luminosity ratio which was surprisingly much larger than the expected value of 1. Zwicky then hypothesized the existence of a missing, non-luminous component of matter and coined the term “dunkle Materie” which translates to Dark Matter.

The need for a dark matter component was further established when Vera Rubin measured the rotation curves of a number of spiral galaxies [2]. She measured the rotation curve by comparing the redshift of the 21 cm hydrogen line from stars on the opposite sides of the galaxy. If the galaxy were composed of entirely luminous matter, Newtonian dynamics indicates that the stars at a distance r from the center of the galaxy should approximately obey the following velocity function :

$$v(r) = \begin{cases} \sqrt{\frac{4}{3}\pi G \rho r} & \text{if } r < R \\ \sqrt{\frac{4}{3}\pi G \rho R^3 / r} & \text{if } r > R \end{cases}$$

where R is radius of the central bulge of the galaxy and ρ is the density of the bulge. As seen in Fig 1.1, the component labeled ‘disk’ shows the velocity decrease $\propto 1/r^2$ at large radii.

Rubin observed that the rotation curve was flat even at very large distances from the bulge of the galaxy. It is possible to resolve this discrepancy by introducing a component of dark matter as a spherical halo where its mass density falls off as $1/r^2$. Of course the true profile of the halo is not known, but some very good models exist [4]. One such model is the Navarro-Frenk-White profile [5] which suggests that the mass density of the halo is given by :

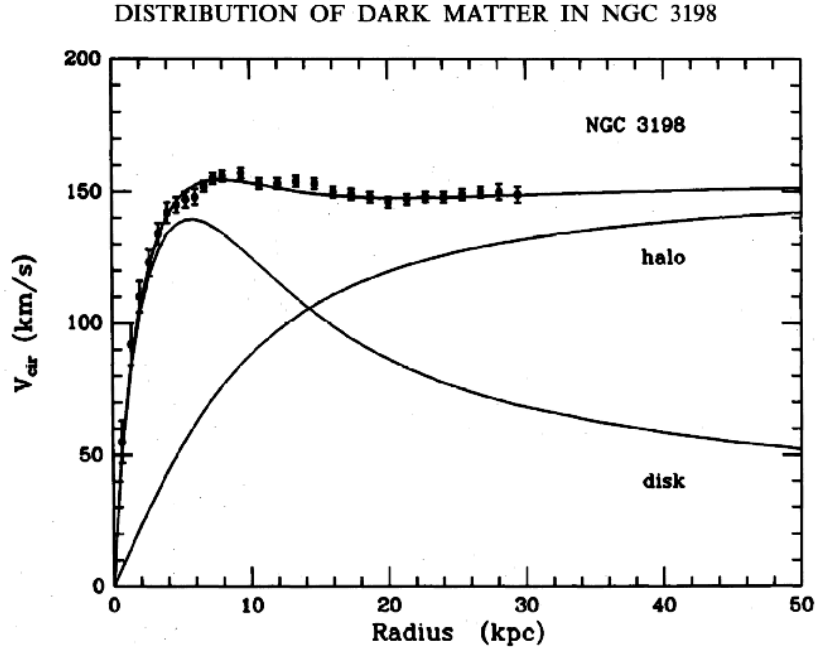


Figure 1.1: Rotation curve for galaxy NGC 3198. It shows the expected rotation velocity (labeled as “disk“) if no dark matter were present and the component arising from dark matter (labeled as “halo“). Figure taken from [3]

$$\rho(r) = \frac{\rho_0}{\frac{r}{R_s} \left(1 + \frac{r}{R_s}\right)^2} \quad (1.1)$$

where ρ_0 and R_s (scale radius) are parameters which depend on the particular halo in consideration.

Massive objects (like galaxy clusters) are able to warp space-time in their vicinity, as is known from the results of General Relativity. This causes bending of light rays around the object and the phenomenon is known as gravitational lensing. It primarily involves the bending of light rays, as observed from a distant source behind a massive object. The image of the source could be deformed or distorted into rings or arcs or it could produce multiple images of the same source. An example of such an observation is shown in Figure 1.2

Observations from the Bullet Cluster provide further evidence that there is a missing component of matter which is non-luminous. The Bullet Cluster is composed of two galaxy



Figure 1.2: Evidence of gravitational lensing from Abell 2218 which is a rich galaxy cluster composed of thousands of individual galaxies. Multiple distorted images of the same galaxies can be identified by comparing the shape of the galaxies and their colour. In addition to the giant arcs, many smaller arclets have been identified. Figure and caption from [6]

clusters that collided with each other. X-ray photography can be used to determine the center of mass in both galaxies, as the mass is dominated by interstellar gas and stars. Gravitational lensing measurements provide an independent estimate of the center of mass of all matter (luminous and non-luminous). These two estimates differ from each other at the 8σ level implying the existence of a far more abundant but weakly interacting, non-baryonic, non-luminous matter [7].

Cosmology

Measurements of the cosmic microwave background (CMB) provide some of the strongest evidence for the existence of dark matter. The Big Bang model suggests that at the earliest stage, the universe went through a period of extremely rapid expansion (\sim a factor of 10^{27} over 10^{-32} s [10]). This is known as inflation, an idea first introduced by Alan Guth [11] as a solution to the horizon [12] and flatness problems [13]. At this stage, the universe was composed of a dense, hot plasma of ionized particles. This plasma was opaque since photons

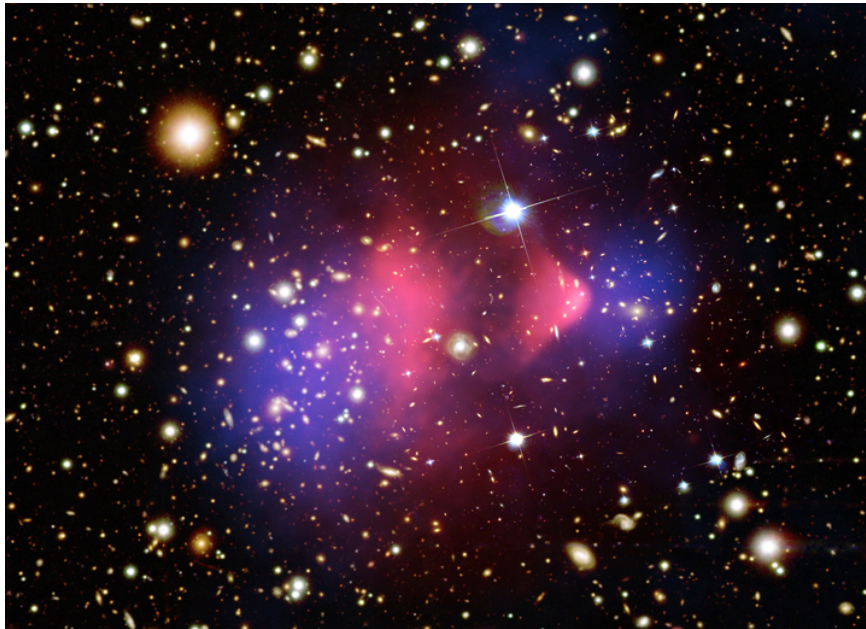


Figure 1.3: Hot gas detected by the Chandra X-ray observatory is seen as two pink clumps and contains most of the baryonic matter in the two clusters. The bullet-shaped clump on the right is the gas from one cluster which passed through the gas originating from the other cluster. The blue areas depict where most of the mass (determined by gravitational lensing) lies. It clearly shows that normal matter (pink) is separated from the majority of the matter (blue). Figure taken from [8].

in this sea of charged particles had extremely short mean free paths. Thus the photons were coupled strongly to the baryons. This compressed photon-baryon fluid fell into residual gravitational wells from inflation, and expanded as the pressure of the fluid increased from higher electromagnetic interaction rates. As the universe cooled, the temperature dropped below the atomic ionization energy threshold, and the ionized plasma began to form neutral atoms (mostly hydrogen). This process called recombination, occurred 380,000 years after the Big Bang. The photons were able to free stream until today, and this relic radiation is referred to as the CMB. The temperature of the CMB today is estimated to be 2.73 K [14].

The CMB is mostly isotropic with small anisotropies being driven by temperature fluctuations in the early universe. This demonstrates that the universe is primarily homogeneous. The intensity and size of the temperature fluctuations are characterized by the particle physics during the early Universe as it was expanding and cooling off. These temperature

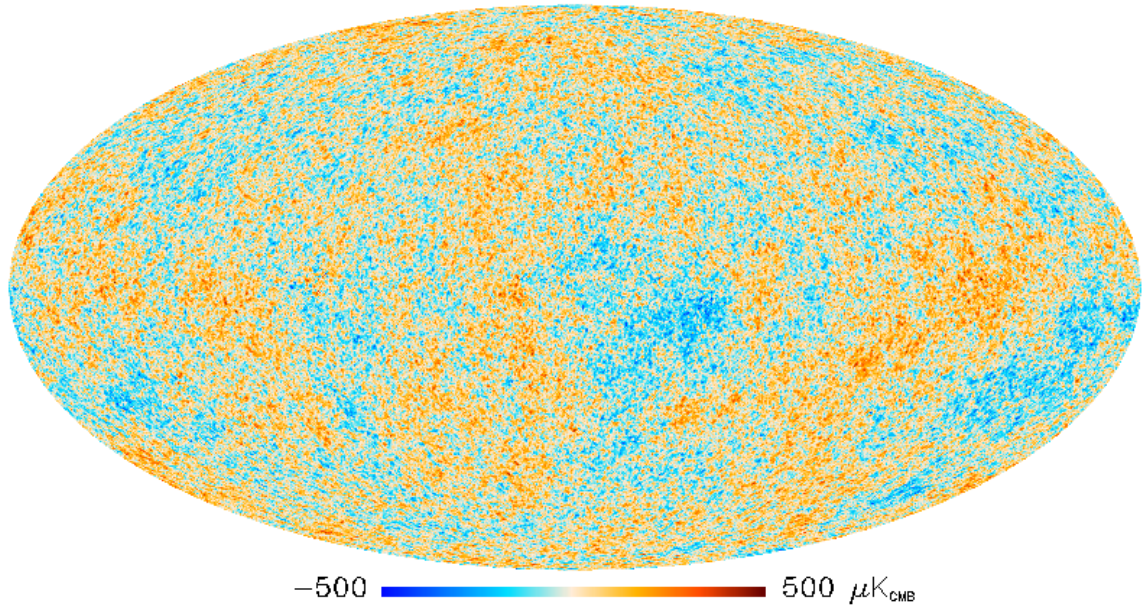


Figure 1.4: Measurement of the CMB temperature from the Planck experiment shown by a full sky temperature map. Figure taken from [9].

variations can be represented by the power spectrum of the CMB. This power spectrum is a measure of the deviation of each point from the mean temperature, when decomposed into spherical harmonics. The amplitude of the power spectrum at different values of the multipole moment, ℓ , can be seen in Figure 1.5. It gives a measure of the anisotropies in the CMB which permits the calculation of the abundance of different species of particles in the universe after they are fixed at the time of freeze out. Since dark matter is not expected to interact with photons directly, baryonic matter couples to photons much more strongly. This implies that anisotropies in the CMB are primarily driven by fluctuations in the baryonic density.

If the universe is flat, the location of the first peak in Figure 1.5 should be at $\sim 1^\circ$ which is equivalent to $\ell \sim 200$ and measurements from The WMAP and Planck experiments confirm that the Universe is indeed flat [9, 15]. Furthermore, the relative amplitudes of the peaks in the power spectrum provide information on the amount of baryonic and dark

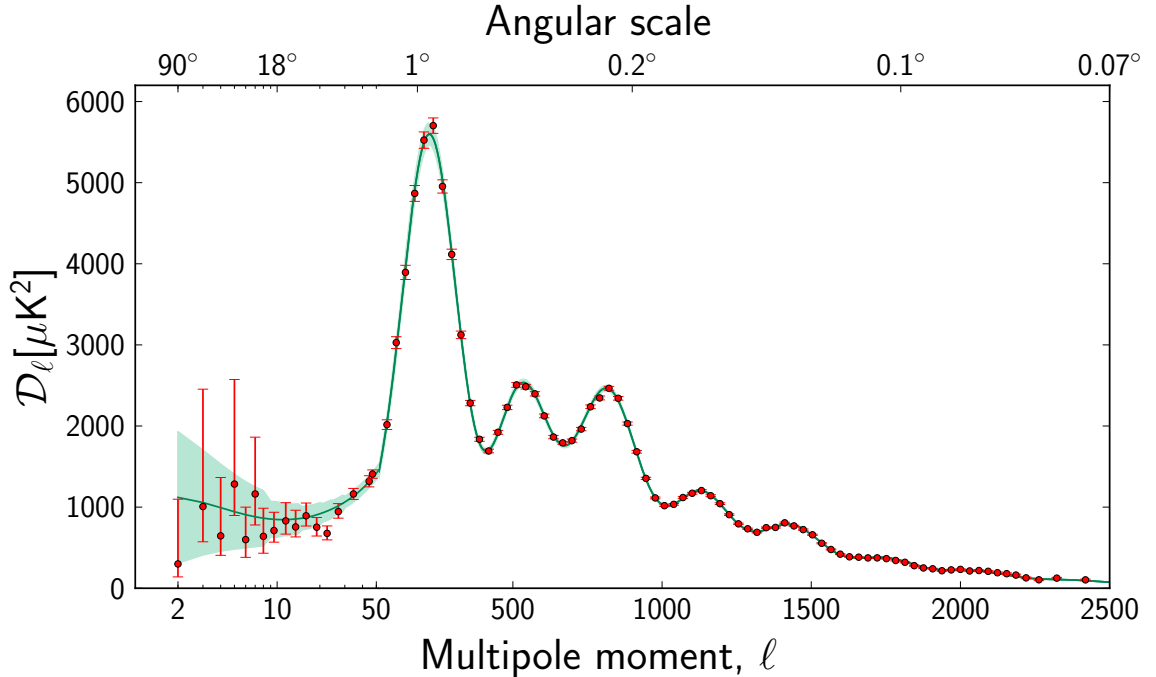


Figure 1.5: Temperature angular power spectrum of the primary CMB from the Planck Collaboration, showing a precise measurement of 7 acoustic peaks that are fit well by a 6 parameter Λ -CDM model. The shaded area around the best fit curve represents the sample variance. The error bars on individual points also include cosmic variance. The x axis is logarithmic up to $\ell = 50$, and linear beyond. The vertical scale is $\ell(\ell+1)/2\pi$. Figure taken from [9].

matter in the universe. The peaks in Figure 1.5 are referred to as acoustic peaks since they are related to the density of sound waves of a given wavelength when the universe became transparent to the waves. The first acoustic peak (at $\ell \sim 200$) corresponds to the compression of the plasma. The size of this peak (and subsequent odd numbered peaks) depends on the mass of all baryonic matter in the universe. The second peak corresponds to the rarefaction of the plasma, but is in fact a harmonic of the first peak. The size of this peak (and subsequent even-numbered peaks) increases with the expansion of plasma due to acoustic oscillations and hence does not depend on the content of baryonic mass in the universe. Thus given the dependence of the amplitude of first peak on the quantity of baryonic mass and the independence of the amplitude of the second peak, the ratio of the two amplitudes provides a measure of the total baryonic mass content of the universe.

The data obtained from the WMAP and Planck experiments are fit with a 6 parameter model (Λ -CDM) which provides the following results; $\Omega_b = 0.049$, $\Omega_{DM} = 0.268$, and $\Omega_\Lambda = 0.683$. Here $\Omega_i = \frac{\rho_i}{\rho_{cr}}$ and ρ_i is the physical density and ρ_{cr} is the critical density necessary for a flat universe given by $\rho_{cr} = \frac{3H_0^2}{8\pi G}$. In other words, the fit determines that a model of the universe where the energy budget is factored into 69.3% dark energy, 26.8% dark matter and 4.9% baryonic matter, is favored.

1.2 Dark Matter Candidates

1.2.1 Weakly Interacting Massive Particles (WIMPs)

The very first WIMPs were considered as massive Majorana or Dirac neutrinos with masses in the range of a few GeV to a TeV. These candidates were soon ruled out. Other simple candidates for WIMPs, which require the least amount of addition to the Standard Model, are also not particularly favorable. These “vanilla” WIMPs could include scalar interactions via Higgs exchange or vector interactions via Z-exchange. For example in the latter case, the WIMP would interact with a nucleon via a Z-boson exchange in the simplest tree level Feynman diagram. Models predict the cross section for the Higgs interaction to be $\sim 10^{-43}$ cm² while $\sim 10^{-38}$ cm² for the Z-exchange. The Z-mediated interactions for WIMPs with masses of ~ 100 GeV have mostly been excluded.

A more promising candidate for WIMPs comes from the introduction of supersymmetry (SUSY). SUSY was first hypothesized in particle physics to solve the naturalness problem with the Higgs boson, at the electroweak scale. SUSY also provides a solution to the hierarchy problem, while simultaneously seems to improve the unification of the coupling constant at the Grand Unified Theory (GUT) scale. Furthermore, it could help unify gravity with the other fundamental forces. SUSY introduces for each of the Standard Model particles a complementary partner. That is for every boson there is a supersymmetric fermionic

partner and for every known fermion there is a supersymmetric bosonic partner. SUSY requires a new discrete symmetry, R-parity. The standard model particles have R-parity = 1 while their superpartners have R-parity = -1. Any interaction between these particles must conserve the R value. This guarantees that the lightest supersymmetric particle (LSP) will be stable. The minimal extension of the standard model in SUSY, also referred to as Minimal Supersymmetric Standard Model (MSSM), typically identifies the neutralino as the LSP. The neutralino is a linear combination of the supersymmetric partners of the photon, Z^0 , and the Higgs boson. With a particular SUSY model, the cross section for the neutralino annihilation to lighter particles can be calculated, and the cosmological mass density can be obtained. The solution to the naturalness problem via SUSY requires the mass scale to be of the order of the weak scale and hence the neutralino would have, at most, electroweak interactions. Thus the cosmological neutralino abundance is expected to be $\mathcal{O}(1)$ and can therefore account for dark matter in the halo.

WIMP Relic Density

In the early universe, when the temperature was sufficiently high, massive dark matter was in a state of thermal equilibrium with ordinary matter. As the universe expanded, the temperature dropped and lighter particles did not have sufficient kinetic energy to produce dark matter particles. The gas of dark matter particles became less dense and hence it became more improbable for the particles to find each other to annihilate. The co-moving number density then approached a “freeze-out” state, which is now referred to as the dark matter relic density. The time evolution of the dark matter density can be described by the Boltzmann equation as follows [16] :

$$\frac{dn}{dt} = -3Hn - \langle \sigma_A v \rangle (n^2 - n_{\text{eq}}^2) \quad (1.2)$$

Here n is the number density of the dark matter particle (χ), n_{eq} is the dark matter number density in thermal equilibrium, H is the Hubble constant and $\langle \sigma_A v \rangle$ is the thermally average self-annihilation cross section. The term $-3Hn$ represents the dilution of the gas from the expansion. The n^2 term represents the process of annihilation of dark matter particles to

generate standard model particles ($\chi\chi \rightarrow \text{SM SM}$). The reverse process, which creates dark matter particles, is represented by the remaining term n_{eq}^2 . A change of variables can be employed in equation 1.2 in order to simplify the differential equation as follows :

$$Y = n/s$$

$$x = m_\chi/T$$

Where m_χ is the particle mass and T is the temperature. s is the time dependent entropy density of the universe which can be represented as $s = \frac{2\pi^2 g_*}{45} T^3$ where g_* is the number of relativistic degrees of freedom. It is possible to combine equation 1.2 with the Friedmann equation which relates the Hubble parameter H to the energy density of the universe ρ :

$$H^2 = \frac{8\pi G}{3} \rho = \frac{8\pi}{3M_p^2} \rho \quad (1.3)$$

Here G is the gravitational constant and M_p is the Planck mass. Thus using equations 1.2 and 1.3 the following relation for the number density is obtained :

$$\frac{dY}{dx} = -\sqrt{\frac{\pi}{45G}} \frac{g_*^{1/2} m_\chi}{x^2} \langle \sigma_{Av} \rangle (Y^2 - Y_{\text{eq}}^2) \quad (1.4)$$

This equation (1.4) must be solved numerically. At very later times, the temperature is well below m_χ , $x \gg 1$ and $dY/dt \rightarrow 0$ and implies that Y is constant. Figure 1.6 shows one such numerical solution for a particle with a mass of 100 GeV.

The relic density can be analytically obtained. A convenient definition of a dimensionless variable λ is introduced.

$$\lambda = \sqrt{\frac{\pi}{45G}} g_*^{1/2} m_\chi \langle \sigma_{Av} \rangle \quad (1.5)$$

At late times, Y_{eq} falls exponentially and therefore equation 1.4 can be written as :

$$\frac{dY}{dx} \simeq -\frac{\lambda Y^2}{x^2} \quad (1.6)$$

which allows for analytical integration from freeze-out to the present time (where $x \rightarrow \infty$), thus leading to the following :

$$\frac{1}{Y_0} - \frac{1}{Y_f} \simeq \frac{\lambda}{x_f} \quad (1.7)$$

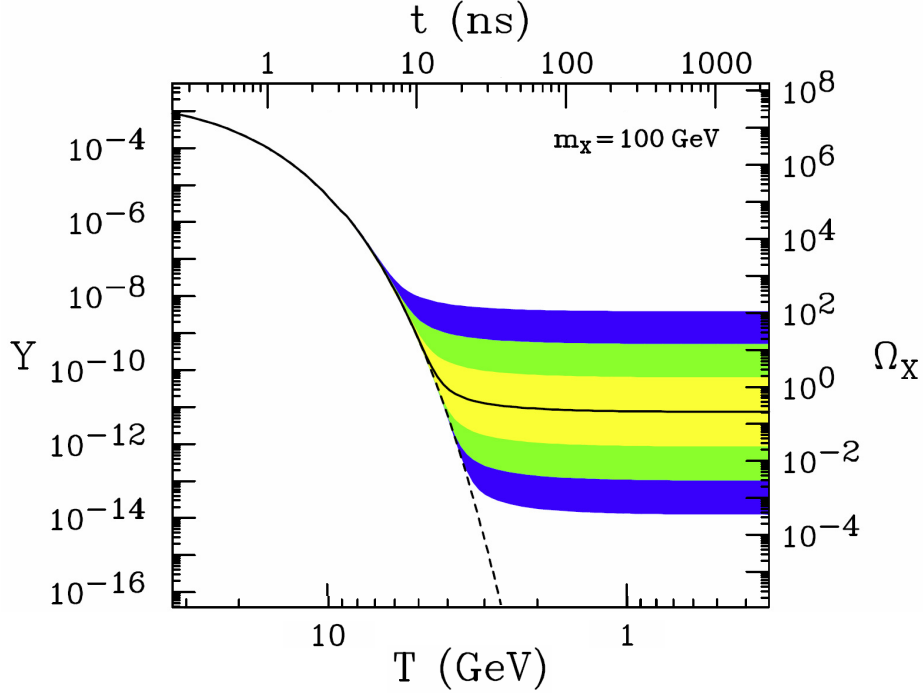


Figure 1.6: The co-moving number density Y (left,y-axis) and the resulting thermal relic density (right,y-axis) of a 100 GeV WIMP as a function of temperature T (bottom,x-axis) and time t (top, x-axis). The solid contour is for an annihilation cross section that yields the correct relic density, and the shaded regions represent cross sections that differ by 1,2 and 3 orders of magnitude from this value. The dashed line represents the number density of a particle that remains in thermal equilibrium. Figure taken from [17].

where Y_0 represents the present value of Y and Y_f represents the value of Y at freeze-out. Using the arguments presented in [17] which suggest that x_f does not vary much with particle mass and can be approximated as $x_f \sim 20$, and the fact that the abundance at freeze-out is much larger than the present abundance, equation 1.7 becomes :

$$Y_0 \simeq \frac{x_f}{\lambda} \quad (1.8)$$

The relic dark matter density can then be expressed as :

$$\Omega_{\text{DM}} = \frac{m_\chi s_0 Y_0}{\rho_{\text{cr}}} \simeq \frac{m_\chi s_0 x_f}{\rho_{\text{cr}} \lambda} = \sqrt{\frac{45G}{\pi}} \frac{s_0 x_f}{\rho_{\text{cr}} g_*^{1/2} \langle \sigma_{A\nu} \rangle} \quad (1.9)$$

Here s_0 is the present day entropy density. Using the lowest order approximation which suggests that the relic density is inversely proportional to $\langle \sigma_{A\nu} \rangle$ but insensitive to m_χ , and

subsequently substituting numerical values for the constants, the following is obtained :

$$\Omega_{\text{DM}} \simeq \frac{10^{-39} \text{cm}^2}{\langle \sigma_A v \rangle} \quad (1.10)$$

The dark matter relic density, represented by Ω_{DM} , is observed to 0.268, implying from equation 1.10, that the cross section needs to be of the order of the weak scale ($\sim 10^{-39} \text{cm}^2$). This is known as the WIMP miracle. It is “miraculous” since the cross section in equation 1.10 comes essentially from the age of the universe and there is no a priori reason why the age of the universe would have much to do with electroweak physics. This coincidence advocates that a new, undiscovered particle with electroweak interactions could exist and would provide the correct relic density, and hence would be a natural dark matter candidate.

1.2.2 Other Theories

There are several other candidate theories that attempt to explain the “missing matter” problem. Another class of well motivated particles, axions, are discussed in Chapter 6. Yet another candidate for dark matter particles are sterile neutrinos . This could be a fourth flavour of a neutrino which does not couple to other leptons other than indirectly by oscillating into one of the active neutrino flavours. It would be a right-handed neutrino and possibly account for some of the dark matter in the universe [18]. Many more exotic candidate particles have been hypothesized [19]. There are also other theories which modify gravity to explain the observations listed in Section 1.1; these include MoND (Modified Newtonian Dynamics) [20] and the description of gravity as an emergent phenomenon [21, 22]. It is worth mentioning that amongst the vast number of proposed solutions, only WIMPs and axions have survived extended theoretical scrutiny. Neither of these two candidates were invented to solve the dark matter problem. They were hypothesized to remedy other problems in particle physics and only later was it realized that they could be natural dark matter candidates.

1.3 WIMP Recoil Spectra

1.3.1 WIMP-Nucleon Scattering

The fundamental process involved in WIMP-nucleon scattering is WIMP-quark scattering. An effective WIMP-nucleon scattering cross section can be obtained by summing over the quarks present in a nucleon. In the limit of low momentum-transfer, the contribution of each individual nucleon can be summed coherently to obtain a WIMP-nucleus scattering cross section.

1.3.1.1 Cross Section

This section follows the discussions of [16, 23, 24]. The differential WIMP-nucleon cross section can be written as :

$$\frac{d\sigma_{\delta N}}{dq^2} = \frac{1}{\pi v^2} f_n^2 A^2 F^2(q^2) \quad (1.11)$$

Where q is the momentum transfer and f_n is the coupling of WIMPs to neutrons (and protons in the spin independent case) and this can be further simplified as ;

$$\frac{d\sigma_{\delta N}}{dq^2} = \frac{\sigma_0}{4m_r^2 v^2} F^2(q) \quad (1.12)$$

where $m_r = M_N M_\delta / (M_N + M_\delta)$ is the reduced mass of the WIMP and nucleus system. v is the relative WIMP-nucleus velocity. σ_0 is the total cross section independent of the form factor $F(q)$. The form factor represents the dependence of the interaction on the shape of the nucleus. Quantitatively it is the Fourier transform of the nucleon density. The following form factor parameterization is recommended [23] :

$$\begin{aligned} F(qr_n) &= 3 \frac{j_1(qr_n)}{qr_n} e^{-(qs)^2/2} \\ &= 3 \frac{\sin(qr_n) - qr_n \cos(qr_n)}{(qr_n)^3} e^{-(qs)^2/2} \end{aligned} \quad (1.13)$$

where

$$\begin{aligned}
r_n^2 &= c^2 + \frac{7}{3}\pi^2 a^2 - 5s^2 \\
c &= 1.23A^{1/3} - 0.60\text{fm} \\
a &= 0.52\text{fm} \\
s &= 0.9\text{fm}
\end{aligned}
\tag{1.14}$$

Here r_n is the nuclear radius, j_1 is a spherical Bessel function while a and s represent nuclear skin-thickness parameters.

For the spin-dependent case, Equation 1.12 is re-cast as [16] :

$$\begin{aligned}
\frac{d\sigma}{dq^2} &= \frac{8}{\pi v^2} G_F^2 \Lambda^2 J(J+1) F_S^2(q) \\
&= \frac{1}{\pi v^2} \left(\frac{g^2}{4M_W^2} \right)^2 4\Lambda^2 J(J+1) F_S^2(q)
\end{aligned}
\tag{1.15}$$

Here g is the fundamental electroweak coupling, M_W is the mass of the W boson and v is the relative WIMP-nucleus velocity. J represents the nuclear spin. Furthermore;

$$\Lambda^2 = \left[\frac{J(J+1) - L(L+1) + \frac{3}{4}}{2J(J+1)} \right]^2
\tag{1.16}$$

Examining equations 1.15 and 1.12 it is observed that the spin-independent part of the cross section scales with the number of nucleons, A^2 while the spin-dependent part is proportional to the nuclear angular momentum $(J+1)/J$. For many experiments that operate with heavy target nuclei such as argon, xenon and germanium the spin-independent component dominates.

1.3.1.2 Expected Recoil Energy Spectrum

The discussion here follows that of the classical paper by Lewin and Smith [23] with much reliance on the procedure developed in the dissertation [24]. Generally, the rate of interactions per unit mass of a target material of a particle with interaction cross section σ

can be represented by :

$$R = \frac{N_0}{A} \sigma v n \quad (1.17)$$

Where n is the number density of the incoming flux of the particles with velocity \mathbf{v} relative to the target with atomic mass A and N_0 represents Avogadro's constant. In order to compute the recoil-energy spectrum, it is imperative to consider the rate as a function of momentum transfer. It is typically standard to assume the WIMPs follow an isothermal, isotropic distribution. This may not be the accurate picture, but the uncertainties associated with this assumption are small compared to the uncertainties in the WIMP-nucleon cross section. At a given location, a simple Maxwellian velocity distribution such as :

$$f(\mathbf{v}, \mathbf{v}_E) = \exp\left(-\frac{(\mathbf{v} + \mathbf{v}_E)^2}{v_0^2}\right) \quad (1.18)$$

can be used to describe the velocity distribution of WIMPs. Here \mathbf{v} is the WIMP velocity relative to the Earth and \mathbf{v}_E is the Earth's velocity relative to the non-rotating halo of the galaxy and v_0^2 represents the most probable velocity and has an approximate value of 220 km/s. Then the differential number density is given by :

$$dn = \frac{n_0}{k} f(\mathbf{v}, \mathbf{v}_E) d^3v \quad (1.19)$$

where ;

$$n_0 \equiv \int_0^{v_{esc}} dn \quad (1.20)$$

$$k = \int_0^{v_{esc}} v^2 dv \int d\Omega_v f(\mathbf{v}, \mathbf{v}_E) \quad (1.21)$$

The velocity distribution has a cut off at the halo escape velocity (v_{esc}). Then, the interaction rate as a function of q^2 and WIMP velocity in the frame of reference of the target takes the following form :

$$\frac{d^2 R}{dq^2 dV_v}(q^2, v) = \frac{N_0}{A} \left[\frac{d\sigma}{dq^2}(q^2, v) \right] v \left[\frac{n_0}{k(v_{esc})} f(\mathbf{v}, \mathbf{v}_E) \right] \quad (1.22)$$

The above expression needs to be integrated over the full WIMP velocity distribution in order to generate the differential rate. The lower limit of the integral is set by a minimum velocity (v_{min}) which is determined by the lowest velocity a WIMP must have in order to produce a momentum transfer of q^2 . It turns out that $v_{min} = q/2m_r$. Substituting the form of the differential cross section from equation 1.12 into equation 1.22, the following expression is obtained :

$$\frac{dR}{dq^2}(q^2) = \frac{N_0}{A} \frac{\sigma_0}{4m_r^2} F^2(q^2) \frac{n_0}{k(v_{esc})} \int_{q/2m_r}^{v_{esc}} \frac{f(\mathbf{v}, \mathbf{v}_E)}{v} d^3v \quad (1.23)$$

The general solution to this equation leads to the following description of the differential rate :

$$\frac{dR}{dE_R}(E_R)|_{\mathbf{v}_E, v_{esc}} = \frac{k_0}{k_1} \frac{R_0}{E_0 r} \left(\frac{\sqrt{\pi}}{4} \frac{v_0}{v_E} \left[\operatorname{erf} \left(\frac{v_{min} + v_E}{v_0} \right) - \operatorname{erf} \left(\frac{v_{min} - v_E}{v_0} \right) \right] - e^{-v_{esc}^2/v_0^2} \right) \quad (1.24)$$

where

$$\begin{aligned} v_{min} &= q/2m_r = v_0 \sqrt{E_R/E_0 r} \\ \text{and } k_0 &= (\pi v_0^2)^{3/2} \\ \text{while } k_1 &= k_0 \left[\operatorname{erf} \left(\frac{v_{esc}}{v_0} \right) - \frac{2}{\sqrt{\pi}} \frac{v_{esc}}{v_0} e^{-v_{esc}^2/v_0^2} \right] \\ \text{and } r &\equiv 4m_r^2/M_W M_N = 4M_W M_N / (M_W + M_N)^2 \end{aligned}$$

The average spectrum (ignoring the annual modulation of the Earth's velocity component in the direction of the galactic disk's rotation) can be calculated by setting $v_E = \langle v_E \rangle = 232 \text{ kms}^{-1}$ in equation 1.24. For instructive purposes, it is worthwhile to examine the scenario by setting $\mathbf{v}_E = 0$ and allowing $v_{esc} \rightarrow \infty$, and using the fact that $E_R = q^2/2M_N$. This renders the differential recoil rate as :

$$\frac{dR}{dE_R}(E_R) = \frac{2}{\sqrt{\pi}} \frac{N_0}{A} n_0 \sigma_0 v_0 \frac{e^{-E_R/E_0 r}}{E_0 r} F^2(q^2 = 2M_N E_R) \quad (1.25)$$

In the above equation, we have; $E_0 \equiv M_W v_0^2/2$, and the value of $k(v_{esc} \rightarrow \infty) = k_0 = (\pi v_0^2)^{3/2}$

It is worth computing approximate rates for WIMP events to grasp the difficult nature of an experiment to detect such events. When making some gross oversimplifications to equation 1.24, the following is obtained as a description of the differential energy spectrum as a function of the recoil energy E_r :

$$\frac{dR}{dE_R} = \frac{R_0}{E_0 r} e^{-E_R/E_0 r} \quad (1.26)$$

Here R is the events rate per unit mass, R_0 is the total event rate and E_0 is the most probable incident kinetic energy. The average recoil energy is obtained by taking the mean of the differential energy spectrum over recoil energy values. It turns out that $\langle E_R \rangle = E_0 r$. Using some numerical estimates:

- Mass of WIMP (M_W) $\sim 100 \text{ GeV}/c^2$
- Mass of Nucleon (M_N) $\sim 40 \text{ GeV}/c^2$
- Velocity of WIMP (β) $\sim 0.75 \times 10^{-3} = 220 \text{ km/s}$

the mean recoil energy is computed as : $E_0 r = \frac{1}{2} M_W \beta_0^2 c^2$ which is approximately 24 keV. After substituting appropriate values in equation 1.24 an estimate of the rate is obtained as $\sim 10^{-4}$ counts / day / kg with an assumption that $\sigma_0 \sim 10^{-42} \text{ cm}^2$. See Figure 1.7 for an example of the integrated recoil rates for WIMP elastic scattering of different targets, given a cross section and halo model.

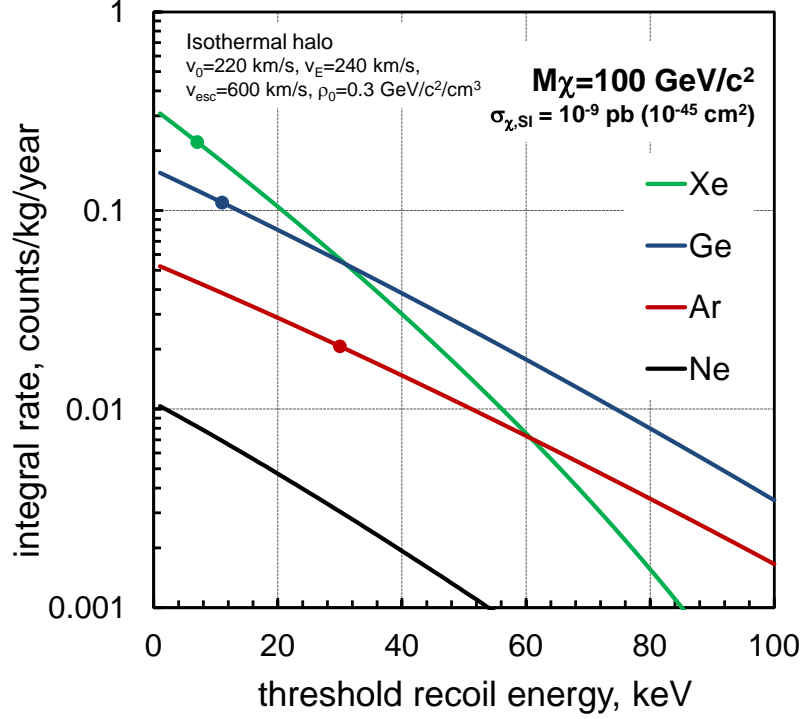


Figure 1.7: Predicted integral spectra for WIMP elastic scattering for Xe, Ge, Ar and Ne. The dark matter halo is assumed to be solely composed of WIMPs with a mass of 100 GeV/c². The cross section is assumed to be 10⁻⁴⁵cm² per nucleon. Figure taken from [25].

1.3.2 Detector Sensitivity

Understanding the WIMP interaction rate and characteristics in a detector is one part of the WIMP search. The other, perhaps more important, aspect is comprehending the interaction rate of non-WIMP events (see Chapter 3 for more details).

If a detector cannot distinguish WIMP events from background events it will observe a recoil-energy spectrum from background particle interactions. Such a detector could detect WIMP(s) if it could observe the expected recoil-energy spectrum over the background spectrum while simultaneously demonstrating that such a spectrum would be impossible to generate by another interaction. This detector could exclude a particular model for WIMPs if the the predicted spectrum has a higher event rate than the observed background rate. If no events are observed, then the sensitivity of the detector scales with it's exposure (MT),

which is simply the product of the target mass (M) and the time of operation (T). If on the other hand, events are observed, the sensitivity does not improve until a reduction in the background spectrum is achieved.

Naturally an improved detector would rely on background subtraction. If there exists a model for the background spectrum, then the possibility to subtract it and inspect for a WIMP spectrum in the residual spectrum arises. If the background model describes the observed spectrum perfectly, the residual number of counts in any bin of the histogrammed spectrum increases as the square root of the exposure $(MT)^{1/2}$. Thus, the residual event rate decreases as the reciprocal of the square root of the exposure $(MT)^{-1/2}$. While the livetime increases, so does the need for accuracy of the background model. The relative systematic uncertainty in the background subtraction method must decrease at least as quickly as $(MT)^{-1/2}$ for the statistical uncertainty to be dominant. Once a bound is reached in reducing systematic uncertainty, the sensitivity fails to improve with increased exposure.

Looking further, sensitivity can be improved by background rejection techniques. One of the most common forms of background rejections in WIMP searches, is nuclear-recoil discrimination. Being able to reject the majority of background which are electromagnetic in nature (electron-recoil events), brings the state of such a detector to the one described previously, but with a much lower background rate. Of course, no nuclear-recoil discrimination technique is perfect and hence a non-zero probability to misidentify electron recoil events as nuclear recoils exists. The sensitivity improves until systematic uncertainties become dominant.

Another class of background rejection techniques relies on the kinematics of WIMP interactions. A signature of the interaction is diurnal variation. While yet another similar technique relies on the ability to observe an annual modulation in the recoil-energy spectrum. The Earth's velocity with respect to the dark matter halo is modulated in a sinusoidal fashion because of the Earth's orbit around the Sun. Thus in the lab frame, the WIMP velocity

changes with the time of the year which results in a change in the recoil energy spectrum. Most such detectors count the number of events recorded above an energy threshold and inspect the data for a variation.

1.4 WIMP Detection Experiments

1.4.1 Indirect Detection

Indirect searches for WIMPs examine the SM products (neutrinos, gammas, positrons etc) of WIMP annihilation processes. In such scenarios the signal for WIMPs would be a mono-energetic photons or GeV neutrinos coming from the Sun or the Earth. An excess in the flux of these particles or decay products could be indicative of a WIMP signal. Large astrophysical objects like the Sun or galaxies could accumulate WIMPs at their centers. This could result in an increase in the WIMP density and consequentially an increase in the rate of self-annihilation or decay. Muon neutrinos are one such decay product that could be detected on the Earth [26]. Experiments like Super-K [27] or IceCube [28] could detect energetic muons and provide limits on WIMP annihilation rates into b-mesons, τ and W pairs. WIMP annihilation products could potentially encompass charged particles like protons, electrons and their anti-particles. Experiments such as PAMELA [29] and AMS-02 [30] have been built to look for these signals. See [31] for a brief review of indirect searches for WIMPs.

1.4.2 Direct Detection

Since a very low energy nuclear recoil (~ 10 keV) is expected from a WIMP which collides with a target particle on the Earth, a detector with a low energy threshold is required to observe such recoil energies. The readout of the energy must be efficient, while the backgrounds should be extremely low in order to claim a positive discovery for a rare event

search. A large fraction of the backgrounds are caused by interactions with the electrons of the target material and termed electron recoil (ER) events. Hence detectors must be able to distinguish background from nuclear recoil (signal-like) events. Neutron backgrounds must be kept extremely low by choosing to build the detector with extremely radio-pure components. This is because neutrons can induce nuclear recoils identical to those induced by WIMPs and hence are the most dangerous class of background. The multiple scattering of neutrons in a detector could be one handle to distinguish them from WIMP recoils, since the latter is not expected to scatter multiple times. Detector technology must also scale with the mass of the target material, since the sensitivity to WIMPs is proportional to the detector volume.

WIMP-induced recoils typically deposit energy into three channels which are exploited by different technologies. These are; 1) scintillation, 2) ionization and 3) heat/phonons. Several experiments use one or a combination of these channels to discriminate between backgrounds and signal (WIMPs). Scintillators are essentially materials that efficiently convert the energy deposited into scintillation light. The mechanism typically involves transferring the energy to electrons in the material so the nuclei are left in an excited state which de-excite with characteristic decay times and releasing optical photons. A good scintillator will typically produce photons proportional to the energy deposited, allowing for energy reconstruction, and also should be transparent to its own scintillation light. Examples of good scintillators include liquid noble gases such as argon and xenon. Nuclear recoils in a crystal lattice deposit energy in a cascade of collisions with other ions and electrons. The ions may be excited together forming a phonon excitation. The phonons then induce a tiny temperature change ($\sim 1 \mu\text{K}$), which could potentially be detected with bolometry. Experiments like DEAP[32], CLEAN [33], ZEPLIN [34] exploit the scintillation channel in order to look for WIMP signals. Experiments like DarkSide [35], Xenon [36], LUX [37] use a combination of the scintillation and ionization channels to discriminate backgrounds from signal. The use of phonons and ionization channels is made by experiments like CDMS

[38] and EDELWEISS [39], while the CRESST [40] experiment utilizes the scintillation and phonon channels for nuclear recoil discrimination. Experiments solely using the phonon channel include PICASSO [41] and COUPP [42].

1.4.3 Current Status

While the vast majority of experiments have had null results, which is to say that no events compatible with WIMPs have been observed, there is some tension in the community due to the results of the DAMA experiment. The DAMA collaboration claims a signal at more than a 5σ level (observed for more than a decade). They observe an annual modulation of the residual rate in the 2 to 6 keV_{ee} bin, with the expected period of 1 year and phase with a maximum around June 2 at the 9.3σ level [43]. If the standard halo model is assumed, two possible solutions arise for WIMPs, both of which are excluded by other experiments. Other interpretations of this observed signal exist; some of which try to explain the modulation with other backgrounds [44]. Other experiments have been set up to use sodium-iodide detectors to try and test DAMA's results with the same target.

The current best limit for high-mass WIMPs on spin-independent interaction has been set by Xenon-1T at 7.7×10^{-11} pb for a WIMP of mass 35 GeV [45]. See Figure 1.8 for visual review of some of the sensitivities of different experiments.

For low-mass WIMPs in the range (< 5 GeV/ c^2 and > 1.8 GeV/ c^2), DarkSide-50 has achieved the best limit on spin-independent cross section. See Section 4.9 for more details about this analysis and result.

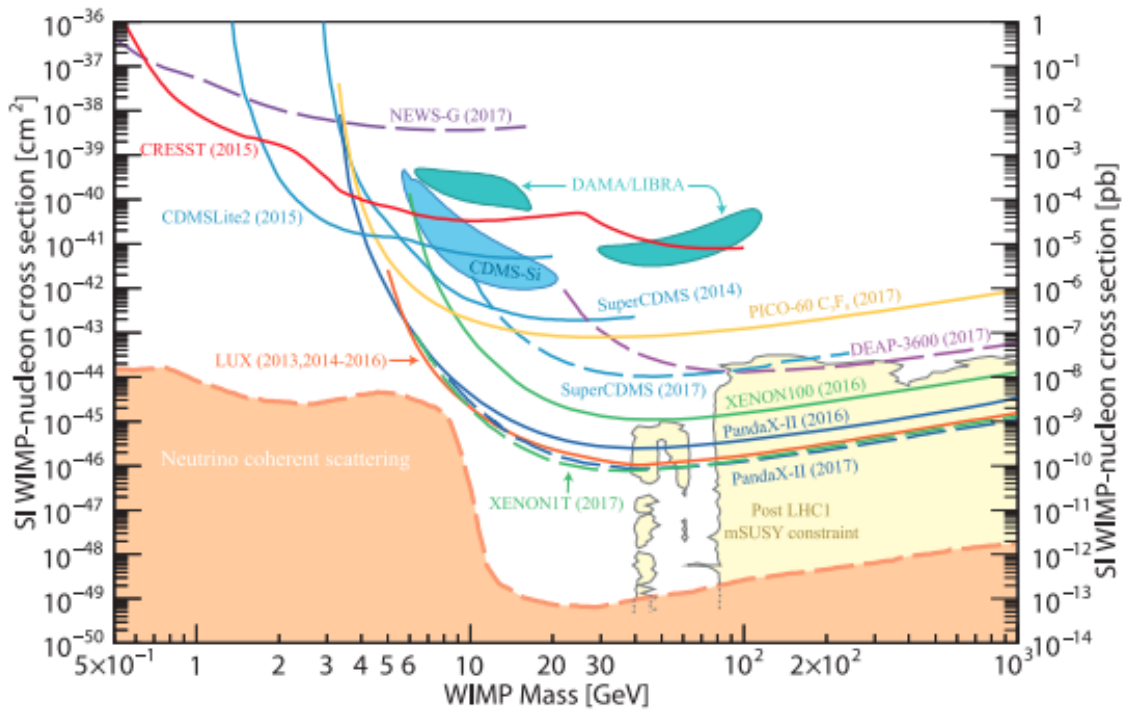


Figure 1.8: WIMP cross sections (normalized to a single nucleon) for spin-independent interactions versus WIMP mass. Figure taken from [26] which should be consulted for more details about the plot.

Chapter 2

DarkSide-50

2.1 Liquid Argon (LAr)

Argon is an extremely inert noble gas. It is colourless, odorless, nonflammable, non-corrosive and makes up approximately 1% of the Earth's atmosphere. LAr is a cryogenic liquid with a boiling point (at 1 atm) of 87 K and a freezing point (at 1 atm) of 84 K. Its density at boiling point at 1 atm is $\sim 1400 \text{ kg/m}^3$. Typically argon is produced by liquefaction of atmospheric air and separated by continuous cryogenic distillation and subsequently recovered as a cryogenic liquid.

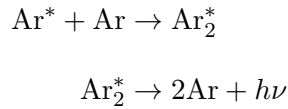
2.1.1 Scintillation Mechanism

Scintillation of LAr is well documented [46,47]. Broadly speaking, a particle interacting with LAr will either scatter off a bound electron or the argon nucleus. In both cases an electron or a nucleus will recoil through the LAr and the atom may be left in an excited or ionized state. If a charged particle moves through LAr, it experiences continuous energy loss via ionization and excitation. It may also scatter from other argon nuclei which results in a cascade like reaction where some of the energy may be transferred to the electrons

directly or via another recoiling nucleus. Residual energy is dissipated as heat. Owing to the kinematics of a collision between an electron and nucleus, the amount of energy transfer to the nucleus is minimal and in addition an electron moving through LAr will transfer practically all of its energy to other electrons.

A nucleus, on the other hand, will transfer its energy to electrons and nuclei as described by a theory developed by Lindhard et al [48]. A neutron (or a WIMP) is likely to scatter off an argon nucleus. The nucleus then loses some of its energy by recoiling off other argon nuclei. Some of these nuclei will have too little energy to cause any scintillation and simply dissipate their energy as heat, while the remaining nuclei may contribute to scintillation and ionization. The residual fraction of energy of the primary argon nucleus is distributed into ionizing and exciting argon atoms in the vicinity, thereby creating N_{ions} ions and N_{exc} excitons.

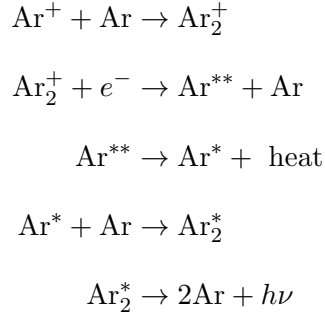
The argon exciton represented by Ar^* , has a single valence electron which is promoted to the first excited orbital. This vacancy permits the exciton to dimerize with a ground state argon atom in its vicinity. The valence electron of the ground state atom forms a bonding pair with the excited electron of the exciton in the Ar_2^* dimer/excimer. These excimers subsequently decay to the ground state and release energy in the form of a photon. Succinctly, it can be described as :



where the photon, with a characteristic wavelength of 128 nm, is represented by $h\nu$. This process is known as exciton self-trapping.

Another process which can lead to scintillation begins with an argon ion (represented by Ar^+) forming a dimer (Ar_2^+) with a ground state argon which shares one of its valence electrons. Subsequently, a free electron perhaps ionized from a nearby argon atom can be captured by the charged dimer. This process, known as recombination, splits the dimer into

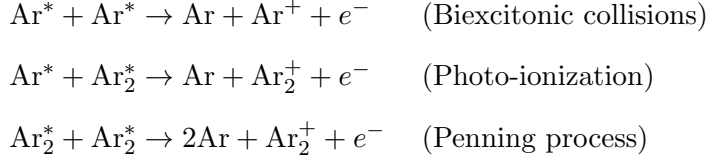
a ground state atom as well as a doubly excited atom. The latter decays in a non-radiative fashion into a single excited state which further decays through exciton self trapping. This process can be summarized as the following :



The probability for an electron to recombine, also referred to as the recombination probability, depends on the ion density in the LAr [46]. The probability to recombine also decreases in the presence of an external electric field (which is the case in our two phase TPC; see Section 2.2). The excited dimer (Ar^*) lies in a Rydberg state where an electron is in orbit around the core (Ar_2^+). Both the core and the electron have a spin of one-half, but since the spin directions can vary, four possible configuration states are permitted. One of which is a singlet while the rest are in a triplet state. The singlet state and the ground state atom each have total spin of 0 and thus the transition to the ground state is allowed by all selection rules and has a short timescale (~ 6 ns). The transition from the triplet state to the ground state is forbidden since the former has a total spin of 1 and thus the timescale associated with this process is much longer (~ 1500 ns). Regardless, either of the transitions leads to the release of scintillation light with a wavelength of 128 nm.

The formation of excimers occurs through different mechanisms for excitons and ions and these two channels form singlets and triplets with different probabilities. The exciton-to-ion ratio in LAr is ~ 0.21 for electron recoils (ER) and essentially 1 for nuclear recoils (NR). The recombination probability is proportional to the ionization density, and hence the singlet to triplet ratio can also vary with the ionization density of the particle track. The introduction of an external electric field tends to amplify this effect and brings the ratios

of singlet to triplet states for ERs and NRs closer. There are also mechanisms which can lead to the suppression of scintillation light by permitting the LAr excitons to decay in a non-radiative fashion [46]. Some of these processes are depicted below :



All of the interactions occur at rates which are proportional to the ionization density of the particle (electron or nucleus) track. They tend to have larger effects for nuclei since they have higher stopping powers. The combination of these effects, along with the proportion of production of excitons and ions for NRs and ERs, indicates that a higher fraction of scintillation generated by NRs will arise from the singlet states dimers compared to the ER scintillation. This implies that the scintillation pulse produced by NRs will typically be significantly faster than that for ERs. This leads to a methodology for implementing a background rejection technique called pulse shape discrimination.

2.1.2 Underground Argon (UAr)

Unfortunately natural argon produced from the atmosphere (AAr) contains ^{39}Ar , an isotope produced through cosmic ray interaction with ^{40}Ar via the (n,2n) reaction. ^{39}Ar undergoes β decay with a Q value of ~ 565 keV and a half life of ~ 269 years. This makes an intrinsic and overwhelming background of the LAr for a WIMP search. It is necessary to obtain argon with a reduced activity of ^{39}Ar .

Identifying an underground source with low ^{39}Ar content and subsequently extracting argon from said source is an economically feasible way to mitigate the background of ^{39}Ar .

In 2010, the DarkSide collaboration extracted over 150 kg of UAr from the Kinder Morgan facility in Cortez, CO [49] which was subsequently purified at FERMILAB [50] and deployed for a WIMP search in DarkSide-50 [51]. The reduction in ^{39}Ar activity was

measured to be more than 3 orders of magnitude from 1 Bq/kg in AAr to ~ 0.7 mBq/kg in UAr [51].

2.2 Dual Phase LAr Time Projection Chamber (LAr TPC)

A dual-phase (liquid-gas) time projection chamber (TPC) is the core of the DarkSide-50 experiment. A LAr TPC typically consists of a cylinder of LAr with a thin layer of argon gas just above the liquid volume. A uniform electric field is applied along the height of the cylindrical volume in order to drift ionized electrons, that escape recombination, into the gas layer. A stronger field is applied across the gas layer forcing the electrons to excite gaseous Ar atoms, which subsequently de-excite and scintillate. This secondary scintillation in the gaseous phase is referred to as electroluminescence. The active volume is equipped with photomultiplier tubes (PMTs) that can detect both the primary scintillation (S1) and the electroluminescence signal (S2). The faces of the PMTs are coated with a material that absorbs photons and emits electrons via the photoelectric effect. These emitted electrons are typically referred to as photoelectrons (PEs) and are multiplied forming cascades along the PMT dynode chain.

The size of S1 (in number of PE) is typically proportional to the amount of energy deposited in the sensitive volume. The size of S2 (also in PE) is directly proportional to the amount of ionization. A ratio between S2/S1 become a potential tool to discriminate between ERs and NRs. The curved surface of the TPC is typically made from a reflective material in order to optimize the light collection efficient of the signals. The top and bottom surfaces of the active volume are defined by the anode and cathode surfaces which form the drift and extraction fields. The anode/cathode windows are composed of fused silica and are coated with ITO which forms a conductive layer. A thin coat of TPB which acts as a wavelength shifter. Just below the liquid surface, an optically and drift electron transparent grid is placed to permit an independent potential setting for the drift and extraction fields.

Field shaping rings outside the TPC keep the electric field uniform and all the inner surfaces of the active volume are coated with TPB to move the Ar VUV scintillation (128 nm) to a wavelength of 420 nm where the PMTs are most sensitive. This is required as the PMTs are insensitive to the VUV range. The time it takes for an ionized electron to drift through the TPC is long compared to the time profiles of the S1 and S2 signals. Thus the time difference between the arrival of an S1 and S2 pulses provides information about the depth (along the length of the TPC, which is chosen as the \hat{z} direction by convention). The PMTs at the top have a geometry which covers the optimal surface area based on their size and number, just above the gaseous pocket. Since S2 occurs in the gas pocket, the light is concentrated on the nearby PMTs in the top array. This allows the retrieval of lateral position information (\vec{x}, \vec{y}). Thus a complete 3D reconstruction of an interaction in the TPC is possible.

DarkSide-50 is the first detector in the DarkSide program capable of producing physics results. A cross sectional view of the DarkSide-50 TPC is shown in Figure 2.1. The TPC is nested within the Liquid Scintillator Veto (LSV) which is further placed within a Water Cherenkov Detector (WCD) and is also referred to as the Water Tank (WT) or Counting Test Facility (CTF). The LSV provides passive shielding from external backgrounds, but more importantly serves as anti-coincidence for radiogenic and cosmogenic neutrons. The WCD provides passive shielding as well, but is primarily deployed as anti-coincidence for cosmogenic events. The sketch of this setup can be seen in Figure 2.2. The entire setup is located underground at Hall-C of Laboratori Nazionali del Gran Sasso at a depth of 3800 m.w.e. (metres water equivalent).

DS-50 TPC

The active volume of the TPC is a cylinder which is 36 cm tall and has a diameter of 36 cm. The cylindrical wall is made of PTFE (Teflon). The top and bottom surfaces of the active volume are marked by fused silica windows. The active volume contracts by $\sim 1.5\%$ when cooled from room temperature to 89 K (LAr temperature) due to the shrinkage of the PTFE. The active volume is instrumented with 38 PMTs in two hexagonal arrays, each

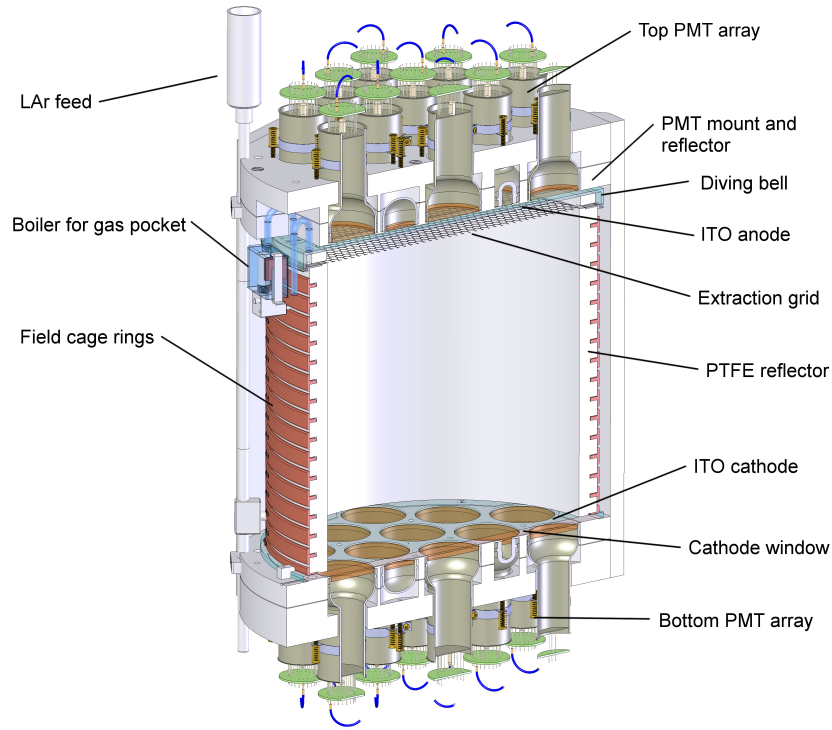


Figure 2.1: The DarkSide-50 LAr TPC. Figure taken from [35].

containing 19 PMTs, and placed at the top and bottom of the TPC. These arrays are held in position by a set of PTFE structures. The TPC is further placed inside a cryostat composed of stainless steel. See Figure 2.1 for a schematic of the DS-50 TPC.

PMTs

The DS-50 TPC PMTs are Hamamatsu (model R11065) PMTs which have a 1.5” radius photocathode and are constructed with low radioactivity materials. The PMTs have a high quantum efficiency (QE) with an average of 34% at 420 nm at room temperature. The PMT anode is held at ground while the photocathode is at negative high voltage. The PMTs are operated with a bias of approximately -1200 V which is less than the full bias (-1500 V). This avoids light emission effects at low temperatures. As a consequence, a cryogenic amplifier for each PMT is required.

Cryostat

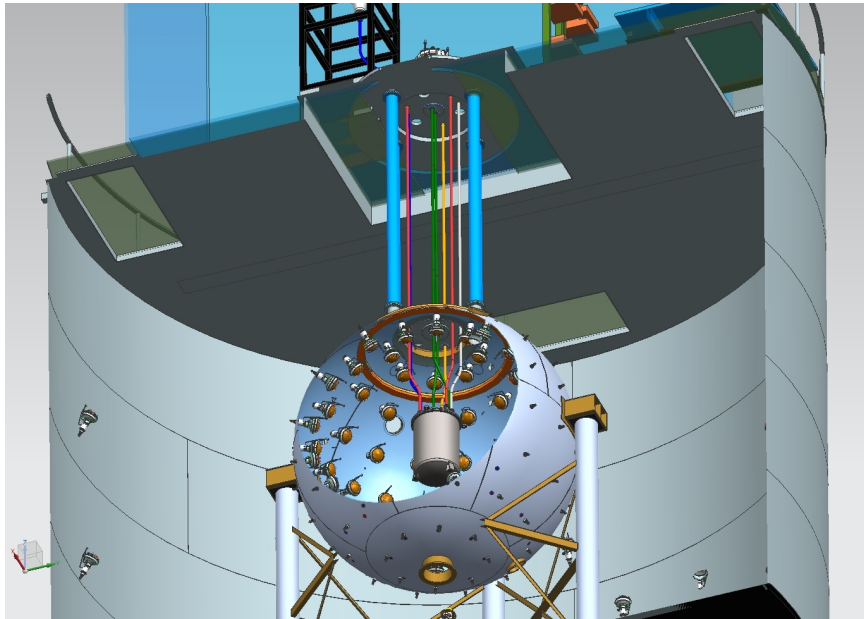


Figure 2.2: The nested detector system of DarkSide-50. The outermost gray cylinder is the WCD, the sphere is the LSV and the gray cylinder at the centre of the sphere is the LAr cryostat. Figure taken from [35].

The TPC is placed within a double-walled stainless steel cryostat with an outer radius of 32 cm and an inner radius of 25 cm. Between the cryostat walls, multiple layers of Mylar insulation and a vacuum jacket maintains the temperature at 89 K inside the cryostat. The outside of the cryostat is at room temperature. The cryostat hangs from rods that lead through the LSV to the top of the WT. The cryostat is cooled by an external circulation loop so that argon gas which leaves the cryostat passes out of the detector system directly to a purification system housed in a radon-free clean room (above the WT). The Ar gas to be purified is taken from the same places as where the cables exit the cryostat. The cables are the largest contributor to the radon out-gassing by pulling the Ar gas along them, the radon is forced up into the re-circulation system and not down into the cryostat. This gas is then passed through a getter which suppresses contaminants such as oxygen and nitrogen gas to levels below parts per billion and is subsequently liquefied by a liquid nitrogen-cooled heat exchanger, before it is transported back to the TPC active volume. Gas and liquids are transferred through a stainless steel transfer line.

2.3 PMT Calibration Procedure and Analysis

Since the fundamental quantity of interest in any interaction within the TPC is the amount of light produced as a function of time by argon recoils, it is important to understand the response of the PMTs to this light and thus the amount of charge generated inside the PMT in an event. Therefore it is critical to understand the amount of charge which is generated by a single photoelectron. This is typically done by calibrating PMTs with a low intensity, high frequency laser.

2.3.1 Conventional Methods

The standard calibration method of the single photoelectron (SPE) response of a PMT is to use a low intensity light source such that the probability of generating more than a single photoelectron within a single PMT is typically less than 0.1 per laser pulse. The resulting spectrum of the integrated signal is then fit with a model of the SPE response, to obtain the mean and variance for each PMT. The difficulty using this method lies in choosing a model. Electron multiplication within the dynode chain is a branching process where the output charge at the PMT anode depends on the secondary electron emission probability at each dynode. For the typical photoelectron, i.e. one generated at the photocathode, the most commonly used approximation is a standard Gaussian distribution [52], where the mean of the single photoelectron distribution is taken as the peak.

There are other possible sub-optimal trajectories that the electrons could take which result in under-amplified PE signals. Since these under-amplified PEs are also generated during normal operation, it is necessary to include their contribution in the estimation of the SPE mean to avoid an underestimate of the number of detected PEs.

The true shape of the under-amplified component is often difficult to determine due to the large overlap with contributions from electronic noise. Several proposals have been

made which suggest adding additional terms to the fit function of the single photoelectron response, including a falling exponential and additional Gaussian components [53, 54]. However, the development of such models usually depends on the photocathode and dynode structure and may even differ for PMTs of the same model operated at the same gain, possibly due to manufacturing differences.

2.3.2 Model-Independent Method

The calibration of the single photoelectron response for the DS-50 TPC photomultiplier tubes follows the approach of Saldanha et al [55]. The method focuses on incorporating contributions from the under-amplified photo-electrons while circumventing the need to assume the shape of the distribution.

To understand the method, it is useful to describe the process that is followed to calibrate the PMTs. Light from pulsed laser diodes is injected into the sensitive volume at a rate of 500 Hz with a 6 μ s acquisition gate, timed with respect to the trigger. These calibration runs are also referred to as laser runs. Each of these runs consists of > 400,000 events collected over a period of 5 minutes. An example of such an event in one PMT can be seen in Figure 2.3.

The runs are reconstructed with a selection of modules which are a part of the DarkArt software package which is built upon the art framework [56] developed by Fermilab. At the first step the Converter module is run. This module retrieves all useful raw information for an event and puts it in a format which can be used by all other DarkArt modules. Next the BaselineFinder is executed for each event. The goal of this module is to identify a DC offset for each PMT. (For a thorough description of DarkArt modules, see Chapter 3 of [57].) The BaselineFinder operates usually for the entirety of the waveform other than in two designated regions. The first of these regions encloses the arrival time of the PMT signal in response to the laser. This window is 104 ns long (26 samples). The other window

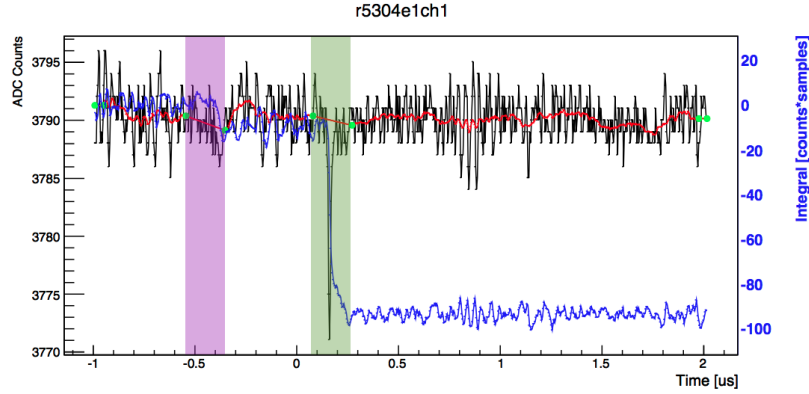


Figure 2.3: An example laser pulsed waveform (single event) in DS-50 for one PMT. The raw waveform is depicted in black, while the blue curve indicates the running integral computed by DarkSide’s waveform analysis software. The red curve indicates the baseline calculated by the BaselineFinder module. The pink region on the left is defined as the first region of interest (ROI), referred to as the background/pedestal region. The charge accumulated here is calculated as $B(q)$ which is the integral in this region. The green region on the left indicates the signal region where the large spike downwards represents the actual signal arrival due to the laser. The charge accumulated in this region is computed by the integral in this ROI and represented by $S(q)$.

used for estimating the pedestal also has the same length as the signal/laser region. The pedestal window is fixed such that it ends before the laser window begins.

There are a few assumptions made about the setup which are listed below :

- The contribution of the total charge divides into two components; namely baseline and signal, and these are assumed to be independent.
- The baseline component comprises of all the charge produced even when the signal is absent. The signal distribution contains all the contributions that are linearly proportional to the number of photoelectrons produced.
- The photomultiplier tubes and all the electronics respond linearly with respect to the number of photoelectrons.
- The number of photoelectrons follows a Poisson distribution.

Every trigger produces two contributions to the total charge (q) which is measured. One

contribution from the background and one from the signal. The total integrated charge spectrum can be written as a convolution of the background and signal spectra as follows :

$$T(q) = B(q) * S(q) \quad (2.1)$$

Here $T(q)$ is the integral charge spectrum, $B(q)$ is the background spectrum and $S(q)$ is the signal spectrum.

Using the assumptions listed above it is easy to see that the sum of the means of the background and signal distributions results in the mean of the total charge distribution. This is also exactly the same for the variance of the distribution.

$$\mathbf{E}[T] = \mathbf{E}[B] + \mathbf{E}[S] \quad (2.2)$$

$$\mathbf{V}[T] = \mathbf{V}[B] + \mathbf{V}[S] \quad (2.3)$$

The distribution of the charge associated with the signal can be expressed in terms of the number of photoelectrons, p , produced

$$S(q) = \sum_{p=0}^{\infty} S_p(q)L(p) \quad (2.4)$$

Here $S_p(q)$ is the signal charge distribution arising from the production of p photoelectrons and $L(p)$ is the probability distribution of the number of photo-electrons produced in a single trigger. It is possible to express the charge distribution of the single photoelectron response as $S_1(q) \equiv \psi(q)$. Because of the assumed linear response of the photomultiplier tubes, the multiple photoelectron response can be expressed as the p -th convolution of the single photoelectron response. More precisely, $S_p(q) \equiv \psi^p(q)$

Using the fact that $E[\psi^p] = p \cdot E[\psi]$ and $V[\psi^p] = p \cdot V[\psi]$ and some algebra which has been described in [55], the following expression for the mean and the variance of the SPE response is obtained :

$$E[\psi] = \frac{E[T] - E[B]}{E[L]} \quad (2.5)$$

and

$$V[\psi] = \frac{V[T] - V[B] - E^2[\psi]V[L]}{E[L]} \quad (2.6)$$

2.3.2.1 Estimating the Single Photo-Electron mean

As can be seen from Eqs. (2.3.2) and (2.3.2), in order to determine the first two central moments of the SPE response it is necessary to evaluate the first two central moments of the total charge distribution, the background distribution, and the mean number of photoelectrons produced in each trigger. Since prior knowledge of the true underlying distributions is absent, an estimate of the moments from the experimentally measured data sample of N triggers is formed.

The central moments of the total charge distribution can be directly obtained by calculating the mean and variance of the measured PMT output spectrum in the presence of the laser. This is typically the spectrum that is used to fit the SPE response.

Typically there is an overlap of the background distribution and the signal distribution of under-amplified single photoelectrons. This makes it difficult to determine the mean and variance of the background in the presence of the laser signal. To mitigate this issue, an estimate of the moments of the background spectrum is made separately from the measured blank data set.

The only parameter that is not trivial to estimate, is the mean number of laser-induced photoelectrons produced in each trigger, $\mathbf{E}[L]$, which is referred to as the occupancy. As mentioned previously, the number of photoelectrons produced follows a Poisson distribution, which can be written as

$$L(p) = \frac{\lambda^p e^{-\lambda}}{p!} \quad (2.7)$$

$$\lambda \equiv \mathbf{E}[L] = \mathbf{V}[L] \quad (2.8)$$

The occupancy λ is directly related to the probability of producing zero laser-induced photoelectrons,

$$\lambda = -\ln L(p) \quad (2.9)$$

and can be estimated from the number of sample triggers with zero laser-induced photoelectrons (zero-pe triggers), N_0 , and the total number of sample triggers N

$$\hat{\lambda} \equiv -\ln(\widehat{N}_0/N) \quad (2.10)$$

Here $\hat{\lambda}$ and \widehat{N}_0 denote the estimates of the occupancy and number of zero-pe triggers in the laser data sample, respectively.

There are several different techniques which can be used to estimate the value N_0 and the optimal method depends on the nature of the signal and background distributions. For example, if the temporal shape of the PMT output pulse is known, and the triggers are individually recorded, it is possible to assign a likelihood for the presence of a laser-induced signal to each individual trigger. In this case, a very simple algorithm is used, from which the associated statistical and systematic uncertainties can be estimated analytically.

If access to a pure sample of zero-pe events from the blank data set is available, empirical information about the shape of the zero-pe distribution can be obtained. An estimate of the number of zero-pe triggers is obtained as follows :

1. A threshold cut is placed at a low charge value ensuring that the fraction of laser triggers with a non-zero number of laser-induced photoelectrons, that fall below the cut, is small. The number of triggers, A_T , in the laser data set below the threshold is then assumed to be the number of zero-PE triggers.
2. To assess the total number of zero-pe triggers in the laser sample, N_0 , information from the blank spectrum is used to correct the value of A_T for the number of zero-pe triggers which fall above the threshold. The fraction of blank data samples that fall below the threshold cut is defined as f . The estimated total number of zero-PE triggers in the laser data set is then :

$$\widehat{N}_0 = \frac{A_T}{f} \quad (2.11)$$

The estimate for $\widehat{\lambda}$ is therefore

$$\widehat{\lambda} = -\ln(A_T/fN) \quad (2.12)$$

Rather than expressing the position of the threshold cut in terms of a charge value, which depends on the shape of the background distribution, the cut can be expressed in terms of the fraction, f , of the background distribution that falls below the threshold. This allows a description of the choice of threshold in a way that can be easily translated to different experimental setups. Moreover, the statistical and systematic uncertainties are conveniently expressed in terms of the fraction, f .

2.3.2.2 Reducing Uncertainty for the SPE claibration

After a careful inspection of the trends of the SPE mean as a function of the threshold fraction, it was realized that the high occupancy channels (PMT numbers 5 and 6) showed signs of a possible bias. It was difficult to evaluate the presence of a bias in the low occupancy channels since the statistical uncertainty was quite high.

The statistical uncertainty on the estimated occupancy can be expressed as (See Appendix A of [55] for a derivation):

$$V[\widehat{\lambda}] = \frac{(e^\lambda + 1 - 2f)}{fN} \quad (2.13)$$

which leads to the following relation for the statistical uncertainty on the estimate of the SPE mean :

$$\mathbf{V}[\widehat{\mathbf{E}}[\psi]] \approx \frac{\mathbf{V}[T] + \mathbf{V}[B]}{N\lambda^2} + \frac{(\mathbf{E}[T] - E[B])^2 (e^\lambda + 1 - 2f)}{fN\lambda^4} \quad (2.14)$$

This bias in the SPE mean arises from a systematic bias in the estimation of the occupancy where the estimated occupancy was generally lower and decreases for high and increasing threshold fractions. This bias has been quantified as [55] :

$$E[\widehat{E}[\psi]] \approx E[\psi] \cdot \left(1 + \frac{k(f)}{f}\right) \quad (2.15)$$

where $k(f)$ is the fraction of triggers with exactly one laser-induced photoelectron, which falls below the threshold fraction cut. It is assumed that $\frac{k(f)}{f} \ll 1$

After this realization, various techniques were implemented in order to reduce or quantify the bias. Firstly, an optical filter was removed such that the occupancy of all channels increased by a factor of ~ 3 . This allowed for a reduction in the statistical uncertainty and

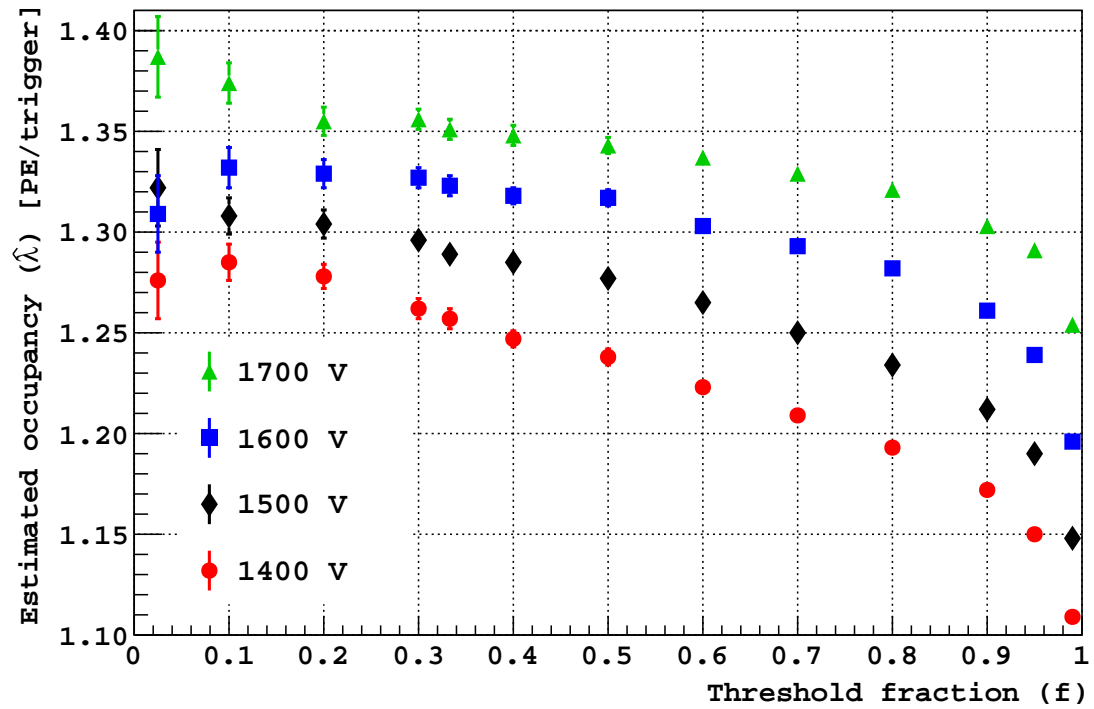


Figure 2.4: Occupancy as a function of threshold fraction for different PMT voltage differences. A trend is seen for an increase in occupancy with the increase in gain. Also a decrease in occupancy with an increase in f . It seems the systematic bias increases as the gain is lowered, hence the occupancy could be fixed to the value obtained at the highest gain, where the bias is the least. Figure taken from [55].

gave a handle to evaluate the trend of the SPE mean as a function of threshold fraction. While [55] suggests operating at relatively lower threshold fractions, since the fraction of underamplified photoelectrons falling below the threshold reduces, and the systematic bias in the occupancy is lower (see Figure 2.4); calibrating the SPE mean with low values of f in DS-50 resulted in the SPE mean varying with time. An independent algorithm (based on a voting structure) was developed with the goal of finding the optimal value of f , optimizing for reduction in bias and stability in the discrete derivative ($\frac{\partial \lambda}{\partial f}$) using a sliding window over f . However the algorithm was not deployed in the DS-50 analyses. Instead a higher value of f (0.975) was chosen where the uncertainty arising from the occupancy was comparable to uncertainty on the SPE mean (see Figure 2.5).

A critical difference between the procedure followed by DS-50 and the one suggested by Saldanha et al [55] is that in DS-50 in-situ calibration is performed by the laser runs and hence the possibility of physically blocking the laser light from reaching the PMTs is not present. There is no choice but to dedicate two different time windows within each event and assign them as signal and background regions. This leads to the background in the pedestal region being independent of the background in the signal region due to inherent differences in the electronics.

In fact, in DS-50 a shift between the charge spectra for background and signal is observed, for the few runs that were performed with the laser light physically blocked. The algorithm developed for computing the mean of SPE takes into account this shift, and corrects for it during offline analysis. Effort was made to reduce the shift correction that was needed, such that the uncertainty arising from the correction procedure could be reduced.

At first, the moving average of several ($> 10k$) events was taken for runs where the laser light had been physically blocked. The moving average window was varied in order to permit visual observations of any periodicity present in the waveforms. With some inference after visual inspection as seen from Figure 2.6, a fast-Fourier transform was applied to the

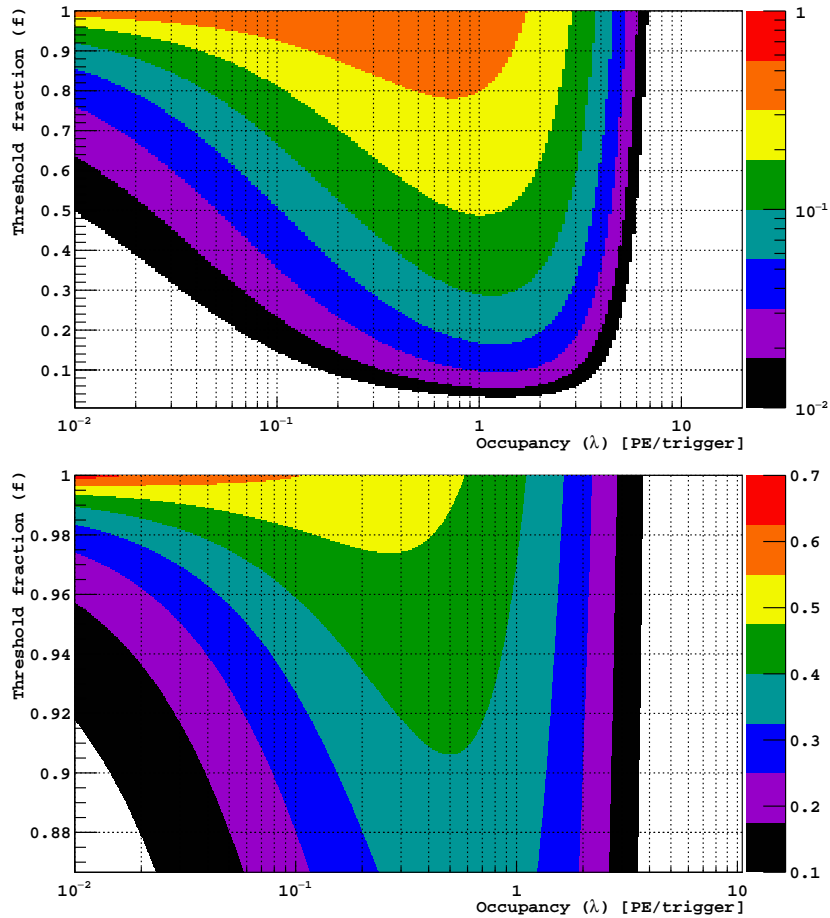


Figure 2.5: (top) The ratio of the uncertainty on the occupancy to the total uncertainty on the SPE mean is shown on the colour scale, as a function of the occupancy (on the x axis) and the threshold fraction (on the y axis). (bottom) A zoomed version. The plot shows that it is preferable to operate at higher occupancies and higher values of the threshold fraction to reduce uncertainty, purely from a statistical perspective.

average of 10k events. The results are shown in Figure 2.7. From these figures, it is clear that a particular frequency, corresponding to the frequency of the digitizer, is dominant. This could lead to the periodicity effect we observe. It is also apparent that these frequencies are not locked in a particular phase. It was suggested that to cancel the periodicity effect, it might be possible to set the range and width of the two time windows to be such that the shift correction is minimized. This procedure was attempted, but it was not clear that it would mitigate the need for a shift correction, since the noise from the electronics appeared itself to be time-dependent.

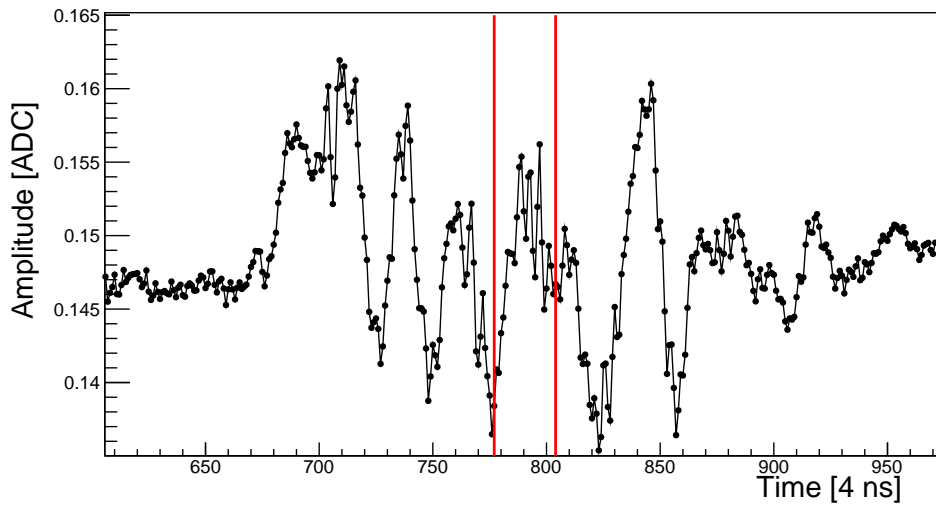
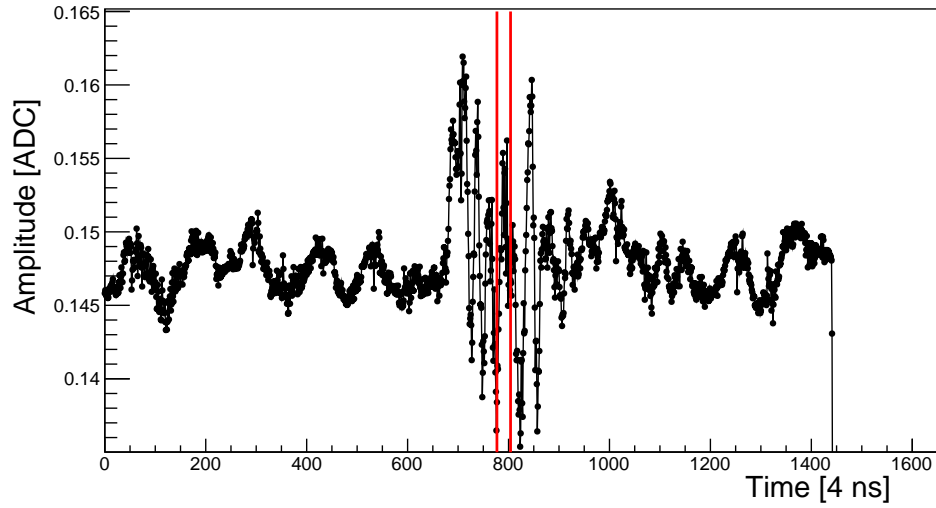


Figure 2.6: Fourier transform of 10,000 averaged waveforms where the laser was physically blocked. (top) Shown here are the frequency and phase on the x and y axes respectively, while the colour scale represents the ADC value. (bottom) is a projection onto the y-axis.

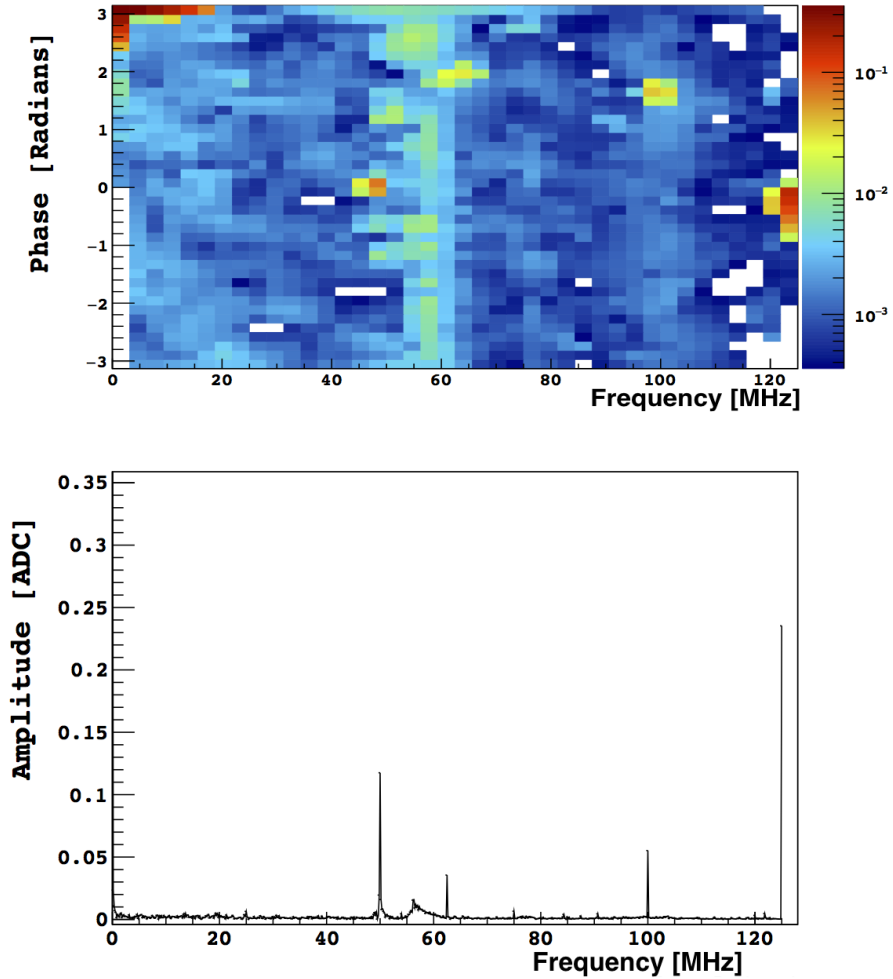


Figure 2.7: Fourier transform of 10,000 averaged waveforms where the laser was physically blocked. (top) Shown here are the frequency and phase on the x and y axes respectively, while the colour scale represents the ADC value. (bottom) is a projection onto the y-axis.

2.4 Veto Detectors

This section describes the two outer detectors, namely the LSV and the WCD and follows the discussion of [58]. The most critical background for a WIMP search are nuclear recoils from single neutron scatters since they mimic WIMP interactions in the TPC. One solution is to use passive shielding around the detector. But this shielding alone does

not allow the measurement of background levels, which makes the interpretation of recoil events (compatible with WIMP signatures) difficult. Moreover, a passive shield cannot be employed to protect against radiation arising from detector components themselves. Neither can it shield against high energy neutrons arising from cosmic ray interactions with the surrounding material. On the other hand, DarkSide-50 employs a unique method of active shielding (veto). The TPC is surrounded by a large volume of material with high neutron cross section. This allows identification of interactions resulting from a neutron in the TPC through coincident detection of the neutron in the veto. A WIMP, since it is very weakly interacting, is only likely to scatter in the TPC and will not leave accompanying signals in the surrounding active shielding material (anti-coincidence). The veto also permits in-situ measurements of the neutron background to the setup. DS-50 utilizes the combination of the two outer detectors; the LSV and the WT, to actively veto radiogenic and cosmogenic neutrons.

2.4.1 Liquid Scintillator Veto (LSV)

The LSV is a 4.0 m diameter stainless steel sphere filled with 30 tonnes of boron-loaded liquid scintillator. The sphere is lined with Lumirror, a reflecting foil used to enhance the light collection efficiency. An array of 110 Hamamatsu R5912 LRI 8" PMTs is mounted on the inside surface of the sphere to detect photons arising from scintillation. Photographs of the inside of the LSV detector can be seen in Figure 2.8.

The neutron capture reaction $^{10}\text{B}(n, \alpha)^7\text{Li}$ makes the boron-loaded scintillator a very effective neutron veto because of its large cross section for thermal neutron capture leading to charged products. An α particle and a ^7Li nucleus are always produced as a result of the neutron capture on ^{10}B . Because the α and the ^7Li nucleus move only short distances, a neutron capture on ^{10}B in the LSV scintillator will always deposit visible energy in the detector.

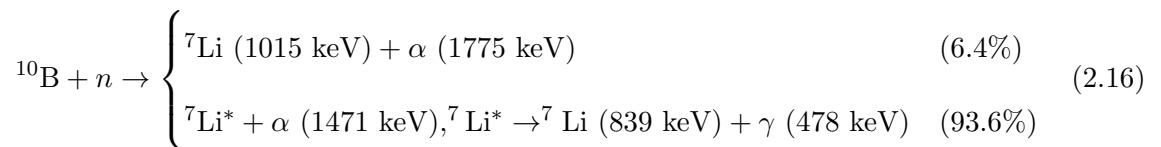


Figure 2.8: (Left) The Liquid Scintillator Veto (LSV). The picture shows the cryostat of the DarkSide-50 LAr TPC hanging from the top. (Right) The picture shows the internal surface of the LSV, covered with Lumirror, with PMTs evenly distributed inside. Figure taken from [58].

2.4.2 Organic Liquid Scintillator

The boron-loaded liquid scintillator has three primary components: pseudocumene (PC), trimethyl borate (TMB), and 2,5-diphenyloxazole (PPO). PC, $C_6H_3(CH_3)_3$, is the primary scintillator used in the veto and is the bulk of the cocktail. TMB, $B(OCH_3)_3$, is an organic molecule containing one boron atom. ^{10}B , with a natural abundance of 19.9%, and has a very high thermal neutron capture cross section of 3837 barn [60].

When a neutron captures on ^{10}B , two reactions are possible:



The decay to the excited state produces a γ -ray that is easily seen as long as it does not escape into the cryostat before depositing energy in the scintillator. Energy deposits

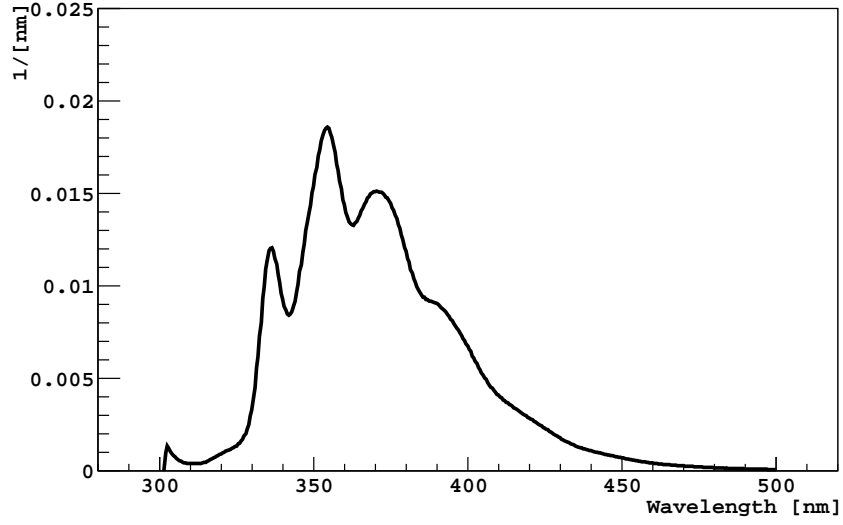


Figure 2.9: The emission spectrum of PPO [59]. Figure taken from [58].

due to the α and ${}^7\text{Li}$ nucleus are always contained in the scintillator, due to their high stopping power and thus short track lengths. The light output of α and ${}^7\text{Li}$ nuclei is highly suppressed because of ionization quenching. This causes them to scintillate equivalently to a 50–60 keV electron (an energy scale referred to as “keV electron equivalent”, or keV_{ee}). Detecting these decay products therefore requires a high light collection efficiency and a low background level. If the detector can reliably detect these nuclear decay products, it can efficiently detect neutrons that capture in the veto, regardless of their initial kinetic energy, since the energy of these capture products does not depend on the neutron’s initial energy.

In addition to capturing on ${}^{10}\text{B}$, a thermal neutron may also capture on ${}^1\text{H}$ or ${}^{12}\text{C}$ through the following reactions

$$\begin{aligned}
 & {}^1\text{H} + n \rightarrow {}^2\text{H} + \gamma \text{ (2223 keV)} \quad I_\gamma/I_\gamma(\text{max}) = 100\% \quad \sigma = 0.33\text{b} \\
 & {}^{12}\text{C} + n \rightarrow \begin{cases} {}^{13}\text{C} + \gamma \text{ (3090 keV)} & I_\gamma/I_\gamma(\text{max}) = 100\% \\ {}^{13}\text{C} + \gamma \text{ (4945 keV)} & I_\gamma/I_\gamma(\text{max}) = 67\% \quad \sigma = 0.0034\text{b} \\ {}^{13}\text{C} + \gamma \text{ (1860 keV)} & I_\gamma/I_\gamma(\text{max}) = 57\% \end{cases} \quad (2.17)
 \end{aligned}$$

where σ is the thermal neutron capture cross section, $I_\gamma/I_\gamma(\text{max})$ is the intensity of the

γ -ray, relative to the maximum intensity γ -ray [61]. For ^{12}C only the three dominant γ -rays are shown.

The wavelength shifter PPO is added to the scintillator cocktail in a concentration of a few grams per liter to increase the detection efficiency of the LSV. PPO scintillates much faster than PC, hence adding PPO can make the light signal faster, allowing for tighter prompt coincidence cuts. Borexino has observed that increasing the PPO concentration decreases the effects of ionization quenching, which made it easier to detect the nuclear decay products [62, 63]. The emission spectrum of the PPO is shown in Figure 2.9.

The LSV was first filled with boron-loaded scintillator during the first two weeks of October, 2013. Two different mixtures of PC, TMB, and PPO were used in the two WIMP search phases of DarkSide-50:

- *Phase-I* Nov. 2013 – June 2014: 50% mass fraction of PC, 50% TMB, 2.5 g/L PPO
- *Phase-II* Feb. 2015 – present: 95% mass fraction of PC, 5% TMB, 1.4 g/L PPO

The capture times and relative rate of neutrons capturing on ^1H , ^{10}B , and ^{12}C can be calculated from the cross sections and the chemical compositions and concentrations of PC and TMB. During Phase-I of DarkSide-50, with a 50% TMB concentration, the neutron capture time was $\sim 2.2\ \mu\text{s}$ and $\sim 0.8\%$ of neutron captures were expected to be on ^1H . During Phase-II, with a $\sim 5\%$ concentration, the neutron capture time is $\sim 22\ \mu\text{s}$ and it was expected that $\sim 8\%$ of neutrons capture on ^1H . The number of captures on ^{12}C should be about two orders of magnitude below the ^1H capture rate.

2.4.3 Lumirror reflector

The LSV has $\sim 7\%$ photo-detector coverage because of cost restrictions. To compensate for this seemingly low coverage, the inner walls of the LSV have been lined with a reflector. After some experimentation [64–66], Lumirror 188 E6SR was chosen. Lumirror is a highly

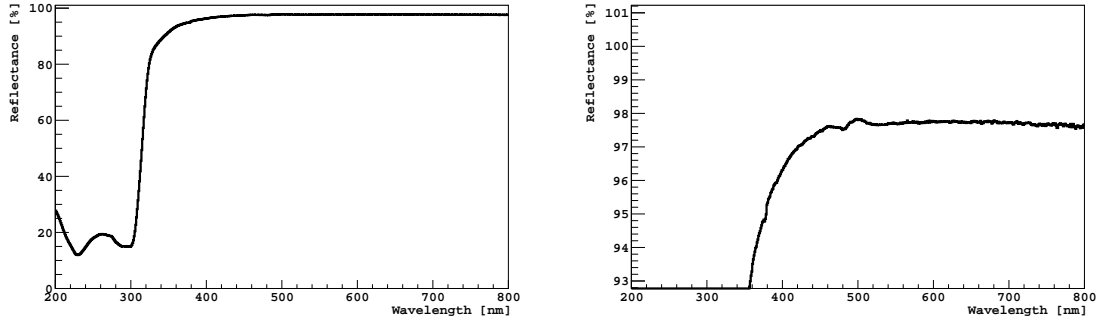


Figure 2.10: The reflectance measured for Lumirror E6SR. There is a sharp cutoff at wavelengths shorter than ~ 350 nm. The bump in reflectance around 260 nm is due to the specular component of the reflectivity. (Left) The reflectance over the full range measured. (Right) The reflectance near the maximum value. Figure taken from [58].

reflective void-based reflector between two protective layers that allow the reflector to be submerged in scintillator without significant loss of reflectivity [64].

A sample of measurements of the Lumirror reflectance taken with a Perkin Elmer Lambda-650 spectrophotometer are shown in figure 2.10. As can be seen in this figure, the Lumirror has a maximum reflectance of $\sim 97.5\%$ for wavelengths greater than ~ 350 nm, and has a steep cutoff at shorter wavelengths, below most of the scintillator’s emission spectrum. A photograph of the LSV with the LAr TPC inserted inside it is shown in Figure 2.8. The exterior surface of the TPC cryostat is not covered with Lumirror.

2.4.4 LSV PMTs

The LSV is equipped with 110 Hamamatsu R5912 LRI 8” PMTs with low-radioactivity glass bulbs and high-quantum-efficiency photocathodes (37% average quantum efficiency at 408 nm) [67]. All 110 PMTs are mounted on the stainless steel sphere, as shown in figure 2.8. The PMTs were chosen for their low radioactivity glass, low dark-pulse rate, low after-pulse rate, and a 1σ transit time spread of ~ 1 ns, much smaller than the scintillation light pulse width. The amplitude and timing response performance of single electrons is particularly important due to the need to measure prompt coincidences with the LAr TPC with a very

low threshold. Furthermore, in order to minimize the background from PMT noise, the PMTs have to feature a low dark rate and have a low probability of PMT after-pulsing. [58, 68] All of the PMTs were tested in the photomultiplier tube testing facility of the Borexino experiment at LNGS [69].

In order to determine the energy of scintillation events, it is important to know the total charge collected by each PMT. For this reason, charge calibration of the PMTs is required. The light emitted by an external picosecond 405 nm laser source is carried simultaneously to each PMT by a dedicated system of optical fibers via 10 custom-designed optical feed-throughs, which are further split into 110 individual fibers each coupled to a PMT. The design has been based on the experience gained in the development of the Borexino experiment [70].

2.4.5 Calibration system

A CALibration Insertion System (CALIS) [71] is used to deploy radioactive sources to calibrate both the TPC and the LSV. CALIS was constructed, tested at Fermilab and LNGS, precision cleaned, and installed in DarkSide-50 during summer, 2014 (Figure 2.11). Since then it has been used for extended calibration campaigns of both the TPC and LSV involving radioactive γ -ray (^{57}Co , ^{137}Cs , ^{133}Ba) and neutron ($^{241}\text{AmBe}$) sources (see Figure 2.12).

2.4.6 Water Cherenkov Veto

The Water Cherenkov Veto (WCV) is a powerful shield against external background (γ -rays and neutrons from the rock), and is also used as a Cherenkov muon detector. The muon flux at the 3800 m.w.e. depth of the LNGS, although reduced from that at the Earth's surface by a factor $\sim 10^6$, is of the order of 1.1 muons/(m²·hr) [72]. This corresponds to about 2000 muons per day crossing the WCV, about 380 muons per day crossing the LSV,

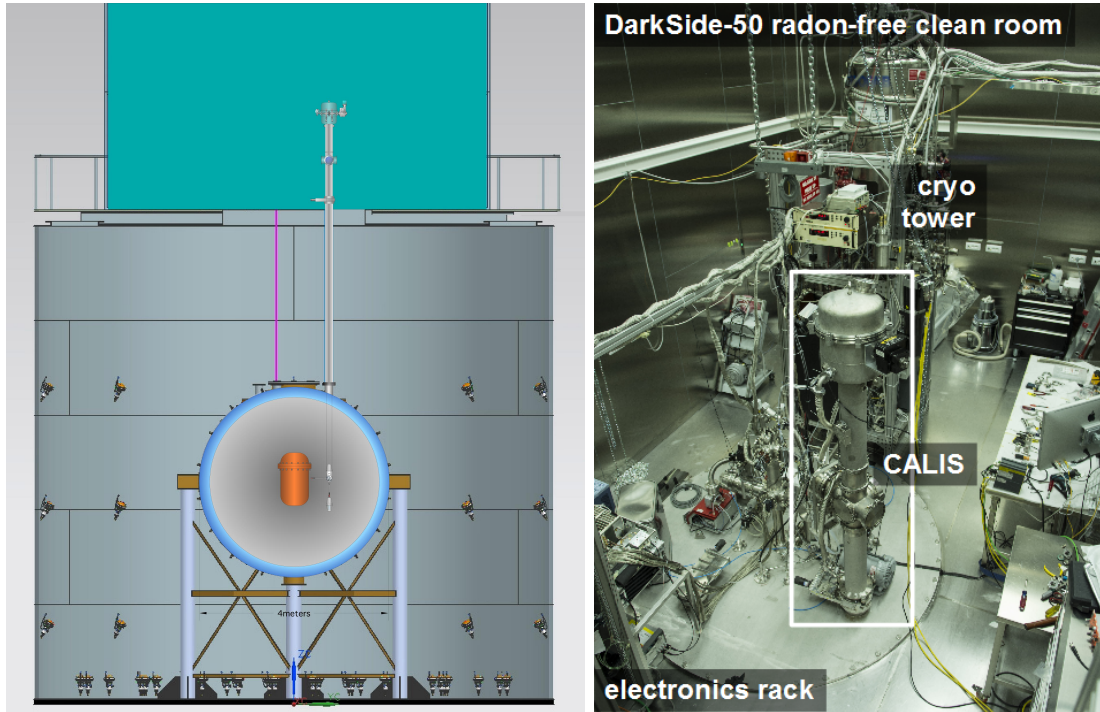


Figure 2.11: *Left*: Sketch of CALIS installed inside the radon-free clean room CRH atop the WCV and with the deployment device next to the cryostat. The source arm is articulated. *Right*: Photograph of CRH after installation of CALIS.

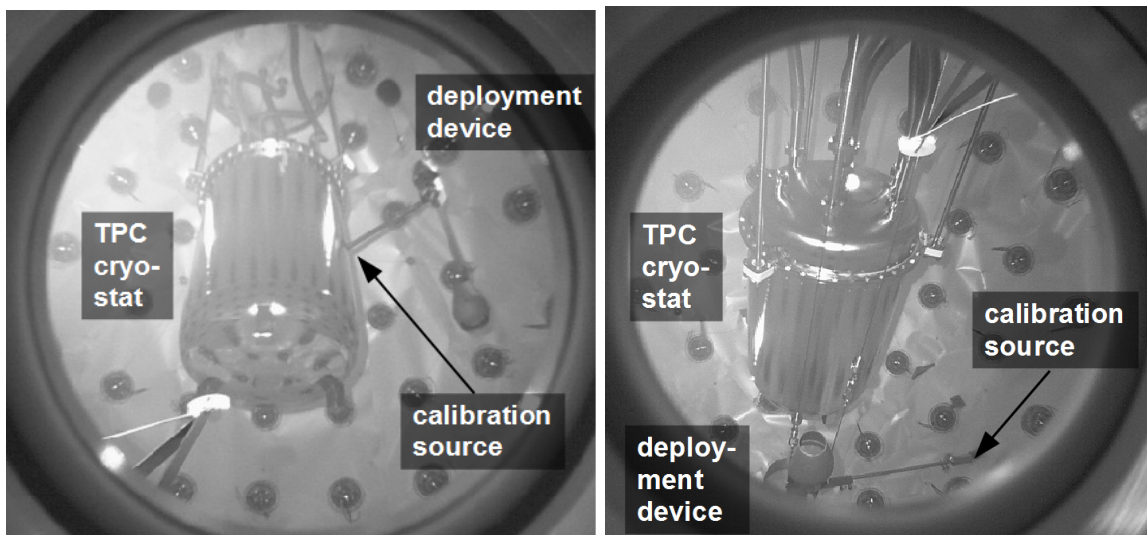


Figure 2.12: Photographs taken with cameras looking into the LSV. *Left*: CALIS with the source in contact with the cryostat of the LAr TPC. *Right*: CALIS with the $^{241}\text{AmBe}$ source rotated away from the LAr TPC in order to study position dependent effects. Figure taken from [58].

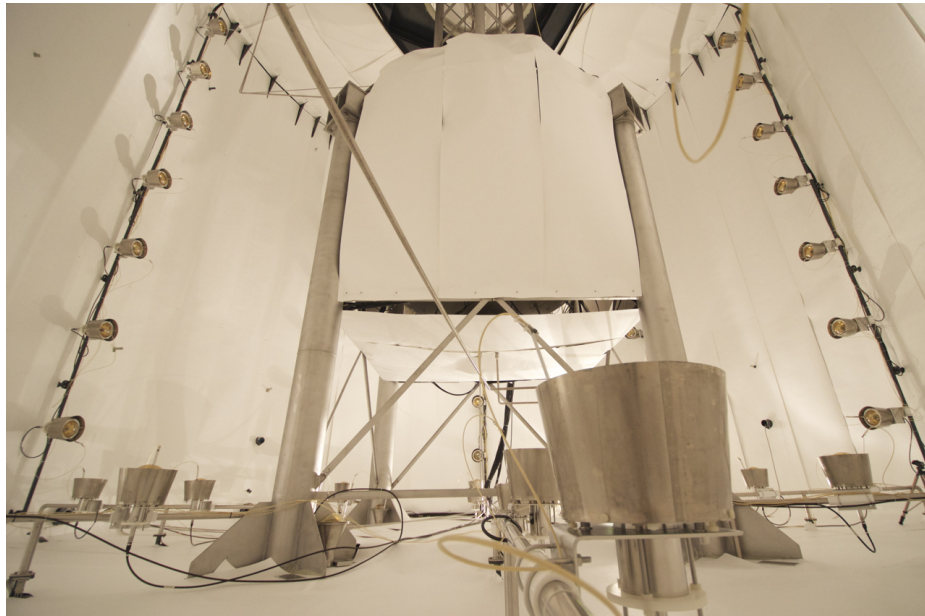


Figure 2.13: The inner surface of the Water Cherenkov Veto covered with layers of Tyvek. The Liquid Scintillator Veto, installed on four stilts and also covered in Tyvek, can be seen in the middle of the water tank. Figure taken from [58].

and about 4 muons per day crossing the LAr TPC. Cosmogenic muons can produce high energy neutrons [73], which can penetrate several meters of shielding. In order to avoid backgrounds from these high energy neutrons, the WCV acts as a veto to detect the muons that may produce them and therefore leave a detectable coincident signal. The WCV is equipped with 80 8" PMTs: 56 in 8 columns on the cylindrical tank wall and 24 on the floor. These PMTs collect the Cherenkov light emitted by muons or muons' electromagnetic shower products in the water. The WCV uses the water tank from the Borexino Counting Test Facility (CTF) [74], and the design draws on the muon detector of the Borexino experiment.

Figure 2.13 shows a photograph of the inside of the WCV. The tank is a cylinder with a diameter of 11 m and a height of 10 m for a total volume of $\sim 1000 \text{ m}^3$. It is built from carbon steel and internally protected from corrosion by a layer of Permatex resin. In order to improve the light collection efficiency, the interior surface of the WCV and the exterior of the LSV sphere are covered with a layer of highly reflective Tyvek [75].

Since the background signals in the WCV are very small compared to the large Cherenkov

signal produced by the muons, light collection efficiency is not as crucial as it is in the LSV, allowing the reuse the PMTs from CTF and use of cheaper reflector without sacrificing detector performance.

2.4.7 Tyvek reflector

The inner surfaces of the WCV, including the outer surfaces of the LSV, are covered with a layer of a Tyvek-based reflector provided by the Daya Bay collaboration [76]. This reflector consists of two layers of DuPont Tyvek 1082D bonded together by a layer of polyethylene. The reflectivity of this material has been measured to be greater than 96% in air and 99% in water, for wavelengths between 300 and 800 nm [76].

2.4.8 WCV photomultiplier tubes

The WCV is lined with 80 20 cm diameter ETL 9351 8" PMTs. These are the same PMTs used by the CTF experiment [77], after 15 years of continuous operation. These PMTs have a peak quantum efficiency of $\sim 25\%$ at 380 nm and a dark rate of ~ 2500 Hz.

Similar to the LSV PMTs, the WCV PMTs are each equipped with an optical fiber pointing at the photocathodes, and are connected to the same laser system as the LSV PMTs, in order to perform the SPE calibration. Each PMT is surrounded by a conical light collector which increases the effective coverage of the PMTs.

Cherenkov Effect

A charged particle moving through a medium creates a time varying electromagnetic perturbation. If the velocity (v) at which the particle is traveling at, is more than the critical velocity of the medium (defined by $v_{crit}=c/\eta$; where η is the index of refraction), a delayed polarization of the medium is observed and the resulting dipoles radiate coherently.

Cherenkov radiation is emitted in a cone, whose angle is defined by :

$$\theta = \arccos \left(\frac{1}{\eta\beta} \right) = \cos^{-1} \left(\frac{1}{\eta\beta} \right) \quad (2.18)$$

where β is the ratio of the velocity of the particle to the velocity of light in vacuum (v/c).

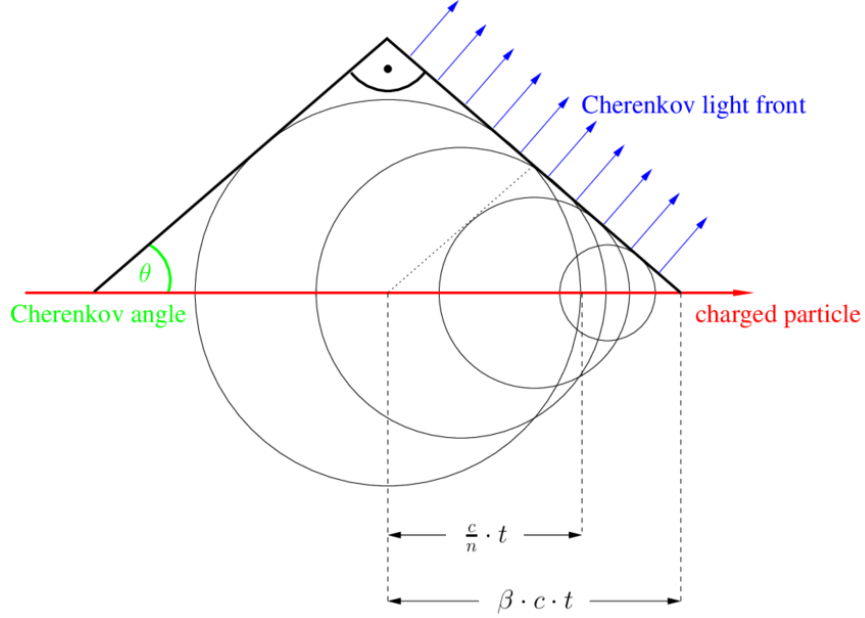


Figure 2.14: Illustration of the Cherenkov effect created by a charged particle traveling with velocity c/n in a medium of refractive index n . The Cherenkov angle is defined by equation 2.4.8. Figure taken from [78].

The Cherenkov effect is well described by the Frank-Tamm formula which computes the number of Cherenkov photons produced per unit path length and per unit energy of a charged particle.

$$\frac{d^2N}{dE dx} = \frac{\alpha Z^2}{\hbar c} \sin^2 \theta_c = \frac{\alpha^2 Z^2}{r_e m_e c^2} \left(1 - \frac{1}{\beta^2 \eta^2(E)} \right) \quad (2.19)$$

where Z is the charge of the particle; r_e is the radius of the electron; m_e is the mass of the electron; α is the fine structure constant.

When substituting the values of the fundamental constants, the following is obtained :

$$\frac{d^2N}{dEdx} \approx 370Z^2 \sin^2 \theta_c(E) \text{ eV}^{-1} \text{ cm}^{-1} \quad (2.20)$$

By integrating this equation over a range of wavelengths and using the fact that the refractive index of water is ~ 1.33 , a photon count of more than 200 per cm is obtained. This is very relevant for the detection of cosmic muons (or other charged particles of cosmic origin) passing through the WCD, since they will generate several thousand photons which should be sufficient to veto cosmogenic events. (See Section 3.5 for more details.)

2.5 G4DS - The DarkSide Monte Carlo Tool

The DarkSide collaboration has developed a Geant4-based Monte Carlo package (G4DS) to simulate the response of DarkSide-50. The details about the development and implementation of this simulation can be found in [79, 80]. G4DS reproduces energy and time observables at the percent level. G4DS has been crucially utilized in several DS-50 analyses [35, 51, 81], including the ones presented in the latter chapters of this document. Its modular nature allows an extension to incorporate other geometric structures such as the DS-20k detector [82]. In particular, it is worth summarizing the scintillation model customized for DS-50 which described the physical processes that produce the S1 and S2 signals.

PARIS model

The TPC optical response is tuned and an effective model is adopted in G4DS to parameterize the processes which induce S1 and S2. This model is called PARIS (Precision Argon Response Ionization and Scintillation). To model the process of scintillation (see Section 2.1.1) in the PARIS model, the following approach is taken (under the assumption that there is no quenching for electron recoils) :

$$E_{\text{dep}} = N_i W_i + N_{\text{ex}} W_{\text{ex}} \quad (2.21)$$

where the energy deposited (E_{dep}) by an electron recoil is split into excitation and ionization. W_i and W_{ex} represent the work functions to produce an electron-ion pair and an exciton respectively. With the introduction of an effective work function defined as :

$$W = \frac{\alpha W_{\text{ex}} + W_i}{1 + \alpha} \quad (2.22)$$

It is possible to re-define the number of ions and excitons as :

$$N_i = \frac{E_{\text{dep}}}{W} \frac{1}{1 + \alpha} \quad (2.23)$$

$$N_{\text{ex}} = \frac{E_{\text{dep}}}{W} \frac{\alpha}{1 + \alpha} \quad (2.24)$$

where α is simply the ratio of the number of excitons to ions, and it is different for ERs and NRs. The value of W is estimated to be 19.5 eV [83]. As a reminder, for ERs α is estimated to be 0.21 and 1 for NRs (see Section 2.1.1).

If it is assumed that the an S1 photon can originate directly from an excitation component or from the recombination of an electron-ion pair, then S1 can be parameterized as

$$S1 = g_1 (N_{\text{ex}} + r(E) \times N_i) \quad (2.25)$$

where $r(E)$ is the kinetic energy (E) dependent recombination probability. g_1 is the collection efficiency of photons generated in LAr. This factor includes the PMT quantum efficiency, optical coverage and light absorption in the materials of the detector. The factor g_1 was estimated to be 0.157 ± 0.001 . This was done by simulating UV photons uniformly distributed in the TPC. Similarly, S2 (proportional to the number of electrons that survive

recombination) is parameterized as :

$$S2 = g_2 \varepsilon_{s2} \times (1 - r(E)) \times N_i \quad (2.26)$$

where ε_{s2} is the electroluminescence yield, g_2 is the detection efficiency of photons generated in the gas pocket and is estimated to be 0.163 ± 0.001 . G4DS assumes that all electrons recombine when there is no external electric field applied.

A Geant4 based simulation code, NEST [84], combined the Thomas-Imel [85] and Doke-Birks [86] models by constraining the parameters using experimental datasets. These data are unfortunately scarce for LAr and hence a NEST-based approach was not chosen for G4DS. Instead an empirical parameterization of the recombination probability was developed. This can then be written as :

$$r(E) = \text{erf} (E/p_1) \left(p_2 \times e^{-E/p_3} + p_4 \right) \quad (2.27)$$

where erf is the error function, E is the kinetic energy, and p_1, p_2, p_3, p_4 are free parameters which are extracted from the fit of DS-50 data.

Chapter 3

Background Sources

This chapter attempts to outline some of the sources of background present in the DS-50 detector. Perhaps the most important aspect of a WIMP search detector is to understand and characterize the various backgrounds such that the detection of a WIMP would be incompatible with a background-only hypothesis. There are primarily two categories of backgrounds, radiogenic and cosmogenic. Particular attention is paid to the backgrounds of cosmic origin and the Monte-Carlo simulation performed to assess the efficiency to veto them.

3.1 Radiogenic Backgrounds

Radiogenic backgrounds arise from radioactivity within the detector materials and the target itself. These broadly consist of surface backgrounds, neutron backgrounds and electron recoil backgrounds. Surface background mainly consist of α decays and a thorough description of them has been documented [87]. Neutron backgrounds of radiogenic origin typically arise from (α, n) reactions in various components of the detector. These backgrounds have also been well documented [66].

Nonetheless it is worthwhile to give an overview of some of the backgrounds and their rates.

Electron Recoil Backgrounds

Electron recoil (ER) events in DS-50 are found to be generated by β decay in the liquid argon active volume or from Compton scattering of γ rays from radioactive decays. The mechanism of LAr scintillation has been discussed in Section 2.1.1.

Pulse shape discrimination (PSD) is a powerful tool to distinguish between ER and NR events. One does not expect a large background in a WIMP search from events like β decays. On the other hand, γ rays could potentially have a sufficiently high rate producing signals in the TPC and LSV. Calibrating the inner and outer detectors based on these γ ray signals helps achieve a background-free experiment.

One potentially dangerous class of backgrounds is the combination of Cherenkov radiation, produced in either of the Teflon or fused silica windows, and a regular ER-like scintillation pulse. These backgrounds have been well studied, modeled and measures to suppress them have been developed [88, 89].

3.1.1 ^{39}Ar

For typical LAr based experiments, one of the dominant backgrounds comes from ^{39}Ar . This radioactive isotope β decays with an endpoint energy of 565 keV and a half life of 269 years [90]. This background is internal to the Argon in the TPC and even though it is in the WIMP energy range of interest, it can be removed easily by making use of PSD. In addition, a high contamination of ^{39}Ar leads to the possibility of pileup of the ^{39}Ar decays, thus reducing the livetime of the detector. For dual phase TPCs like DS-50, two pulses separated by a few μs are typically seen for each event. Thus long acquisition windows are required and the loss of livetime can become a problem for large fiducial masses. DS-50 measured the argon extracted from the atmosphere to have an ^{39}Ar activity of ~ 1 Bq/Kg

[35].

Argon is the most abundant element in the Earth's atmosphere after nitrogen and oxygen. Most of the ^{39}Ar in AAr is produced by interaction of cosmic rays with ^{40}Ar via :



High rates of ^{39}Ar decays can be relieved by employing argon derived from underground sources (UAr), where the reduction in activity as compared to AAr has been measured by the DarkSide collaboration to be $(1.4 \pm 0.2) \times 10^3$ [51].

Shown below is the beta decay scheme for ^{39}Ar .



This reaction flips the parity of the nucleus and changes the angular momentum by 2 so it is labeled a first forbidden beta decay resulting in its long half life.

3.1.2 ^{85}Kr

^{85}Kr is typically produced by cosmogenic neutron activation on ^{84}Kr in the atmosphere. DS-50 reported the activity of ^{85}Kr in UAr to be ~ 2 mBq/kg [51]. The presence of ^{85}Kr was unexpected and there was no evidence found of its existence in the AAr run. The primary mode of decay of ^{85}Kr leads to the ground state of ^{85}Rb via a beta decay process, the endpoint energy of which is 687 keV. Since the endpoint energy for ^{85}Kr is greater than that of ^{39}Ar , a high enough concentration can mask the latter's existence. ^{85}Kr can also decay to ^{85m}Rb with a 0.434% branching ratio and an endpoint energy of 173 keV. The product further decays to the ground state ^{85}Rb with the emission of a γ ray and a half

life of $\sim 1\mu\text{s}$. The coincident, but separable, signals of the γ and the β allow for a clear identification of these events in the TPC [57]. See Figure 3.1 for the decay scheme of ^{85}Kr .

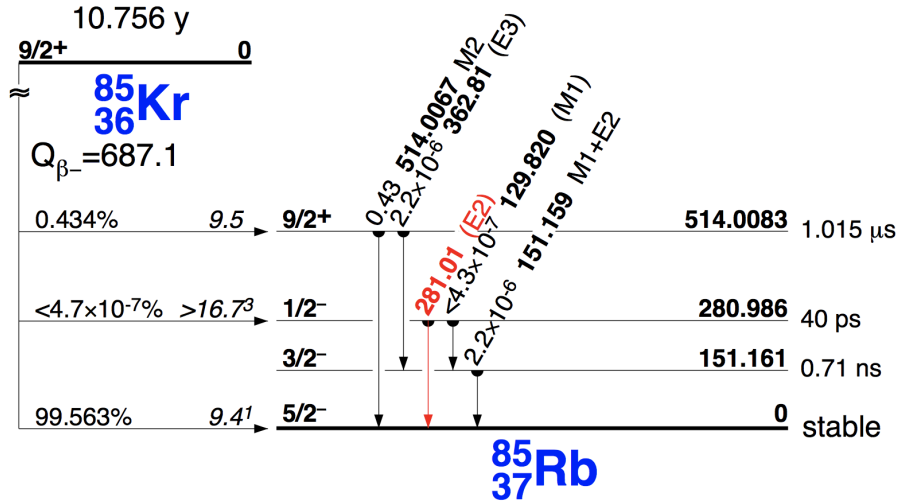


Figure 3.1: The decay scheme of ^{85}Kr . Figure taken from [57].

3.1.3 ^{238}U

^{238}U is a primordial radionuclide, with a natural abundance of 99.27% and half-life of 4.5×10^9 yr. It is present in soil with a median activity concentration of 35 Bq/kg, which varies with location (e.g., soils from igneous sources tend to have higher activities). ^{238}U can undergo spontaneous fission with a branching ratio of 5.45×10^{-7} , producing an average of 2.01 neutrons per decay that may then scatter in the TPC. Also, α -decay in the ^{238}U decay chain is a source of neutrons from subsequent (α, n) reactions.

Secular equilibrium

When the daughter (d) of a parent radionuclide (p) is itself radioactive, the decay rate of the daughter can be described by the Bateman equation:

$$\frac{dN_d}{dt} = \lambda_p N_p - \lambda_d N_d \quad (3.3)$$

where N is the number of each nuclide, and λ its decay constant. Recall that

$$N_p = N_{0p}e^{-\lambda_p t} \quad (3.4)$$

where N_{0p} is the initial number parent nuclides. This leads to a first-order linear ordinary differential equation

$$\frac{dN_d}{dt} + \lambda_d N_d = \lambda_p N_{0p} e^{-\lambda_p t} \quad (3.5)$$

which can be solved as follows :

$$N_d = e^{-\lambda_d t} \int e^{\lambda_d t} \lambda_p N_{0p} e^{-\lambda_p t} dt = \frac{\lambda_p}{\lambda_d - \lambda_p} N_{0p} \left(e^{-\lambda_p t} - e^{-\lambda_d t} \right) \quad (3.6)$$

assuming no daughter nuclides are initially present.

If the half-life of the parent is much longer than that of its daughter ($\lambda_p \ll \lambda_d$), N_d becomes dependent on the decay of only the parent nuclide after several half-lives of the daughter:

$$N_d \rightarrow \frac{\lambda_p}{\lambda_d - \lambda_p} N_{0p} e^{-\lambda_p t} \approx \frac{\lambda_p}{\lambda_d} N_{0p} e^{-\lambda_p t} \quad (3.7)$$

Substituting equation 3.7 into equation 3.5 shows that $\frac{dN}{dt} = 0$ in this situation, known as secular equilibrium.

Since daughter decays now occur at the same rate as that of the parent, the same reasoning can be applied to subsequent daughters (as long as their respective half-lives are shorter than the parent) to show that the entire decay chain can be in secular equilibrium with its parent radionuclide. This is the case for ^{238}U , whose half-life is much longer than that of any of its daughters (the longest of which $2.5 \times 10^5 \text{ yr}$ is for ^{234}U). The same applies to ^{235}U and ^{232}Th . ^{238}U is present in the DS-50 stainless steel cryostat as well as components of the PMTs.

3.1.4 ^{235}U

^{235}U is also primordial radionuclide, with a natural abundance of 0.72% and half-life of 7.0×10^8 yr [44]. The activity ratio with respect to ^{238}U is 0.046. Germanium counting of ^{235}U identifies the 143 keV and 185 keV γ -rays from ^{235}U decay. The entire ^{235}U decay chain is assumed to be in secular equilibrium. The ^{235}U decay chain mostly produces low energy γ -rays. High energy γ -rays (>1 MeV) can be produced by ^{215}Bi decay, however the branching ratio is $1.38\% \times 0.006\% \times 97\% = 0.00008\%$. ^{235}U can undergo spontaneous fission with a branching ratio of 2.011×10^{-9} , producing an average of 1.86 neutrons per decay that may then scatter in the TPC. In the ^{238}U decay chain, α -decay is also a source of neutrons from subsequent (α, n) reactions. ^{235}U is present in the DS-50 stainless steel cryostat as well as components of the PMTs.

3.1.4.1 ^{60}Co

^{60}Co is a synthetic isotope of cobalt with a half life of 5.27 years. ^{60}Co produces two high energy γ - rays and hence it finds use in radioactive tagging. ^{60}Co typically β decays through the reaction



The two γ rays in the decay of ^{60}Co are produced by two different de-excitations and therefore their momenta are not correlated. These rays are produced in coincidence with each other, making this the strongest signal in prompt coincidence between the TPC and LSV. ^{60}Co is present in the DS-50 stainless steel cryostat as well as components of the PMTs.

3.1.5 ^{232}Th

^{232}Th is a primordial radionuclide with a half life of 1.4×10^{10} yr. It is present in the crust of the Earth with a concentration of ~ 9.6 ppm. Since it is found in rock, small amounts of ^{232}Th are typically found in most metals. The decay chain of ^{232}Th ends with the stable ^{208}Pb . We assume that the chain is in secular equilibrium and have not found contradictory evidence. ^{232}Th undergoes spontaneous fission with a branching ratio of 1.4×10^{-11} which results in ~ 2.1 neutrons per decay which have the potential to scatter in the sensitive liquid argon volume. γ rays are associated with the fission neutrons. The highest γ energy is 2.6 MeV from the decay of ^{208}Tl . There are also many α emitters in the decay chain and this may result in further (α, n) reactions, possibly producing fast neutrons. ^{232}Th is present in the DS-50 stainless steel cryostat as well as components of the PMTs.

3.2 Cosmogenic Backgrounds

This section presents the use of a Monte-Carlo based simulation to study muon-induced, cosmogenic backgrounds for the DS-50 experiment.

Muons can generate backgrounds by producing showers of secondary particles with interactions with the rock in the vicinity of the detector. Typically only high energy muons are able to penetrate to the depth of the experimental halls, and hence the total muon flux decreases since the low energy muons, which are more intense, are removed from the spectrum. As a result, the mean energy of the surviving muons increases with depth.

Scarce experimental information about muon-induced secondaries at depth is available. Many earlier studies focused on the neutron flux in the muon radiation field. Low rates and difficulties in measuring neutrons make it challenging to interpret the available data.

Previously [91], it had been suggested to study the neutron production deep underground

to understand the incident muon flux. But such measurements were limited to cosmogenic neutrons typically in liquid scintillator detectors. The flux was calculated by measuring the gamma radiation after neutron capture in the scintillator. Many uncertainties, mostly systematic in nature, associated with detector geometry and efficiency corrections make it formidable to interpret the data correctly.

3.2.1 Neutron Production Mechanisms

- **μ^- capture**

Negative muon capture, which is an electro-weak charge current interaction, has a cross section that is sensitive to the muon kinetic energy. For kinetic energies greater than the muon binding energy, the capture cross section falls sharply. This process is dominant at depths of ≤ 100 metres of water equivalent (m.w.e).

- **Muon-induced spallation of a nucleus**

If a muon inelastically scatters with a nucleus via exchange of a virtual photon, it is referred to as muon spallation. The excited nucleus disintegrates producing neutrons and other daughter particles. This process is dominant when the transfer energy is < 0.3 GeV.

- **Muon-induced hadronic cascade**

Hadronic cascades are produced as a result of high energy transfer in a muon spallation reaction. Typically hadronic cascades consist of pions, kaons and nucleons $[\pi^\pm, \pi^0, K^\pm, K^0]$.

Shower hadrons, which are primarily charged pions, typically have energies corresponding to $\beta > 0.7$. They generally retain the direction of muon propagation. Cascade hadrons (also called recoil nucleons) have energies corresponding to $0.2 < \beta < 0.7$. They are generally nucleons produced in pion-nucleus and nucleon-nucleus collisions. They have a broad angular distribution with respect to the muon track. Evaporated

nucleons with $\beta < 0.2$ are produced when cascade particles produce additional nucleons at lower energies. They have an isotropic angular distribution and are produced after the nucleons are thermalized and captured by surrounding matter.

- **Muon-induced electromagnetic cascades**

EM cascades originate with δ electrons, e^-e^+ pairs and bremsstrahlung photons. Neutrons resulting from EM showers are produced primarily by the photo-production reaction (γ, n) through nuclear giant resonances. The only difference between this process and muon-induced nuclear spallation is the exchange of a real photon as opposed to a virtual one. Neutrons could also be generated by multiple photo-production mechanics i.e. (γ, xn) . The production of shower photons is inversely proportional to the square of the energy of the photon, thus neutrons generated by EM showers are typically done by low energy photons. Alternatively, neutrons can be produced in inelastic charge exchange reactions such as :

$$\gamma + p \rightarrow n + \pi^+$$

$$\gamma + (Z, A) \rightarrow (Z - 1, A - 1) + n + \pi^+$$

or in the pion photo-production reaction:

$$\gamma + (Z, A) \rightarrow (Z, A) + \pi^+\pi^-$$

which is then followed by pion capture :

$$\pi^- + (Z, A) \rightarrow (Z - 1, A - 1) + n$$

The inelastic charge exchange and pion photo-production mechanisms require high γ energies > 140 MeV. Thus the contribution of these two mechanisms is negligible compared to the rate of direct neutron production, however, they do contribute to the high energy end of the neutron spectrum.

3.2.2 The FLUKA Code

FLUKA [92,93] is a fully integrated particle-physics, Monte Carlo simulation package, originally developed for the design of shielding of particle accelerators. Recently it has been applied in high energy particle physics, medical physics, radio-biology, and astrophysics. Design and development of FLUKA is based on the implementation of verified microscopic models of physical processes. FLUKA utilizes these models such that consistency is maintained at all steps of all reactions. Predictions are bench-marked against experimental data. A consistent approach to all energy/target/projectile combinations is provided with a minimum set of free parameters. Hence predictions for complex simulations problems arise from underlying physical models and are typically reliable.

The version of FLUKA used for the presented study is FLUKA2011.2, from November 2011.

3.2.3 Physics Models in FLUKA

Hadron-nucleon interactions at energies < 5 GeV are simulated by a model based on individual resonance production and decay while also considering charge and strangeness exchange. At high energies, this interaction is described by a model based on the dual parton model (DPM) [94]. The mechanism for multiple production in hadron interactions is described by this model. Hadron-nuclear interactions are described by the Glauber-Gribov formalism [95,96] at high energies, while at low energies, the PEANUT model is used. The Glauber-Gribov model effectively calculates the elastic and absorption hadron-nuclear cross section from the nuclear ground state and the free hadron-nucleon interaction [97]. Nucleus-nucleus collisions for energies > 5 GeV per nucleon are simulated using a series of models DPMJET [98], which are based on the DPM and the Glauber formalism.

The relative quantum dynamics model (RQMD) [99,100] is employed to simulate reactions when the energy range per nucleon is between 0.1 GeV and 5 GeV . For lower energies

(< 100 MeV per nucleon), the Boltzmann master equation [101] is utilized.

Electromagnetic interactions in FLUKA are part of EMF (Electro-Magnetic FLUKA). All interactions in the EM sector including photo-nuclear interactions are carried out by the transport of electrons and photons. FLUKA has the ability to propagate electrons and photons in a very large energy range (1 keV to 1 PeV). The electromagnetic interactions are linked with the hadronic interactions, such that production of photons and electrons in the hadronic sector are subsequently handed off to EMF to complete the reactions. Electron pairs and bremsstrahlung radiation are sampled from the energy angular spectra.

The differential cross section of the muon spallation is calculated via the Berzukov-Bugaev model [102]. This model treats the photo-nuclear interaction using the Williams-Weizsacker approximation where the trajectory of a charged lepton in a material replicates the passage of a beam of virtual photons. This model also employs the generalized vector dominance model to calculate the cross section for photon-nucleus interactions and consequently for muon-nucleus interactions.

To summarize:

Production of cosmogenic neutrons in FLUKA is the result of direct muon nuclear interactions, photo-nuclear reactions by real photons in electromagnetic showers, and in nuclear cascades within resulting hadronic showers. Direct muon-nuclear interactions are modeled by μ^- capture at rest, and by virtual photo-nuclear interactions.

Photon-nucleus reactions are simulated over the entire energy range through different mechanisms:

- Giant Resonances interaction,
- Quasi-Deuteron effect,
- Delta Resonances production, and

- Vector Meson Dominance at high energies.

Hadron-nuclear interactions are described by utilizing models dependent on energy of the projectile. The FLUKA nuclear interaction model called PEANUT can be described as a sequence which follows:

- Glauber-Gribov cascade in high energy collisions,
- Generalized-Intra-Nuclear cascade,
- Pre-equilibrium emission, and
- Evaporation/Fragmentation/Fission and de-excitation.

Although steps may be abandoned depending on the projectile energy and type, PEANUT is an accurate tool for intermediate energy hadron-nucleus reactions. Its “nuclear environment“ is also used in the simulation of real and virtual photo-nuclear reactions, neutrino interactions, nucleon decays and muon captures. All nuclear fragments are de-excited through a similar evaporation/fragmentation and gamma production chain. Validation of the FLUKA Monte Carlo code for predicting induced radioactivity has been recorded [103].

3.2.4 Physics Related User Options

The physics models in FLUKA are fully integrated into the code, and the individual models are validated by experimental data. The user is presented with an optimized configuration of models which cannot be further modified.

The simulation described hereon, was executed with the FLUKA setting PRECISIO(n). Photo-nuclear interactions were enabled through the FLUKA option PHOTONUC and the detailed treatment of nuclear de-excitation was also enabled with the EVAPORAT(ion) and COALESCE(nce) options. EVAPORAT(ion) allows for the evaporation of heavy fragments ($A > 1$) while COALESCE(nce) allows for emission of energetic light fragments. These

options are utilized to obtain accurate results for isotope production. The treatment of nucleus-nucleus interactions was also enabled for all energies via the option IONTRANS, and delayed reactions were enabled using the option, RADDECAY.

Neutron captures on hydrogen inside liquid scintillator are also recorded in order to evaluate the muon-induced neutron production rate.

3.3 Cosmogenic Background Simulation at LNGS

A complete simulation of the muon radiation field for an underground WIMP detection experiment must contain details of the depth, overburden geometry and composition of the rock in the vicinity of the detector through which the muons travel through and interact. A sufficiently accurate geometry of the detector must be replicated in order to have accurate results for the simulation.

This study, as it is based on [73], contains multi-muon events. It improves the description of the radiation field compared to previous studies.

3.3.1 Muon Radiation Field

3.3.1.1 Intensity

The muon flux in the 3 halls at Laboratori Nazionali del Gran Sasso (LNGS) is summarized by the Borexino collaboration [104]. The measured flux describes the total cosmogenic muon event rate. Variations in muon flux between the measurements given in Table 3.1 may be attributed to the relative location of the halls within the laboratory and the systematic uncertainties associated with the measurements. The value measured by the Borexino collaboration in table 3.1 is chosen for this simulation.

Table 3.1: Measured muon flux at the three different experimental halls at LNGS. Taken from [73].

experiment	Hall	year published	total muon event rate ($\times 10^{-4} s^{-1} m^{-2}$)
LVD	A	2009	3.31 \pm 0.03
MACRO	B	2002	3.22 \pm 0.08
Borexino	C	2012	3.41 \pm 0.01

3.3.1.2 Mean energy and differential energy spectrum

The underground muon kinetic energy spectrum can be represented by the equation :

$$\frac{dN}{dE_\mu} = C \cdot \left(E_\mu + \varepsilon \left(1 - e^{-\beta h} \right) \right)^{-\alpha} \quad (3.9)$$

In the above equation , E_μ represents the muon kinetic energy at slant depth h (which is just the atmospheric depth scaled by $1/\cos(q)$, q being the angle subtended by the vertical) while α represents the surface muon spectral index [105], β and ε describe energy loss mechanisms in rock, and C is a constant.

The average muon kinetic energy at slant depth h is:

$$\langle E_\mu \rangle = \frac{\varepsilon (1 - e^{-\beta h})}{\alpha - 2} \quad (3.10)$$

Results for the the mean muon energy and the spectral index α for LNGS were measured by the MACRO collaboration [106] and are shown in Table 3.2:

Table 3.2: The mean energy of single and double muon events as measured by MACRO. Taken from [73].

event type	mean muon energy (GeV)	spectral index α
single muon	270 \pm 3 <i>(stat)</i> \pm 18 <i>(syst)</i>	3.79 \pm 0.02 <i>(stat)</i> \pm 0.11 <i>(syst)</i>
double muon	381 \pm 13 <i>(stat)</i> \pm 21 <i>(syst)</i>	3.25 \pm 0.06 <i>(stat)</i> \pm 0.07 <i>(syst)</i>

The description of the energy spectrum given by equation 3.3.1.2 allows for direct sampling because it is both integrable and invertible in analytic fashion. If one uses the values

of $\varepsilon = 0.392 \times 10^{-3}$ and $\beta = 635$ GeV, one is able to reproduce the measured mean energy for single and double muon events, while the mean residual energy of muons is found to be 283 ± 19 GeV at LNGS.

3.3.1.3 Angular Distribution

Both the azimuthal and zenith angles play a role in determining the slant depth h ($g\text{ cm}^{-2}$) of the muon trajectory through the rock. The azimuthal component of the angular dependence of the slant depth depends on the contour of the Gran Sasso mountain. Therefore the incident direction of the muons is a variable of the function which determines the intensity and energy of the muons entering the detector setup.

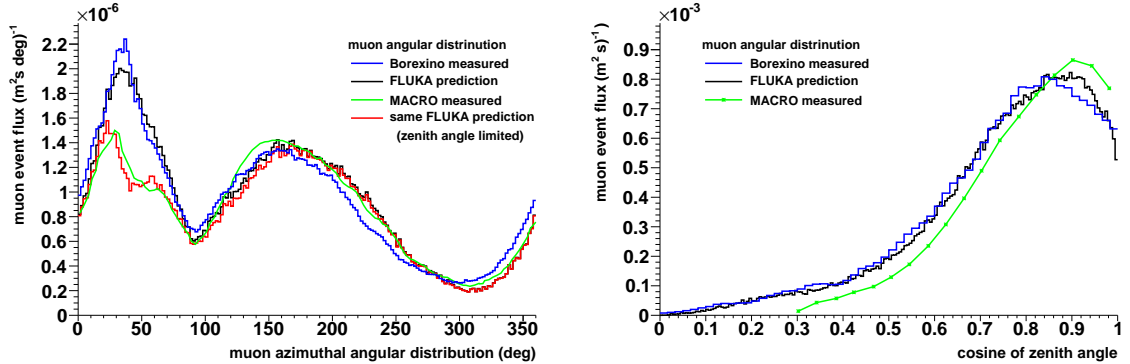


Figure 3.2: Muon azimuthal (left) and zenith (right) angular distribution at LNGS for polar coordinate system pointing up and North with clockwise increasing angle. The figure shows Borexino data (blue), MACRO data (green) and FLUKA predictions (black, red indicates zenith angle limited). Figure taken from [73].

The MACRO collaboration performed a measurement of the muon angular distribution at Hall B of LNGS [107]. Azimuthal (left) and zenith (right) projections of the distribution are shown by the green histograms in Figure 3.2.

The MACRO measurement is compared to the results from the Borexino collaboration [108] (blue histograms). The difference in the experimental azimuthal spectra for angles near $\frac{\pi}{4}$ radians is due to a limit in the angular acceptance of approximately $\frac{\pi}{3}$ radians in the zenith angle in MACRO. These data are compared to a FLUKA simulation which traced

muons, initiated by cosmic rays in the upper atmosphere, to the experimental halls [109], and was normalized to the muon flux measured by Borexino which accounts for detector efficiency. The predictions for full detector acceptance are shown by the black histograms in Figure 3.2.

When the constraint of the zenith angle in MACRO is replicated in the FLUKA based simulation, the features found in data are replicated. The resulting azimuthal spectrum is shown by the red histogram. Reasonable agreement is found between data and simulation. The small difference in locations for the MACRO and Borexino experiments results in a visible shift in the azimuthal distribution.

3.3.1.4 Bundles

Muon bundles at LNGS were investigated by the LVD and MACRO collaborations. The results shown have been taken from [110]. Figure 3.3 shows the measured muon multiplicity (left) and the spatial separation between muons for double muon events (right). A simulation to study muon multiplicity used simplified sampling of the distribution up to a muon multiplicity of 4. The distance between muons within a bundle was chosen according to the distribution measured for double muon events and all muons within a bundle are given the same direction.

The effect of multi-muon events for the Borexino detector geometry was evaluated assuming the measured multi-muon event rate from MACRO of approximately 6%. Close to 1.5% of the muon events in Borexino feature more than one muon. In addition, about 12% of the single muons crossing the Borexino inner detector belong to multi-muon events.

3.3.1.5 Event generation

In order to simulate the muon flux in Hall C at LNGS, one selects the azimuthal and zenith angles according to the measured muon angular distribution. A map of the Gran

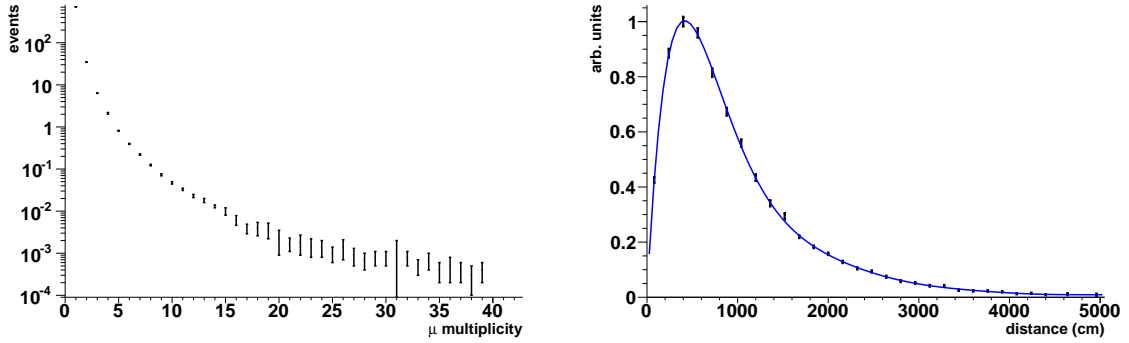


Figure 3.3: (left) Multiplicity of muons recorded by the MACRO detector for cosmogenic muon events. (right) Spatial separation of muons obtained for cosmogenic events in the MACRO detector featuring two coincident muons (black data points). The blue line shows a simple higher order polynomial fit used to implement sampling of the distribution. Figure taken from [73]

Sasso mountain overburden, constructed by the MACRO collaboration [109], was used to convert the muon incident direction into the slant depth h . In the next step, the event type is chosen to be a single muon or multi-muon bundle. If the latter choice is made, a maximum multiplicity of 4 was allowed and sampled from the measured multiplicity spectrum since the probability for muon events with larger multiplicities is less than 0.2%.

Finally, the muon kinetic energy as a function of slant depth h and muon event type was chosen by sampling from the parameterized single or double muon event energy spectra. For muon bundle events of all multiplicities, the double muon event energy spectra is assumed since experimental information for events with higher multiplicities is unavailable.

A constant charge ratio of $N_{\mu^+/\mu^-} = 1.38$ was selected to simplify the simulation. This value is consistent with the weighted average of the reported measurements for single and multi-muon events by OPERA [111]: $R_{single} = 1.395 \pm 0.025$ and $R_{multi} = 1.23 \pm 0.1$.

3.3.2 Muon-induced Secondaries

The cosmogenic radiation field at deep underground sites is composed of muons and muon-induced secondaries. Incident muons are permitted to develop particle showers as

they pass through a 7 m thick layer of Gran Sasso rock [112] surrounding all 4 sides and the top of Hall C. The amount of rock to fully develop the shower was determined by simulation [73,113]. Particle production rates for muons of 280 GeV kinetic energy in Gran Sasso rock are shown in Figure 3.4 (left).

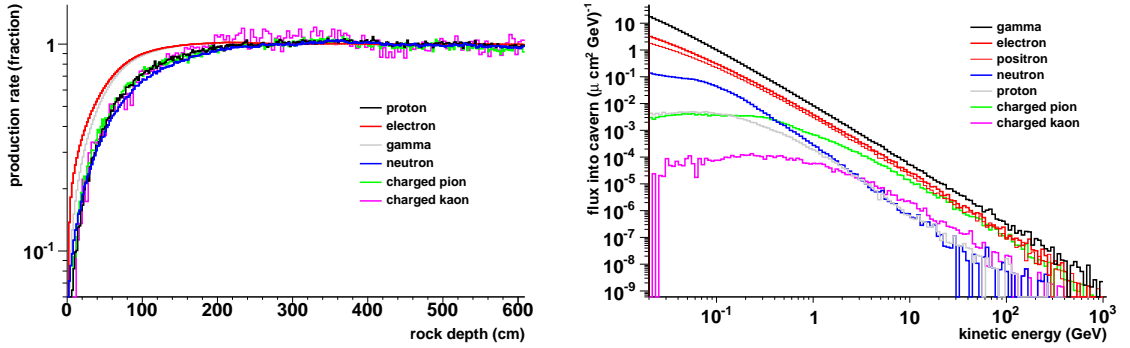


Figure 3.4: (left) Particle production rates by 280 GeV muons in Gran Sasso rock as function of distance travelled. The rates are normalized per particle species to the maximum production rate. (right) Predicted integral particle flux into Hall C at LNGS per cosmogenic muon event given as a function of particle kinetic energy. Figures and caption taken from [73]

Muon events are randomly positioned on a large plane placed above the hall geometry such that the the hall containing the detector is completely illuminated. Muon tracks outside this envelope are rejected.

3.3.2.1 Propagation through rock

The cosmogenic radiation at the cavern walls is approximated in two separate technical steps to save computation time. For the first step, the muon radiation field is reproduced on a rock layer surrounding Hall C, and it is allowed to propagate through the rock without any interactions. The muons which were tracked as entering the hall, were recorded. For high energy muons, the muon trajectory is relatively unhindered by interactions, and these stored muons were chosen as the muon sample for the simulation. These muons were then propagated a second time with all physics processes turned on such that a realistic

description of the cosmogenic radiation, along with all generated secondary particles, could be obtained. The secondary particles were stored along with the initially incident muons. The sampled muon kinetic energy was adjusted for the average muon energy loss in the rock layer.

3.3.2.2 Particle components of the muon-induced radiation field

High energy muons produce several kinds of particles including neutrons. These particles, including the primary muon, can continue to produce backgrounds as they interact with the detector and its surroundings. Figure 3.4 (right) shows the kinetic energy spectra for the most frequently produced secondary particles. Photo-production can also contribute to backgrounds, including neutron backgrounds, because of the large photon flux even though electromagnetic cross sections are not large. Thus, to assess cosmogenic backgrounds, the complete muon-induced radiation field needs to be considered as opposed to simulating only cosmogenic neutrons.

3.3.3 Connection of Simulation to Measured Muon Event Flux

For each simulated event the muon field, denoted by Φ_{sim} , interacts with the detector and shielding. The length of the time-period considered in the simulation, also known as livetime, is determined by the number of simulated muon events compared to the ratio of the simulated to measured total muon flux, Φ_{exp} , from Table 3.1.

$$T[s] = N_{events} \cdot \frac{\Phi_{sim}[events^{-1}cm^{-2}]}{\Phi_{exp}[s^{-1}cm^{-2}]} \quad (3.11)$$

The procedure for determining this can be found in [73].

3.4 Validation

3.4.1 The Borexino Experiment

The most precise experimental data on cosmogenic neutrons deep underground, and a FLUKA simulation based on these data, are available from the Borexino collaboration [108]. The low systematic uncertainties on the data are a result of the size of the detector with its shielded and un-segmented spherical liquid scintillator target. Borexino also has a comparatively short recovery time from the large, prompt muon signal. This permits less accidental background between the muon signal and the neutron capture signals.

3.4.1.1 Distance between neutron capture location and muon track

When a muon enters a detector filled with liquid scintillator, a large initial signal is created and hence it is difficult to retrieve the prompt neutron yield. Borexino allows for spatial reconstruction of the muon track and the delayed neutron capture locations. This permits a study of the transverse distance that neutrons may travel perpendicular to the initial muon track.

3.4.1.2 Neutron multiplicity

In Figure 3.5 the multiplicity of thermal neutron captures per muon-induced cosmogenic event is shown. The Borexino experimental result (red symbols) and the FLUKA predicted distributions (black histogram) from are shown in the graph on the left.

The bias seen at large multiplicities is primarily because of the performance of the detector in the case of muon bundle events. The simulation [73] best replicated this effect by selecting events which only had single muon tracks entering the Borexino inner volume. The shape of the distribution agrees well, other than very low neutron multiplicity events.

“Hard” energy losses by energetic muons are likely to be initiated by muon bremsstrahlung and muon-nuclear interactions. The dashed green line shows the contribution to the neutron multiplicity spectrum by muon bremsstrahlung and muon-nuclear interactions. Contrarily, “soft” energy losses advance via electron pair and delta electron production. This contribution is shown by the dashed blue line.

The graph on the right in Figure 3.5 shows the ratio of the individual muon interaction types which result in the capture of cosmogenic neutrons as a function of neutron capture multiplicity. $\sim 90\%$ of the events with a single neutron capture are initiated by muons after delta electron production or electron pair production.

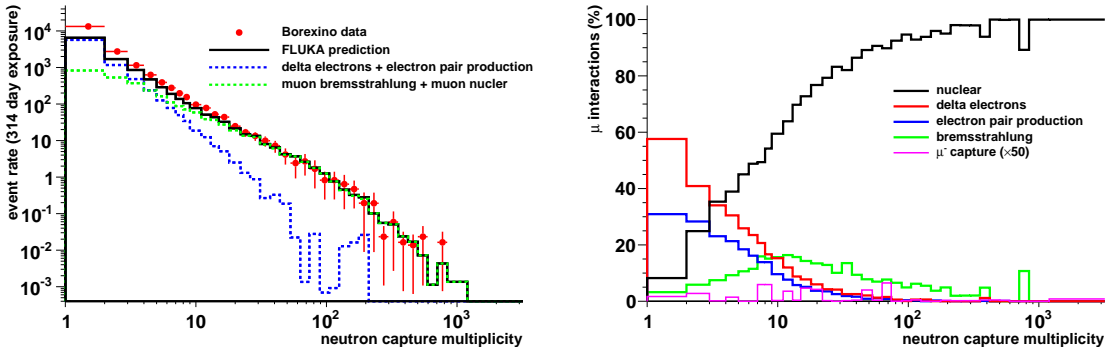


Figure 3.5: (left) Absolute comparison of muon-induced cosmogenic thermal neutron capture multiplicity as measured by Borexino, red symbols, and predicted by FLUKA, black histogram. For the simulated spectrum contributions from muon interactions associated with “soft” (dashed blue line) and “hard” (dashed green line) energy loss processes are shown separately. (right) Fractions of different muon interactions which trigger the production of neutrons in liquid scintillator as a function of neutron capture multiplicity. The fraction of μ^- capture is magnified by a factor of 50 for visibility. Figure and caption taken directly from [73]

3.4.1.3 Muon rate producing neutrons

The rate of cosmogenic muon events resulting in one or more thermal neutron captures in Borexino is 67 ± 1 per day. The corresponding FLUKA simulated rate of 41 ± 3 per day is comparatively low. The difference is mainly due to muon events with very low neutron capture multiplicities as seen in Figure 3.5 on the left.

FLUKA suggests that these events are principally triggered by muon electron pair and delta electron creation, which generally yield neutrons with a “softer” energy spectrum. Moreover, neutrons created in muon events with low neutron multiplicity, capture close to the parent track [73].

Thus, even though the FLUKA predicted neutron event rate is approximately 30% lower, the category of affected neutrons is not very critical with the perspective of cosmogenic background reduction. Also since the only events affected are those with low neutron multiplicities, the overall effect on the neutron yield is not so significant.

3.5 Cosmogenic Neutron Background for DS-50

This section describes the procedure employed to simulate the background arising from cosmogenic events for DS-50 and therein the obtained results.

3.5.1 Simulation Procedure

At this point, having obtained the entire flux of events with muons and their secondaries at the boundary of Hall-C we are able to estimate quantities of interest; i.e the efficiency of the DS-50 veto system to reject cosmogenic events that may mimic WIMP like signals in the LAr.

We require the geometry to be implemented as close as possible to the physical detector setup, and an effort has been made to replicate it. Figure 3.6 shows the implemented geometry in FLUKA.

The first step of the simulation in FLUKA involves simply propagating all the events from the ceiling of Hall-C onto the water tank also referred to as the CTF. Events at the geometrical boundary of the CTF are examined, and those which had at least one particle entering the volume were selected for further propagation while the rest were discarded.

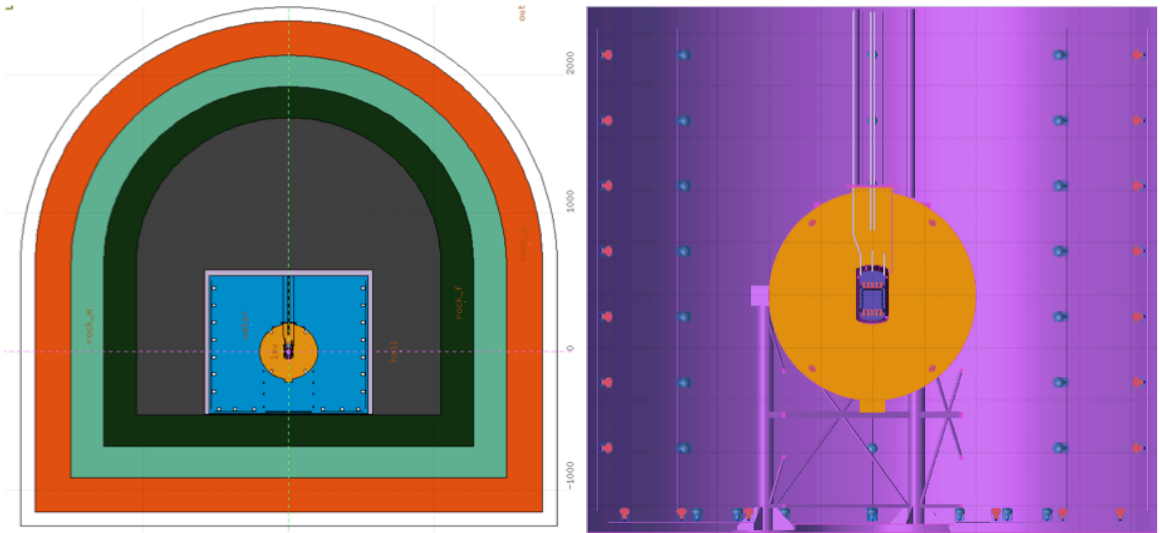


Figure 3.6: Geometry description in FLUKA. (left) The detector setup viewed along the direction of Hall-C at LNGS; (right) A close up of the detector setup within the water tank.

It is worth mentioning that there is a non zero probability that an event with a neutron which does not enter the CTF is discarded in this rejection process, but such neutrons would be thermalized after entering and would not be problematic, as they would eventually get captured in the LSV (see Section 2.4.). On an event-by-event basis the total raw (unquenched) energy deposited in each of the detectors is collected. There are no optical processes involved at this stage of the simulation.

A simple calculation via the Frank-Tamm equation tells us that the number of photons produced via the Cherenkov effect of a muon traveling in water with an energy of ~ 2 GeV would be over 300/cm. It is a reasonable and conservative assumption to discard events which had a muon with an energy > 4 GeV and a physical track length of over 200 cm in water since they would produce more than sufficient light for the event to be classified as cosmogenic and hence it would not be problematic even if a potential WIMP-like signal was seen in the TPC by a single entering neutron. We will later see that these events are extremely computationally intensive to simulate and not worth processing only to determine veto efficiency.

We have a fairly well described simulated dataset at this point and are able to see on an

event-by-event basis, the particles that entered the TPC, and the raw energy deposited (dE) in each detector i.e. the TPC, the LSV and the CTF. If there was a neutron in the sensitive volume, a look at the energy deposited in the outer detectors can give some information about whether we would have vetoed that event or not. For example, a deposit of 1 MeV or higher is a significant amount of raw energy deposited in the LSV which has a light yield of ~ 0.5 PE/keV, allowing the event to be easily detected in the LSV. Many such events are vetoed solely based on this criterion.

Now for events which were tracked as entering the LSV, the simulation re-propagates these events from their incoming locations outside the water tank, this time with optical processes, namely Cherenkov radiation, turned on in the water (See Figure 3.7 for a visual of the optical photon fluence for a set of muon events going through the water tank). Of course it is noteworthy that the events that made it into the LSV during the first run, may not make their way in again since the random seeds are not the same, but this is a conservative approach. Turning on Cherenkov optics for all events from outside the water tank would be extremely time consuming (computationally) and not all such events are dangerous. The only events that have a potential to produce a false positive are the ones that have at least one particle entering the LSV - which is quite a conservative approach. But if Cherenkov radiation was only turned on for events that made their way into the sensitive volume, there could be a chance of underestimating the background. This is simply because the ratio of events that reach the sensitive volume to the number of events at the cavern walls is extremely low. Therefore this potentially aggressive approach was avoided.

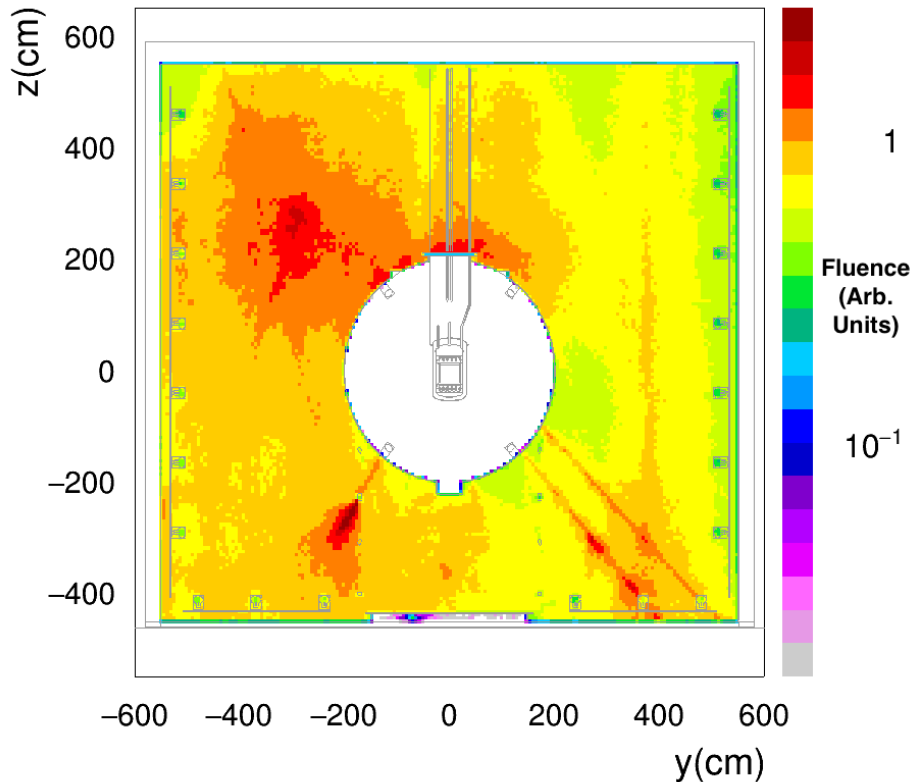


Figure 3.7: Cross sectional view of fluence of optical photons in the setup for a set of 13 simulated muon events. The fluence depicted is calculated by integrating in the x direction

As mentioned previously in [58, 66], the LSV is covered on the outside with sheets of Tyvek while the same is true for the inner surface of the water tank. The reflectivity of Tyvek in the relevant wavelength region has been measure to be 99%. As a conservative approach, the reflectivity was set to be 80%.

The PMTs have a light collection efficiency which was set to 70%, as measured [114]. The PMTs also have a wavelength dependent quantum efficiency (QE) which is extracted from [114] and subsequently implemented in this simulation (see Figure 3.8). The QE achieves it's maximum 26% for a wavelength of ~ 400 nm. The geometry of the PMTs is modeled after the 8 inch ETL PMTs. It is also necessary to set the correct absorption coefficients for the water. After all these steps have been implemented, the machinery is truly ready to

produce meaningful estimates.

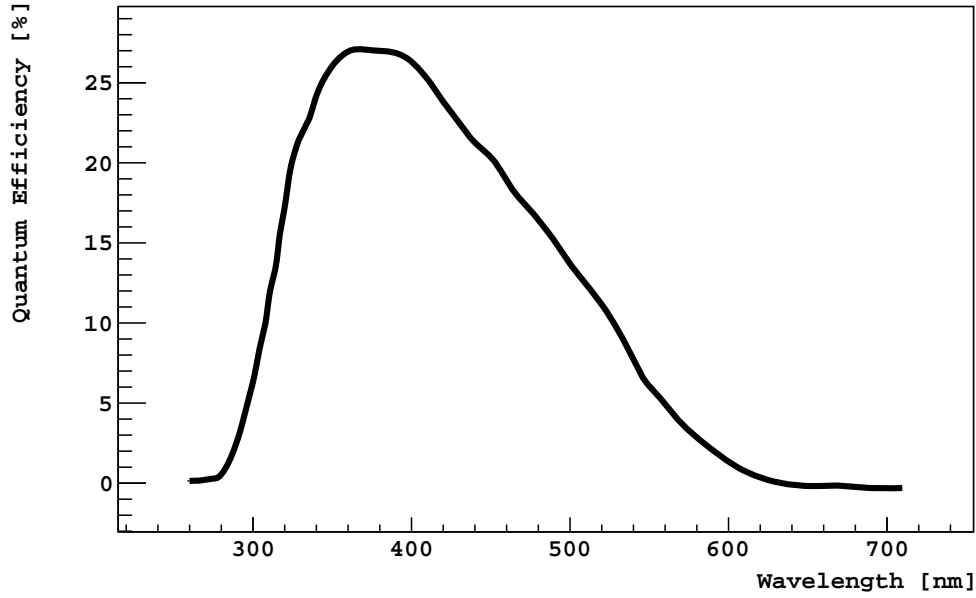


Figure 3.8: The approximate Quantum Efficiency (as a function of wavelength) of the PMTs in the Water Tank as implemented in the simulation.

3.5.2 Results

In this section, the basic results obtained from simulation are reported. In particular, the efficiency of the veto system is evaluated and compared to results from data. Also we look into the rate of cosmogenic events providing WIMP like candidates for the blind analysis [81] described in Section 4.3.

3.5.2.1 Veto Efficiency

For the veto-efficiency, a simulated livetime of approximately 48.7 years was examined. As described, the optical processes were turned on in a second step of the simulation where only those particles that reached the LSV in the first stage were considered. Of the total events, 1388 events were found where one or more particles reached the sensitive volume.

None of these events are considered as background, as they deposit a considerable amount of energy in the LSV (≥ 100 MeV) and this would provide sufficient light to veto the events. See Figure 3.9 for the distribution of these 1388 particles.

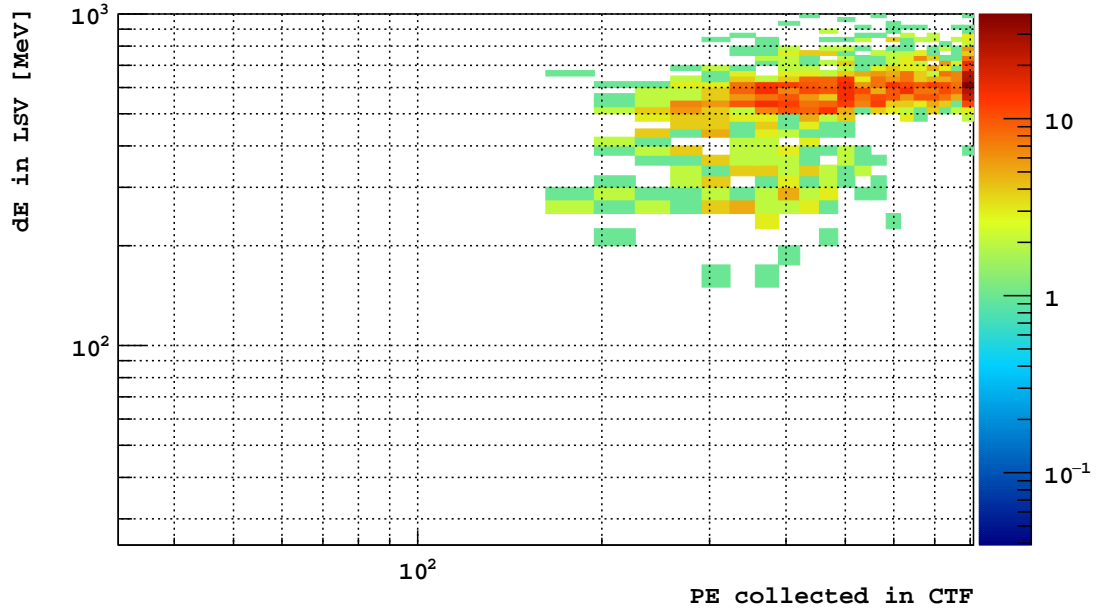


Figure 3.9: Two dimensional distribution of events that had particles reaching the TPC. Dangerous events would be near the origin of the plot, but none were found.

Of these 1388 events, there were only 16 events (see Figure 3.13) where neutrons were among the set of particles, with only 7 events where the neutron was one of at most two particles reaching the sensitive volume. A single event was found in the entire simulated livetime where a single neutron reached the TPC, and to re-iterate, it was not considered potential background because it failed the simulated veto cuts. We found that the light yield in the water tank did not quite match what was observed in the 70 day open dataset (see Figure 3.12). Most of the cosmogenic events registered more than 600 photo-electrons in the WCV. This is somewhat expected since the reflectivity of Tyvek was set to a much lower value (80%) in the simulation. In order to check the validity of the simulation further, the reflectivity was set to the measured value of 99% and the threshold to terminate counting of photoelectrons in the simulation was increased from 800 (see Figure 3.10) to 1600 (see

Figure 3.11). A simple estimate tells us that over the course of three reflections, about 50% of the light in an event would be lost with a reflectivity of 80% and hence we should expect a considerable increase in the photo-electrons generated in the WCV. Of course this is at the expense of much more computational time as each photon has to be tracked for a longer time and has a higher survival probability at each reflection. This required a significant reduction in simulated livetime (14 years) considering the limited computational resources. After these adjustments were made, much better agreement in the light yield of the WCV was found between data and simulation. This simulation, with a more accurate representation of light yield, produced 8 events where neutrons were among the set of particles reaching the sensitive volume (see Figure 3.14) and none of these passed the veto cuts.

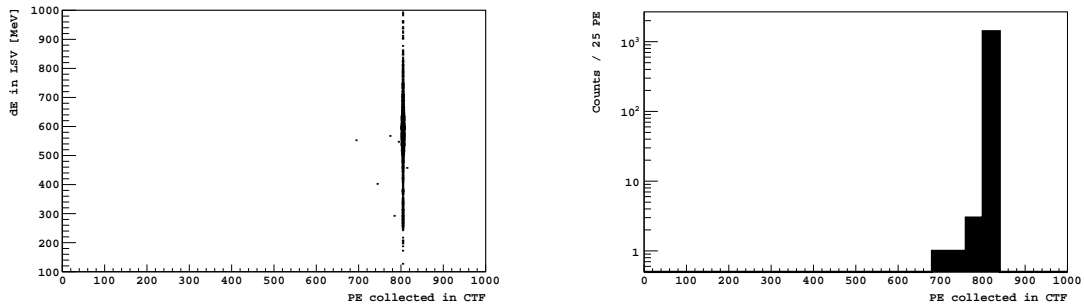


Figure 3.10: (left) 2D Distribution of all particles that reached the sensitive volume; (right) Projection of the distribution in PE collected in WCV. It is clear that all the muon events register more than 700 PE as seen in data, but the simulation cuts off at 800 PE, hence the saturation

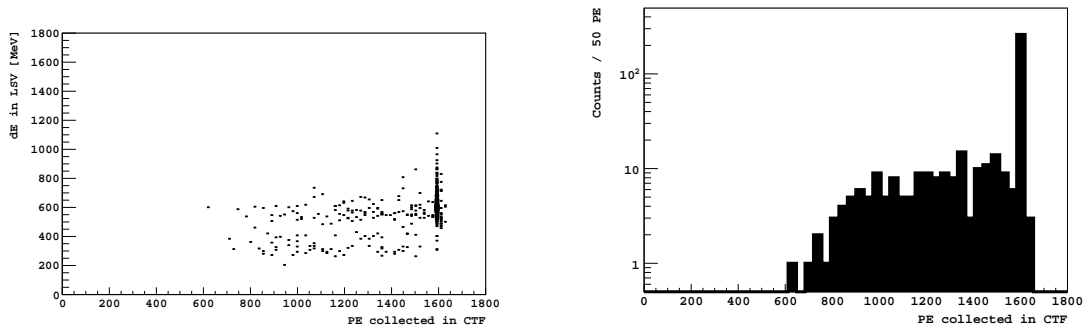


Figure 3.11: (left) 2D Distribution of all particles that reached the sensitive volume; (right) Projection of the distribution in PE collected in WCV. Simulation cut off at 1600 PE now. Note the lifetime is now reduced to 14 years.

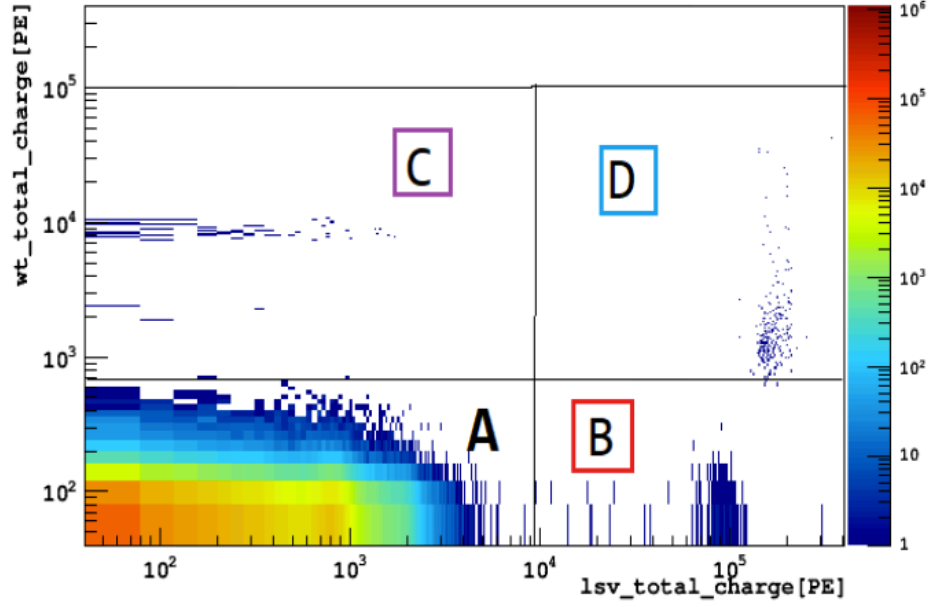


Figure 3.12: Distribution of events in 70 day UAr data. The top right section (D) corresponds to muon events which result in more than 700 PE being collected in the WCV. Regions (B) and (C) correspond to noisy LSV and WCV events respectively. Region (A) corresponds to normal events. The colour scale represents the event count. Figure from H. Qian.

An upper limit (90% Frequentist confidence level) was set on the probability for the veto cuts to miss cosmogenic events that had particles reaching the sensitive volume at

$$< \frac{2.3}{1388} = 0.0017. \quad (3.12)$$

This number was then appropriately normalized for the livetime, and taking a very conservative limit by including all of the 7 events that had up to two particles (one being a neutron) as follows :

$$\frac{7}{48.7\text{yr}} \times \frac{532\text{d}}{365\text{d/yr}} \times \frac{< 2.3}{1388} \leq 3.5 \times 10^{-4} \quad (3.13)$$

The final prediction for cosmogenic neutron background after all cuts is then taken to be $< 3.5 \times 10^{-4}$ events for the 540 day WIMP search (See Section 4.3.5).

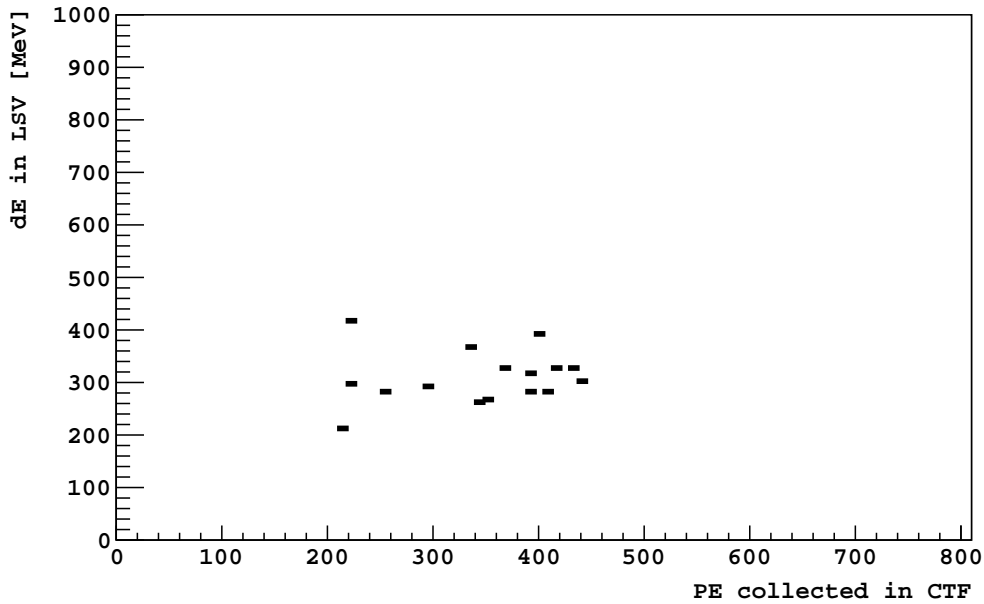


Figure 3.13: Distribution of the 16 events that had one or more neutrons reaching the sensitive volume in simulated livetime of ~ 49 years with a photo-electron counting cut-off at 800

3.5.2.2 Expected Background for a Blind Analysis

In order to assess the expected background for a blind-analysis, one must answer the question “How many events could be potentially WIMP-like if one is denied access to information from the veto detectors?”. To evaluate this background, one must consider all the prepared simulated events at the ceiling of Hall-C. This is because, the conservative removal of muon events with the high-energy long-track length in water inherently uses information from one of the veto detectors, *i.e.*, the WCV. When this high energy-high track length cut is lifted from the simulation procedure, optical processes are no longer required, but the average computational time per event required for simulation is higher than the case where this cut is imposed. Hence, a slightly reduced lifetime of about 33.36 years was produced. The full range of TPC cuts was not applied as a complete description of the optics in the LAr is not present in the current simulation. Instead a coarser version of the TPC cuts was employed. Namely, allowing the entry of a single neutron which has a single elastic scatter

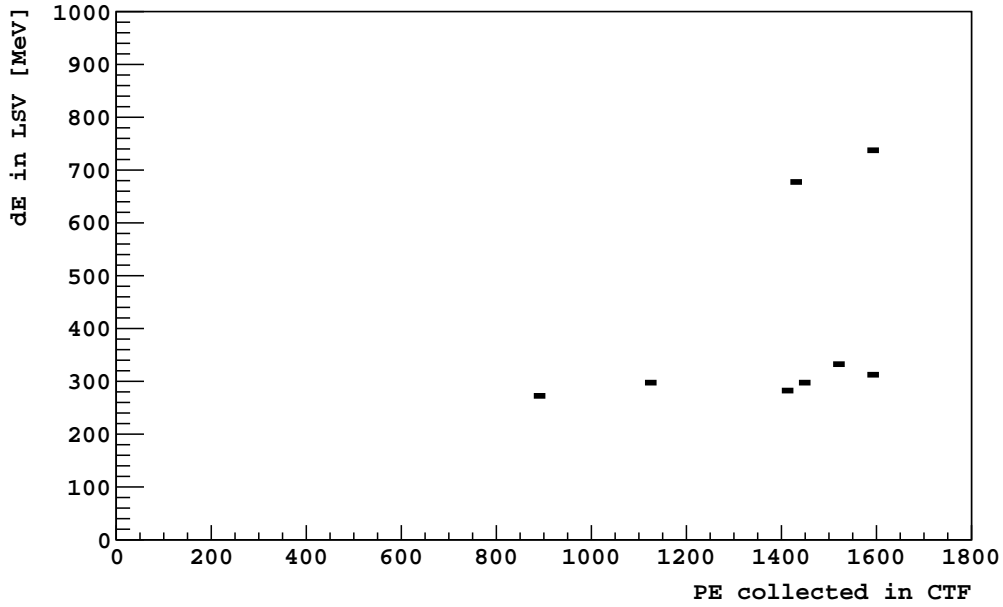


Figure 3.14: Distribution of the 8 events that had one or more neutrons reaching the sensitive volume in the simulated livetime of ~ 14 years with a photo-electron counting cut-off at 1600. It can be seen that all of the events deposited more than 800 PE in the WCV and hence the cut in data, set at 400 PE is safe.

inside the sensitive volume with a raw energy deposition (dE_{TPC}) in a conservative range of the expected WIMP signal *i.e.*, $0 < dE_{TPC} \leq 0.5$ MeV. It was found that the number of neutrons potentially passing these approximate TPC cuts is 1.738 per year. When the cuts are relaxed to permit the entry of up to 2 particles (at least one being a neutron) we find a rate of 2.787 per year. In the veto prompt tag dataset of 532 days, 3 cosmogenic events were found [81]. In our previous two analyses with a combined livetime of 118 days, 1 such cosmogenic neutron event was found [35, 51]. Therefore we find that the simulation predicts reasonably well the number of neutrons expected to give WIMP-like signals if the veto information was abandoned. See Section 4.3.5 for a perspective of where these neutrons fall with respect to the WIMP search box.

Chapter 4

WIMP Searches with DS-50

This chapter outlines the five main results of the DS-50 dark matter searches. The most recent involves low-mass WIMPs and sub-GeV DM particle searches and forms an important baseline for Chapter 6 which is centered around the search for axions with DS-50.

4.1 Atmospheric Argon (AAr) 50 Day Search

This section summarizes the results of [35] which reported the first WIMP search results from the DarkSide collaboration. This dark matter search was performed with an atmospheric argon (AAr) target acquiring data between November 2013 and May 2014. Some basic cuts were employed to remove runs where the detectors may not have been running or where the DAQ showed signs of instability. Further data quality cuts were applied to accept events where all 38 TPC PMTs were alive and had an adequately recognized baseline for each channel. Pileup events were rejected by selecting only the events with a pulse start time of at least $1.35 \mu\text{s}$ after the start of the previous event. Events were also rejected if the DAQ seemed to be inactive for more than 1 second which indicated that the DAQ had stalled. A non-blind analysis was performed on the 53.4 live days of collected WIMP search data. All events in the TPC were discarded where correlated activities in the LSV and

WCV were found. Events containing exactly two pulses, S1 and S2 were selected for further analysis since these could potentially be WIMPs. In addition, events with a valid S3 (echo of an S2 [35]) were also selected.

Each of the events was required to have a start time for the S1 pulse in the expected trigger position in the TPC DAQ window. Moreover, the S1 must not have saturated any of the PMTs. The requirement on the second pulse (presumably the S2) was that it should have had an f_{90} lower than 0.2 to exclude events with fake S2 signals generated by re-triggering on an S1 pulse. The S2 signal was also required to be greater than 30 PE. A fiducial cut in the z direction was employed by requiring that the drift time of an event was between 40 and 334.5 μs to reject background events arising from the top and bottom surfaces of the TPC. Finally, only those events which had an S1 in the range expected by a WIMP-nucleon recoil between 80 and 460 PE were selected. The total exposure remaining after all cuts was (1423 ± 67) kg-days. The distribution of events in the S1- f_{90} plane is shown in Figure 4.1 (left). The distribution was studied by dividing events into 5 PE wide bins in S1, and fits were performed using an analytic model [115] to characterize the f_{90} distributions. Nuclear recoil acceptance curves were derived from the SCENE f_{90} median values. The details for this are in [35]. The dark matter search box in Figure 4.1 (right) was obtained by intersecting the 90% nuclear recoil acceptance curve with the electron recoil leakage curve corresponding to 0.01 events per bin (5 PE width). This keeps the expected leakage of ^{39}Ar events to <0.1 events and resulted in 4 events which passed all TPC cuts, with an f_{90} consistent with that of a nuclear recoil. However each of these events had energy depositions in the LSV above the defined veto cut threshold and were therefore rejected as WIMP candidates.

The dark matter limit as shown in Figure 4.1 was derived using a standard thermal WIMP halo model with $v_{\text{escape}} = 544$ km/s, $v_0 = 220$ km/s, $v_{\text{Earth}} = 232$ km/s and $\rho = 0.3$ GeV/($c^2 \text{ cm}^3$). Since no WIMP like candidates were observed, a 90% CL exclusion curve (which corresponds to observing 2.3 events for spin-independent interactions), is drawn.

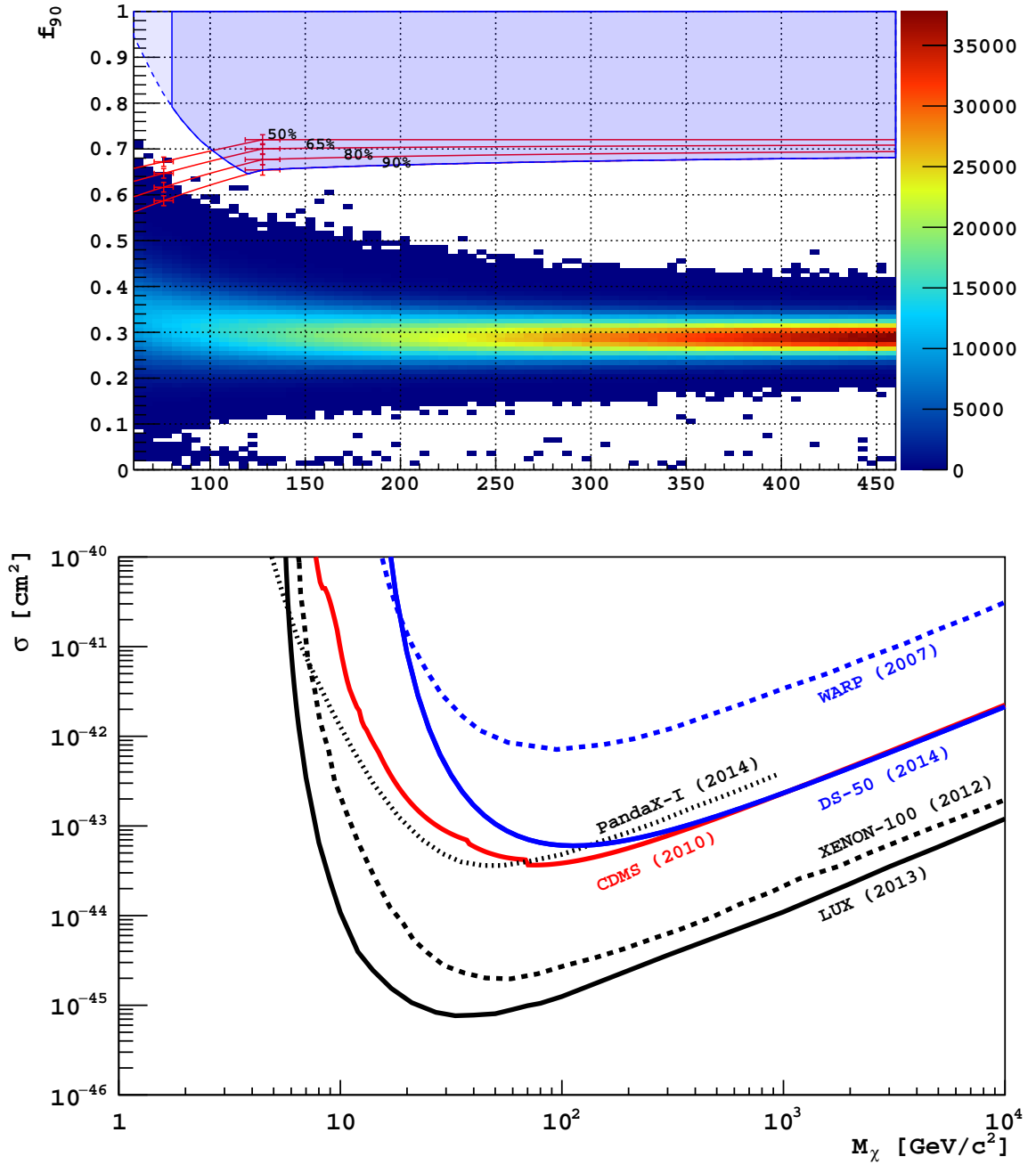


Figure 4.1: (top) Distribution of events in the scatter plot of S1 vs. f_{90} after all cuts. The dark matter search box is represented by the shaded blue area with the solid blue outline. The percentages label the f_{90} acceptance contours for the nuclear recoils drawn connecting points determining from the corresponding SCENE [116, 117] measurements. The colour scale represents event count. (bottom) Spin-independent WIMP-nucleon cross section 90% CL exclusion curves for DS-50 (solid blue) in comparison to other experimental results. Figure taken from [35].

4.2 Underground Argon (UAr) 70 Day Search

This section summarizes the results of [51] which reported the first use of argon from underground sources for a WIMP search, thereby paving the way for scalable LAr technology for WIMP searches. Data for this analysis were collected between April 8, 2015 and July 31, 2015 corresponding to 70.9 live-days of running. The total exposure for this analysis corresponded to 2616 ± 43 kg days of data.

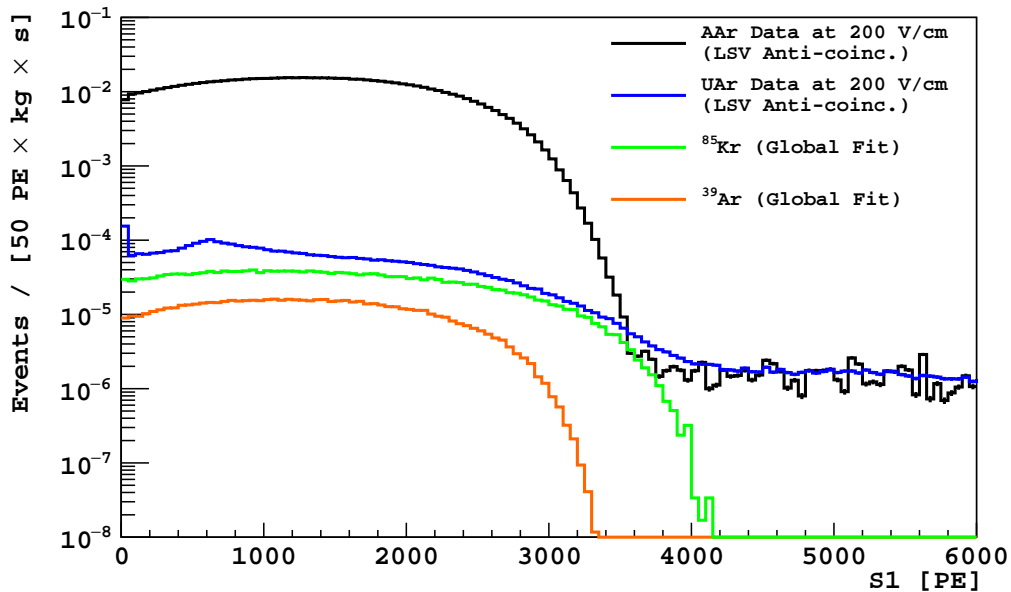


Figure 4.2: Live-time normalized S1 pulse integral spectra from single-scatter events in AAr (black) and UAr (blue) taken with 200 V/cm drift field. Also shown are the ^{85}Kr (green) and ^{39}Ar (orange) levels as inferred from a MC fit. The peak in the lowest bin of the UAr spectrum is due to ^{37}Ar electron capture. The peak at ~ 600 is due to γ -ray Compton backscattering. Figure taken from [51].

Fig. 4.2 compares the UAr and AAr data of the S1 pulse integral spectrum. A z -cut (residual mass of ~ 34 kg) was applied to remove γ ray events from the anode and cathode windows. Events identified as multiple scatters, or coincident with a prompt signal in the LSV were also removed. To compare the ER background from UAr with that from AAr, G4DS was used. The simulation accounts for material properties, optics, and readout noise,

and includes a model for LAr scintillation and recombination. The MC is tuned to agree with the high statistics ^{39}Ar data taken with AAr

The fitted ^{39}Ar and ^{85}Kr activities present in the UAr are shown in Fig. 4.2. The uncertainties in the fitted activities are dominated by systematic uncertainties from varying fit conditions. The ^{39}Ar activity of the UAr was derived from the spectral fit to be $(0.73 \pm 0.11)\text{mBq/kg}$ and corresponds to a reduction by a factor of $(1.4 \pm 0.2) \times 10^3$ relative to AAr.

An independent estimate of the ^{85}Kr decay rate in UAr is obtained by identifying β - γ coincidences from the 0.43% decay branch to metastable ^{85m}Rb with mean lifetime $1.46 \mu\text{s}$. This method gives a decay rate of ^{85}Kr via ^{85m}Rb of (33.1 ± 0.9) events per day in agreement with the value (35.3 ± 2.2) events per day obtained from the known branching ratio and the spectral fit result. The ^{85}Kr activity was measured to be $(2.05 \pm 0.13) \text{mBq/kg}$. The presence of ^{85}Kr in UAr was unexpected and it was not attempted to remove krypton from the UAr, although cryogenic distillation would likely do this very effectively.

The nuclear recoil energy scale is determined from the S1 signal using the photoelectron yield of nuclear recoils relative to ^{83m}Kr measured in the SCENE experiment [116, 117] and the zero-field photoelectron yield for ^{83m}Kr measured in DarkSide-50. An *in-situ* calibration with an $^{241}\text{AmBe}$ source was also performed, providing a check of the f_{90} medians obtained for NRs in DarkSide-50 with those scaled from SCENE.

Cuts are typically employed in all DarkSide analyses and are moreover used in Chapter 5 and Chapter 6. The purpose of these cuts is to ensure that the detector was operating in stable conditions during the period an event was recorded.

4.2.1 Basic Quality Cuts

The Basic Quality Cuts are :

- Channel Cut.

Required to affirm that all 38 TPC channels are operating.

- Baseline Cut.

Required to affirm that the baseline is successfully calculated in all of the 38 channels.

- Veto present Cut.

Required to affirm that the veto data be present and a one-to-one correspondence was successfully found between a TPC event and a Veto event.

- Livetime Cut.

Required to affirm that the start time of acquisition window was at least 1.35 ms after the acquisition of the previous event has ended.

4.2.2 TPC Cuts

WIMPs are expected to create single scatter NR events uniformly distributed in the active LAr. Hence, the following TPC cuts were implemented and only those events passing all of these cuts were accepted. :

- 2-pulses Cut.

Required to affirm that the event posses two pulses, or 3 pulses if the third pulse is consistent with an echo (S3) of the second pulse (S2). An S3 is identified as a pulse with an S2-like f_{90} which occurs exactly $373 \mu s$ after the original S2 pulse. An S3 is induced by an extremely intense S2 signal which could induce photoelectric emission from the cathode window. The purpose of this cut is to accept WIMP-like events which are expected to be single-scatter in the LAr.

- Trigger Time Cut.

Required to affirm that the start time of the pulse (typically S1) was in coincidence with the expected trigger time ($-6.1 \mu s < t < -6.0 \mu s$)

- 95% S1MF Cut.

Required to affirm that the S1 maximum fraction (S1MF) was below the pre-defined threshold. S1MF is defined as the fraction of the total S1 light in the dominant channel. This cut was designed to reject events where Compton scattering of γ -rays in the fused silica windows produce ERs that generate Cherenkov radiation, in coincidence with Compton scattering in the LAr. These events could potentially look like NRs since the Cherenkov signal has an $f_{90} \sim 1$.

- S2 f_{90} Cut.

Required to affirm that the second pulse was S2-like ($f_{90} < 0.2$).

- Minimum S2 Cut.

Required to affirm that the second pulse (typically S2) after applying radial corrections was greater than 100 PE.

- Tdrift Cut.

Required to affirm that the drift time of an event was less than 334.6 μ s, but more than 40 μ s.

4.2.3 Veto Cuts

- Veto Prompt Cut.

Required to reject an event if the signal in the prompt window was greater than 1 PE. The prompt window runs from 50 ns before the TPC trigger time to 250 ns after the trigger. This cut was designed to identify events where either a thermalization of a neutron occurred in the LSV or a γ ray (from radioactive decay or inelastic neutron scattering) interacted in the LSV.

- Delayed Cut.

Required to reject an event if the charge computed by the slider window in the delayed coincidence region was greater than 6 PE (3 PE for run numbers < 12638). This cut

was designed to identify neutrons which potentially interacted in the LAr and primarily get captured on the ^{10}B present in the LSV cocktail.

- Pre-prompt Cut.

Required to reject an event if the charge computed by the 500 ns slider window was more than 3 PE. This region comprises the start of the veto acquisition window to the prompt time. This cut was designed to reject events where neutrons scatter in the LSV before entering the TPC and interacting in the LAr.

- Muon Cut.

Required to reject an event if the total charge within the LSV veto acquisition window was more than 2000 PE or if the total charge acquired in the water tank was more than 400 PE, typical of a cosmic muon traversing either detector. This cut was designed to tackle NR events in the LAr which are the result of cosmic muon interactions (see Section 3.5 for more details).

- Cosmogenic Cut.

Required to reject an event for a 2 s duration after the previous muon event (an event which activated the muon cut). This cut was designed to reject events where muon interaction could potentially activate nuclei which subsequently decay via delayed neutron emission.

4.2.4 Results

An accurate prediction of the ER background is one of the most challenging aspects of WIMP analysis. In the 50 day AAr analysis, a leakage curve was developed by requiring no more than 0.05 events per 5 PE bins and subsequently fitting Hinkley's model [118] to the data. For this 70 day analysis which used a UAr target, the same model did not provide reasonable agreement with data. A more involved procedure was developed [51, 57, 119] and iterated until for all f_{90} profiles (corresponding to different S1 bins), obtaining a count

of 0.01 events per 5 PE slice. The leakage curve allowed a total of less than 0.1 single-scatter ER background events in the WIMP search box. For the NR acceptance curve, a similar procedure was applied. The analytic model was fit to the AmBe data, with two free parameters. The fitted values of the parameters are cross-checked with the SCENE results for the same drift field, and a consistent match was found. The results are shown in Figure 4.3.

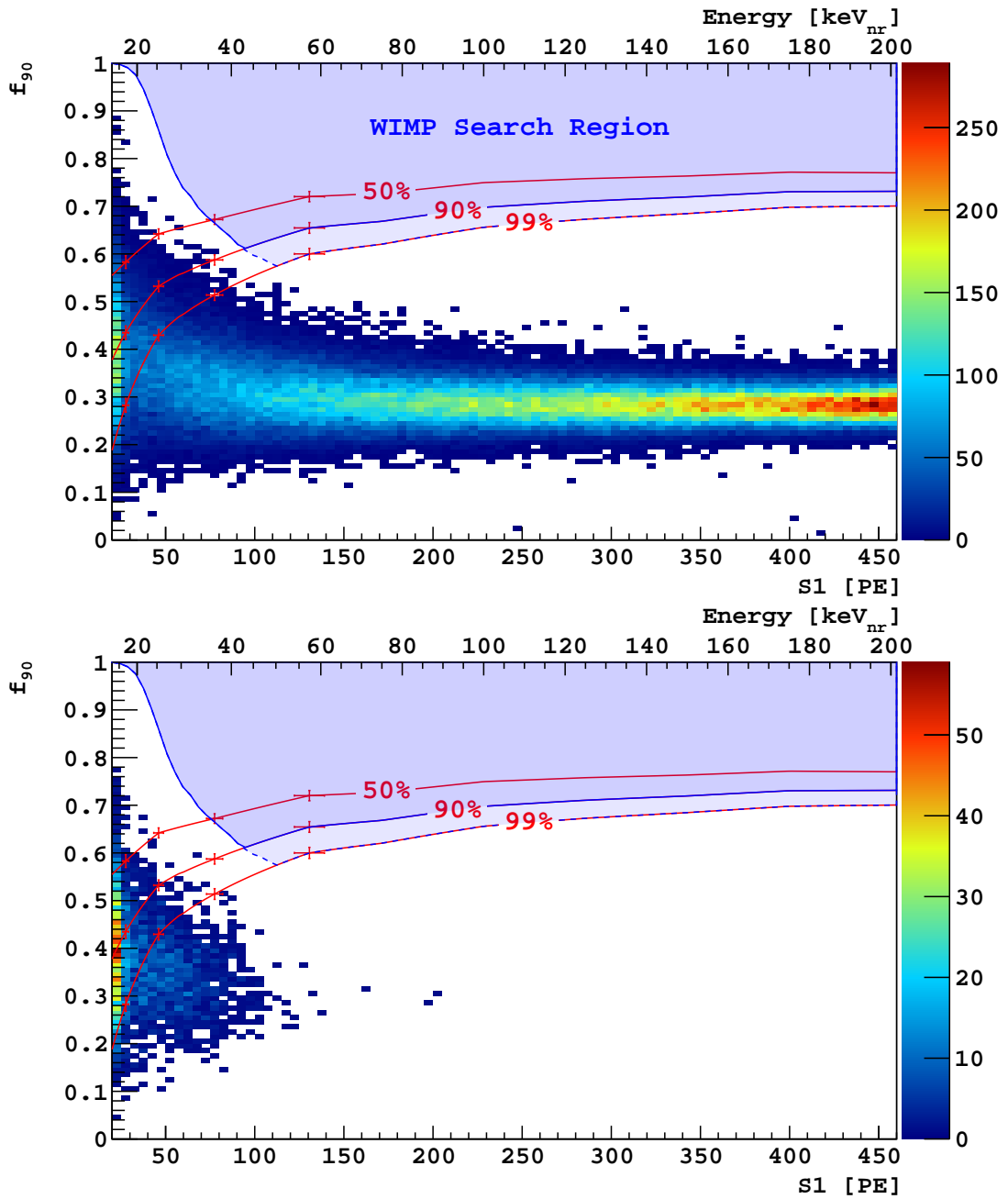


Figure 4.3: (top) Distribution of events in the f_{90} vs S1 plane surviving all cuts in the energy region of interest. The WIMP search region is depicted by the shaded blue outline. The red points are derived from SCENE measurements of Nuclear Recoil acceptance. It is worth comparing the z-scale to Figure 4.1 to illustrate the reduction in background offered by UAr. (bottom) The distribution of events in the same S1 vs f_{90} plane which survive all cuts and additional cuts on radial position and S2/S1. The colour scale represents the number of events in both plots. Figure taken from [51].

The total exposure for this WIMP search after all cuts was (2616 ± 43) kg day. The null results from the first UAr campaign are shown in Figure 4.3. A 90% CL exclusion curve corresponding to the observation of 2.3 events assuming a spin-independent interaction was developed. The WIMP halo parameters are the same as the ones used for the previous analysis. The exclusion curve is shown in Figure 4.4. If the results from the previous analysis are combined, an upper limit on the WIMP-nucleon cross section is found to be most sensitive for a WIMP of mass $1 \text{ TeV}/c^2$ and excludes cross sections above $8.6 \times 10^{-44} \text{ cm}^2$.

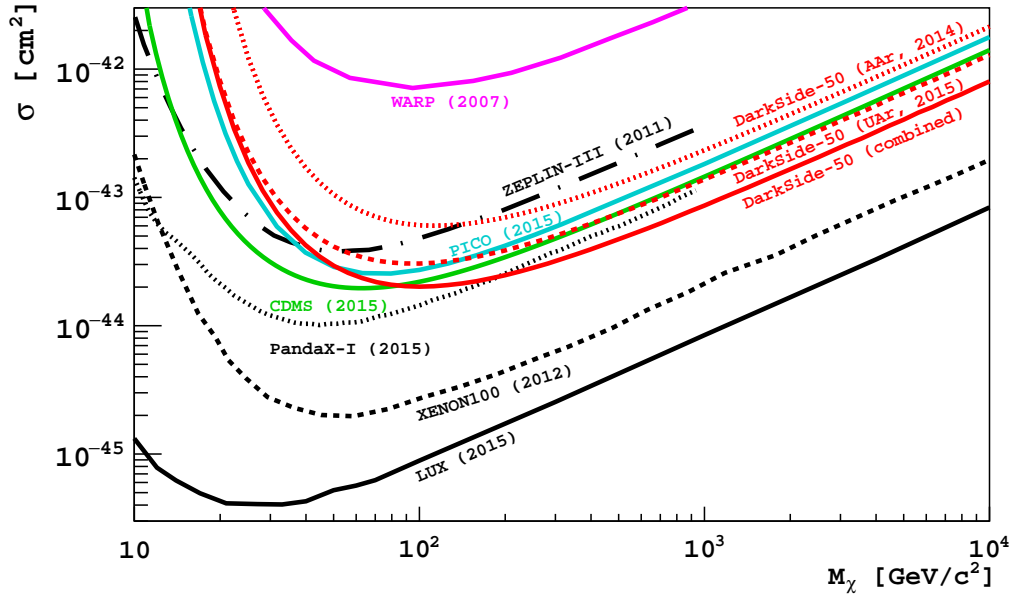


Figure 4.4: Spin-independent WIMP-nucleon cross section 90% C.L. exclusion plots for the DS-50 AAr (dotted red) and UAr campaigns (dashed red), and combination (using [120]) of the UAr and AAr campaigns (solid red). Also shown are results from LUX [37](solid black), XENON100 [121](dashed black), PandaX-I [122] (dotted black), CDMS [123] (solid green), PICO [124] (solid cyan), ZEPLIN-III [125] (dash dotted black) and WARP [126] (magenta). Figure taken from [51].

4.3 UAr 500 Day Blind Analysis

This section summarizes the results of [81] which reports the first WIMP search via a blind analysis performed by the DarkSide collaboration.

4.3.1 Data Set

The analyzed data consist of 532.4 live days of UAr data collected from August 2, 2015 to October 4, 2017. The data used in previous analyses is not included in this set. Blinded data were checked on a run-by-run basis for both hardware and software issues. After removing runs with issues such as abnormal noise or oscillations in veto channels, the livetime was reduced to 545.6 days. After employing basic quality cuts and veto cuts to remove cosmic ray activation, the final livetime was 532.4 live-days. The total exposure reported was (16660 ± 270) kg day.

4.3.2 Blinding Scheme

Candidate selection and background rejection were designed by the analyzers without the knowledge of the number or properties of the events in the final search region. A “blinding module” was imposed in the analysis pipeline (SLAD - see [57] for details about the SLAD framework). Blinded events appeared in the output files, but with all the TPC data except the event ID, timestamps and livetime associated with these events set to -1. Apart from the events outside the blinding box, open data from the previous two analyses was available to the analyzers to tune background rejection. (See [81] for more details on the scheme.) During the course of the analysis, a few sections of the blinded data, outside of the WIMP search region, were unblinded to test background predictions.

4.3.3 Cuts

The cuts employed in this analysis were primarily the same as the ones employed in the 70 day analysis other than the following updates and/or additions.

- Livetime Cut.

This cut was updated from the previous analyses. Events were selected which had a

livetime of greater than $400 \mu\text{s}$. The cut was designed to tackle situations where a scatter in the LAr occurred during the inhibit window following a prior trigger and the associated S2 signal triggers the detector. A coincident pulse in the corresponding acquisition window could then potentially create a fake two-pulse event. If A scattering in the LAr occurred during the inhibit window, as associated S2 could not arrive any later than $\sim 376 \mu\text{s}$ after the end of the inhibit window.

- Minimum corrected S2/S1.

This cut was developed for this analysis. Only those events were selected which had a second pulse compatible with an S2 signal by requiring that the ratio of S2 to S1 was more than a pre-defined S1 dependent quantity. This cut was designed to ensure that the S2 pulse was compatible with the one expected from a WIMP-like event.

- Cosmogenic Cut.

This was updated from the previous analysis. The duration for which events were discarded after a previous event failed the muon cut was decreased from 2 s to 0.6 s.

- Uncorrected S2.

This cut was an updated version of the minimum S2 cut in the previous analysis. Events were selected if they had an uncorrected s2 of more than 200 PE. This update was made primarily to decouple the cut from the xy position reconstruction algorithm.

- Radial Cut.

This cut was new. Events were selected which had a reconstructed radius less than a predefined (vertical position dependent) threshold.

- S1 tail Cut.

This cut was new. Events were rejected which had S1 tails compatible with α events. See [87] for details.

- S2 pulse shape Cut.

This cut was new. It was developed to ensure that the second pulse was indeed an

S2 by affirming that the early shape of the pulse was compatible to a true S2 and not one of a pileup background event. See [127] for more details.

- $S1_{prompt}$ max fraction Cut.

This cut was an updated version of the S1 max frac cut in the previous analysis. Events, which had high concentration of the prompt S1 light in a single channel, were rejected. The cut was updated to consider the light distribution of the the prompt part of the S1 signal, rather than that of the total S1.

- Negative log-likelihood of S1 light distribution.

This cut was new. This cut selected events which had S1 light distributions with low negative log-likelihood values, subject to their reconstructed positions. See [128] for details.

4.3.4 Background Modeling

The purpose of the blind analysis was to design criteria which reject background to a pre-determined level without prior inspection of events in the final WIMP search box. (The search box must also be designed as part of the analysis procedure). An expected background of 0.1 events in the WIMP search box was chosen as the permissible amount of background, which would have less than 10% (Poisson) probability of generating an observation of >1 background event in the box.

Various schemes to model different types of backgrounds were employed. In particular, a class of backgrounds in which ER events had coincident Cherenkov radiation in the PTFE, were the most challenging to model and design cuts for their removal [88]. Details on estimating the radiogenic neutron background can be found in [129], whereas details on cosmogenic backgrounds can be found in Chapter 3 of this dissertation. A thorough investigation of surface background events was done in [87,127]. Neutron candidates in the veto prompt tag sample can be seen in Figure 4.6.

4.3.5 Unblinding and Results

Unblinding the data involved changing the access permissions of the SLAD data, and then running the analysis code subsequently applying all cuts. Figure 4.5 shows f_{90} vs. S1 after applying all analysis cuts. No events were observed in the pre-defined WIMP search region. A limit on the spin-independent WIMP-nucleon scattering (Figure 4.7) is derived assuming the standard isothermal WIMP halo model with parameters already defined in the previous analyses results. The background and signal-free result is consistent with up to 2.3 WIMP induced scatters (90% CL) which sets an upper limit on the scattering cross section at $1.14 \times 10^{-44} \text{ cm}^2$ for $100 \text{ GeV}/c^2$ WIMP particles.

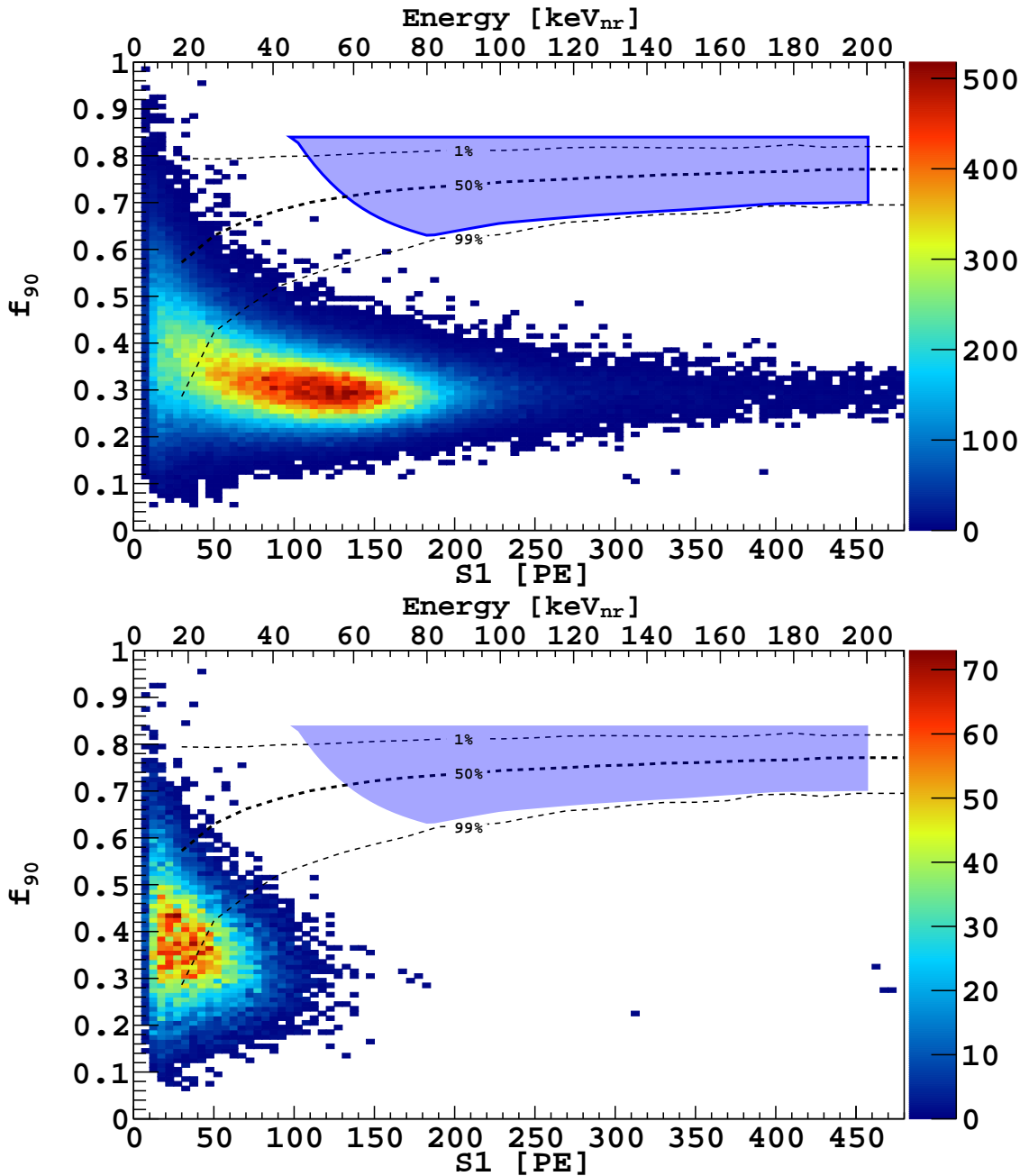


Figure 4.5: (top) Observed events in the f_{90} vs S1 plane surviving all cuts on the energy region of interest. The solid blue outline indicated the WIMP search region. The different f_{90} acceptance contours for nuclear recoils as derived from fits to $^{241}\text{AmBe}$ calibration data are depicted by dashed lines. (bottom) Distribution of events in the f_{90} vs S1 plane that survive all analysis cuts and that in addition survive two more unused cuts in this analysis. They require S2/S1 lower than the median value for nuclear recoils and also a reconstructed radius of less than 10 cm from the centre of the TPC. An even greater separation between the events surviving the selection and the previously defined WIMP search region is obtained. The colour scale represents the count of events in either plot. Figure taken from [81].

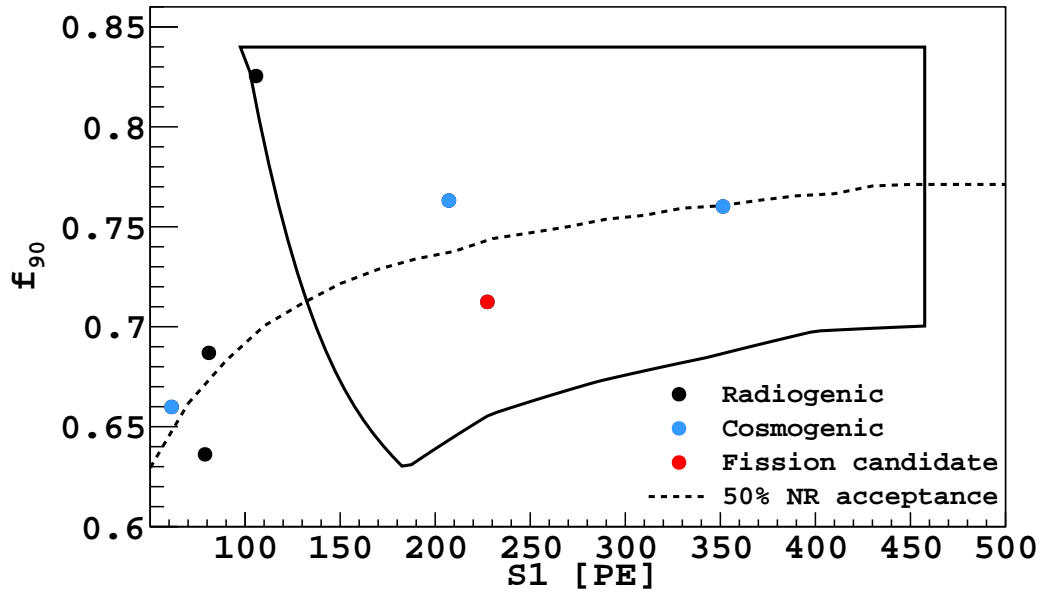


Figure 4.6: Neutron candidates in the Veto Prompt Tag sample. The closed curve is the final WIMP search box. The dashed curve is the 50% nuclear recoil contour around which neutron induced events should be distributed. The observation of the three cosmogenic neutron candidates are compatible with the prediction of the simulation study performed in Section 3.4.4.2. Figure taken from [81].

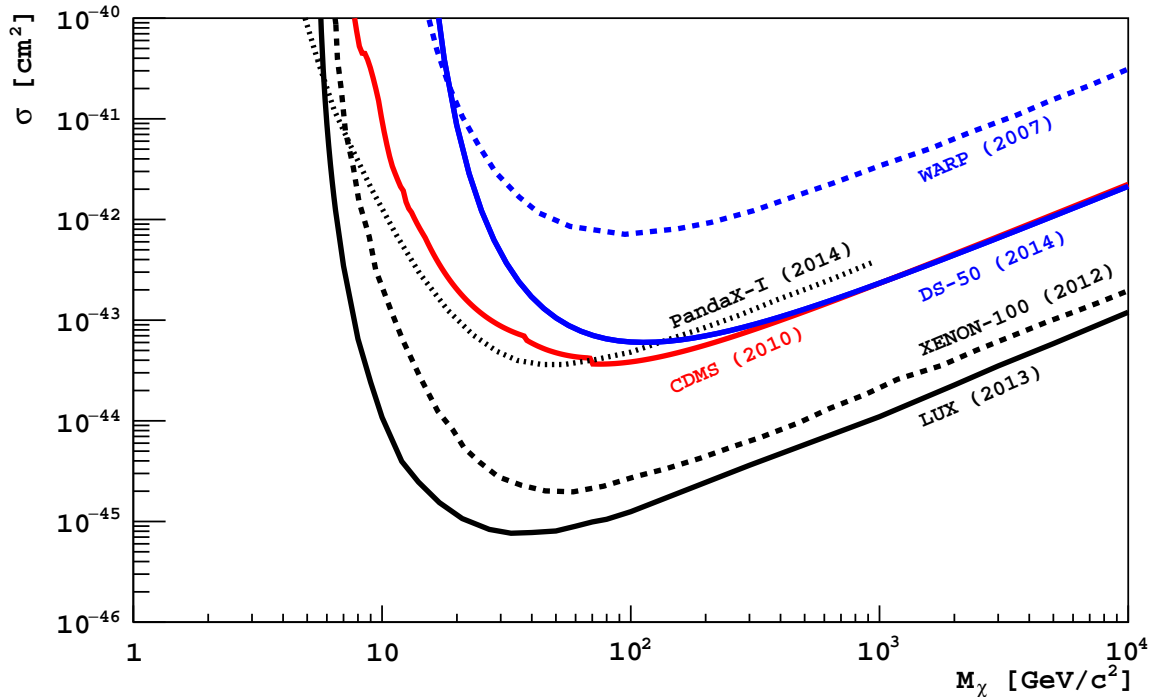


Figure 4.7: Spin-independent DM-nucleon cross section 90% C.L. exclusion limits from the analysis detailed in the paper [81], compared to the previous DarkSide result [51] and selected results from other experiments [32, 45, 126, 130, 131]. Figure taken from [81].

4.4 Low Mass WIMP Search

This section summarizes the results of [132] which led to the most sensitive limit on WIMP-nucleon scattering cross section for low-mass WIMPs ($5 \text{ GeV}/c^2 < \text{mass} < 1.8 \text{ GeV}/c^2$).

4.4.1 S2-Ionization Signals

Unlike previous analyses which required both an S1 and an S2 pulse, this analysis is able to operate with a much lower energy threshold by accepting events with only an S2 pulse. The efficiency of the pulse finding algorithm is virtually 100% for S2 signals greater than 30 PE. A low-mass WIMP is expected to produce a very low energy recoil in the LAr

which would produce an undetectable S1 signal, but an S2 signal which could be measured. Since there is no S1 associated with many of these events analyzed, there is no possibility to fiducialize in the z direction because of the absence of a measured drift time. The standard xy finding algorithm also fails at such low recoil energies due low PE statistics. Hence the xy position of each event is assigned to the centre of the PMT receiving the largest number of S2 PEs. Further, events are only accepted if the largest S2 signal is recorded in any one of the seven central top PMTs. This gives a means to fiducialize the volume in the xy direction, but with larger systematic uncertainties than would be present in the S1+S2 analysis.

4.4.2 Ionization Yield

The S2 photoelectron yield per extracted ionization electron, η , is determined by studying single-electron events obtained during a period of time in which the argon purification getter was turned off. The runs during this period have enhanced single-electron event rates due to electrons getting trapped on impurities and being released at a later time. A radial variation in electroluminescence yield is observed and hence a correction is applied to the S2 photoelectron yield for events that occur under the six PMTs, other than the central one. In situ calibration data from $^{241}\text{Am}^{13}\text{C}$ and $^{241}\text{AmBe}$ neutron sources [133] and neutron-beam scattering data from the SCENE [116, 117] and ARIS [134] experiments are used to compute the ionization yield (Q_y) from nuclear recoils. The final $^{241}\text{Am}^{13}\text{C}$ and $^{241}\text{AmBe}$ spectra are fit simultaneously to recoil energy distributions from G4DS using the Bezrukov model [135] to convert nuclear recoil energy to ionization. The model has two free parameters that relate to a combination of the energy quenching and the ionization to excitation ratio and the recombination rate of the ionization pairs. For the $^{241}\text{Am}^{13}\text{C}$ data, these two parameters are sufficient and the fit goes to the analysis threshold of four electrons. In the case of $^{241}\text{AmBe}$ calibration data, events are only accepted if they were found to be in coincidence with the detection of the 4.4 MeV γ in the veto. This requirement effectively

singles out a pure neutron recoil sample. The fit for this $^{241}\text{AmBe}$ data then, also includes a term for the acceptance of the coincidence requirement and a strong correlation is seen between the uncertainties on the the ionization response and the acceptance-loss model. In order to bypass this correlation, the fit to the $^{241}\text{AmBe}$ data has a threshold of $50 e^-$ above which the fraction of S2-only events is negligible. The ionization yield as a function of recoil energy is shown in Figure 4.8.

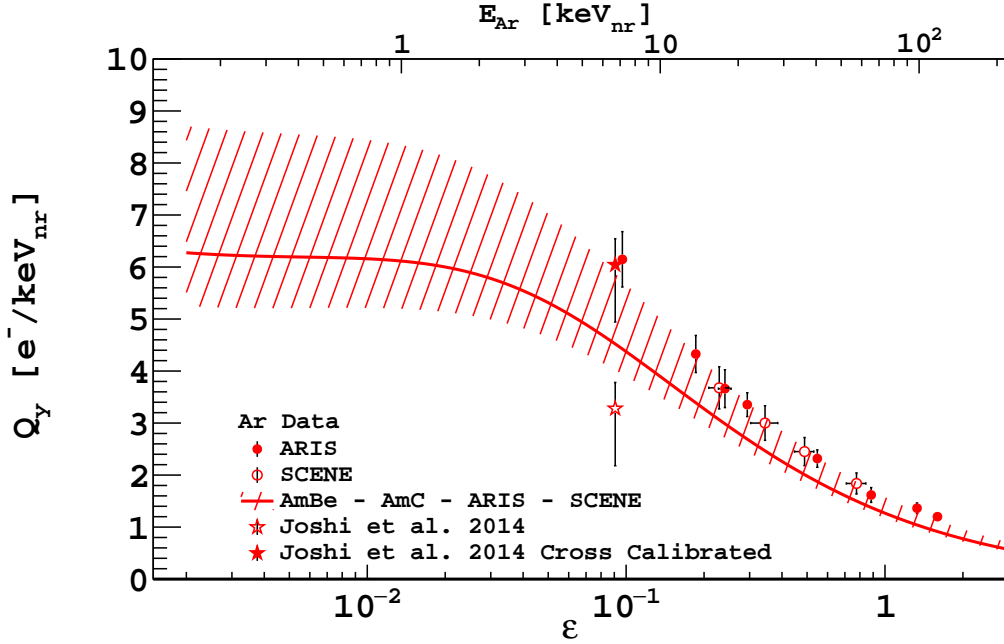


Figure 4.8: The measured ionization yield Q_y for nuclear recoils in LAr as a function of the reduced the nuclear recoil energy in liquid argon. Also shown is the Bezrukov model fit to the $^{241}\text{AmBe}$ and $^{241}\text{Am}^{13}\text{C}$ data and data from [136]. The shaded band depicts the uncertainty on the ionization yield derived from the model. (Refer to [132] (source of Figure) for details).

4.4.3 Results

Upper limits on the WIMP-nucleon scattering cross section are extracted from the observed N_{e^-} spectrum using a binned profile likelihood method [137]. Two signal regions are defined. The first of which has an analysis threshold of 4 drifted electrons, which is determined approximately by the tail of the trapped electron background spectrum [132].

The second region has a threshold of 7 drifted electrons, where the background is described reasonably well by G4DS. The first region has sensitivity to the entire range of WIMP masses that were explored, however the data are contaminated by a component which is not included in the profile likelihood model, which leads to weaker bounds on the cross section. The second signal region has limited sensitivity to WIMP masses below $3.5 \text{ GeV}/c^2$ but the fit performed in this region is able to more tightly constrain the cross section at higher masses due to better description of the background model. For a given WIMP mass and fluctuation model, the limits on the cross section are calculated using both regions and the more stringent one is quoted. The 90% CL exclusion curves for the binomial fluctuation model and the model with zero quenching fluctuation are shown in Fig 4.9. For masses above $1.8 \text{ GeV}/c^2$ the exclusions limits are nearly insensitive to the choice of the fluctuation model. The background and exclusion curve is shown in Figure 4.9.

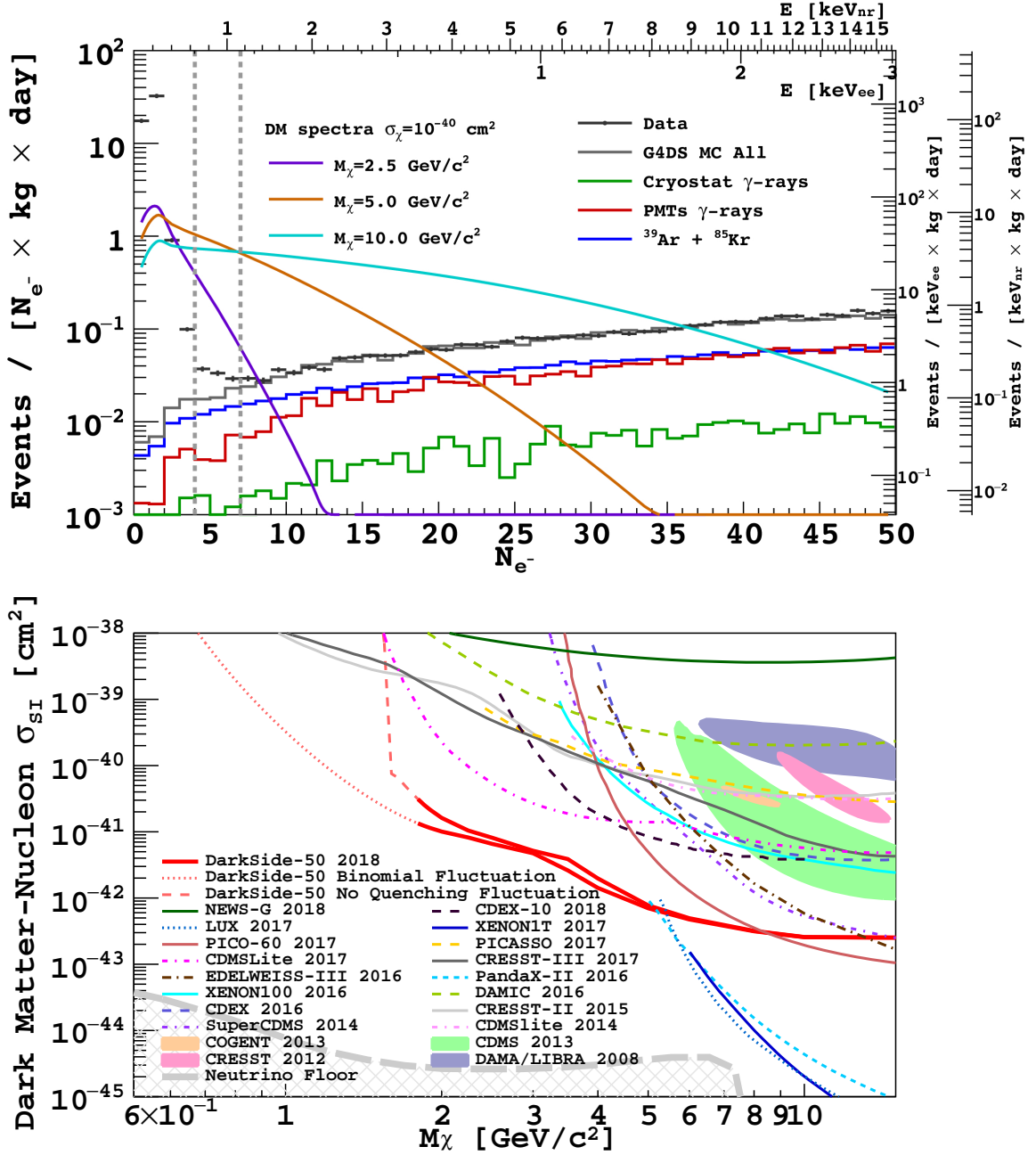


Figure 4.9: (top) The DS-50 N_{e^-} spectra at low recoil energy from the analysis of the last 500 days of exposure compared with a G4DS simulation of the background components from known radioactive contaminants. Also shown are the spectra expected for recoils induced by dark matter particles of masses 2.5, 5, and 10 GeV/c^2 with a cross section per nucleon of 10^{-40} cm^2 convolved with the no energy quenching fluctuation model and detector resolution. The y-axis scales on the right-hand side are approximate event rates normalized at $N_{e^-} = 10e$. (bottom) 90% CL upper limits on spin-independent WIMP-nucleon cross sections from DS-50 in the range above 1.8 GeV/c^2 and comparison to results from other experiments [123, 124, 130, 138–152]. Figure taken from [132]

4.5 Search for Sub-GeV Dark Matter-Electron Scattering

This section summarizes the results of [153] which reported the most sensitive limit on Dark Matter-electron scattering via a “heavy mediator” for masses in the range of 30 MeV/ c^2 and 50 MeV/ c^2 .

4.5.1 Electron Recoil Scale

A direct N_{e^-} energy calibration for very low-energy electron recoils is available from ^{37}Ar which has a half life of ~ 35 days and is produced in the UAr by cosmic rays during refining and transport of the UAr from the USA to Italy [51]. This calibration curve is shown in Figure 4.10.

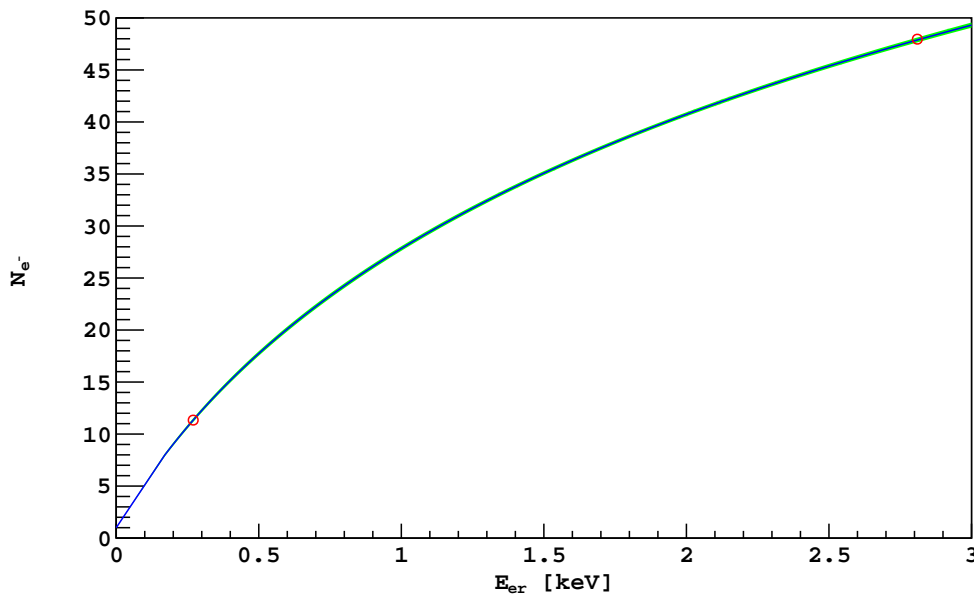


Figure 4.10: Calibration curve used to convert electron recoil spectra to ionization spectra. Below 8 N_{e^-} , it is assumed that there is no recombination and a straight line, that intersects $N_{e^-} = 1$ with a slope determined by the ratio of number of excitations to ionization measured in [154], is used. Above this point, the effects of recombination are included by fitting the Thomas-Imel model [85] to the mean N_{e^-} measured for the 2.82 keV K-shell and 0.27 keV L-shell lines from the electron capture of ^{37}Ar . In order to get good agreement between the model and data, the model is multiplied by a scaling factor. Figure taken from [153].

4.5.2 Results

The same 500 day dataset used in the previous low-mass WIMP analysis was analyzed for this result. The ionization spectrum used for the search can be seen in Fig 4.12. Upper limits on the dark matter-electron scattering cross section are calculated using a binned profile likelihood method. An analysis threshold of 3 drifted electrons is used, which is lower than the threshold used in the previous low-mass analysis. This is able to increase the signal acceptance at the expense of a larger background rate from coincident single electron events (which are not included in the background model as part of the profile likelihood). The hardware trigger efficiency is essentially 100% in the region of interest. The resulting 90% CL exclusion curves are shown in Figure 4.12 for two assumptions of dark matter form factors i.e. $F_{\text{DM}}(q) \propto 1/q^2$ and $F_{\text{DM}}(q) = 1$, for weak and heavy mediators respectively. The results for both mediators along with the background and signal models are shown in Figure 4.12.

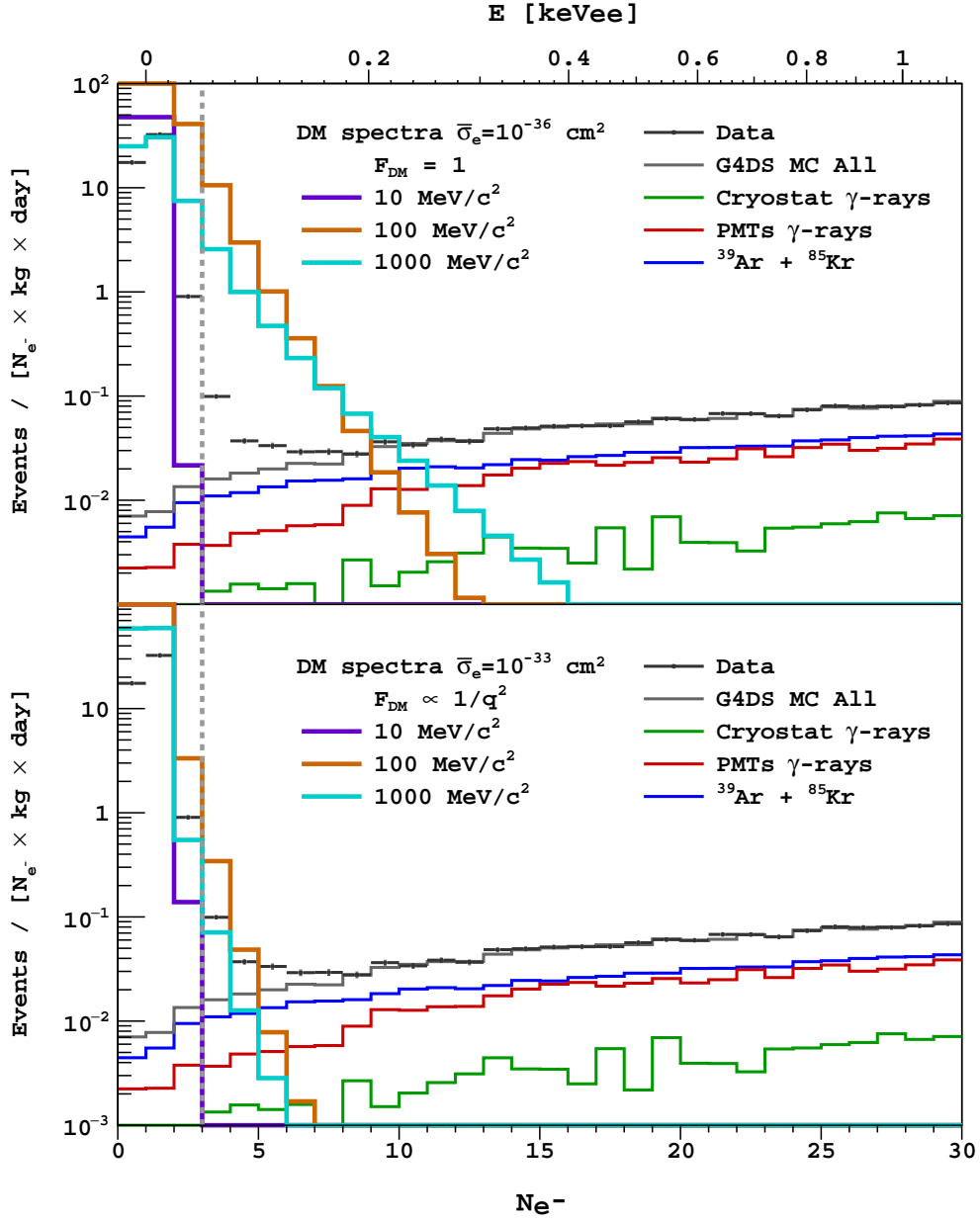


Figure 4.11: The 500 day DS-50 ionization spectrum compared with predicted spectra from the G4DS background simulation [79]. These are the same data and background spectra shown in [132]. Also shown are calculated DM-electron scattering spectra for DM particles with masses m_χ of 10, 100, and 1000 MeV/ c^2 , reference cross section $\bar{\sigma}_e = 10^{-36} \text{ cm}^2$ (top) and $\bar{\sigma}_e = 10^{-33} \text{ cm}^2$ (bottom), and $F_{\text{DM}}(q) = 1$ (top) and $F_{\text{DM}}(q) \propto 1/q^2$ (bottom). The vertical dashed line indicates the $N_{e^-} = 3$ analysis threshold.

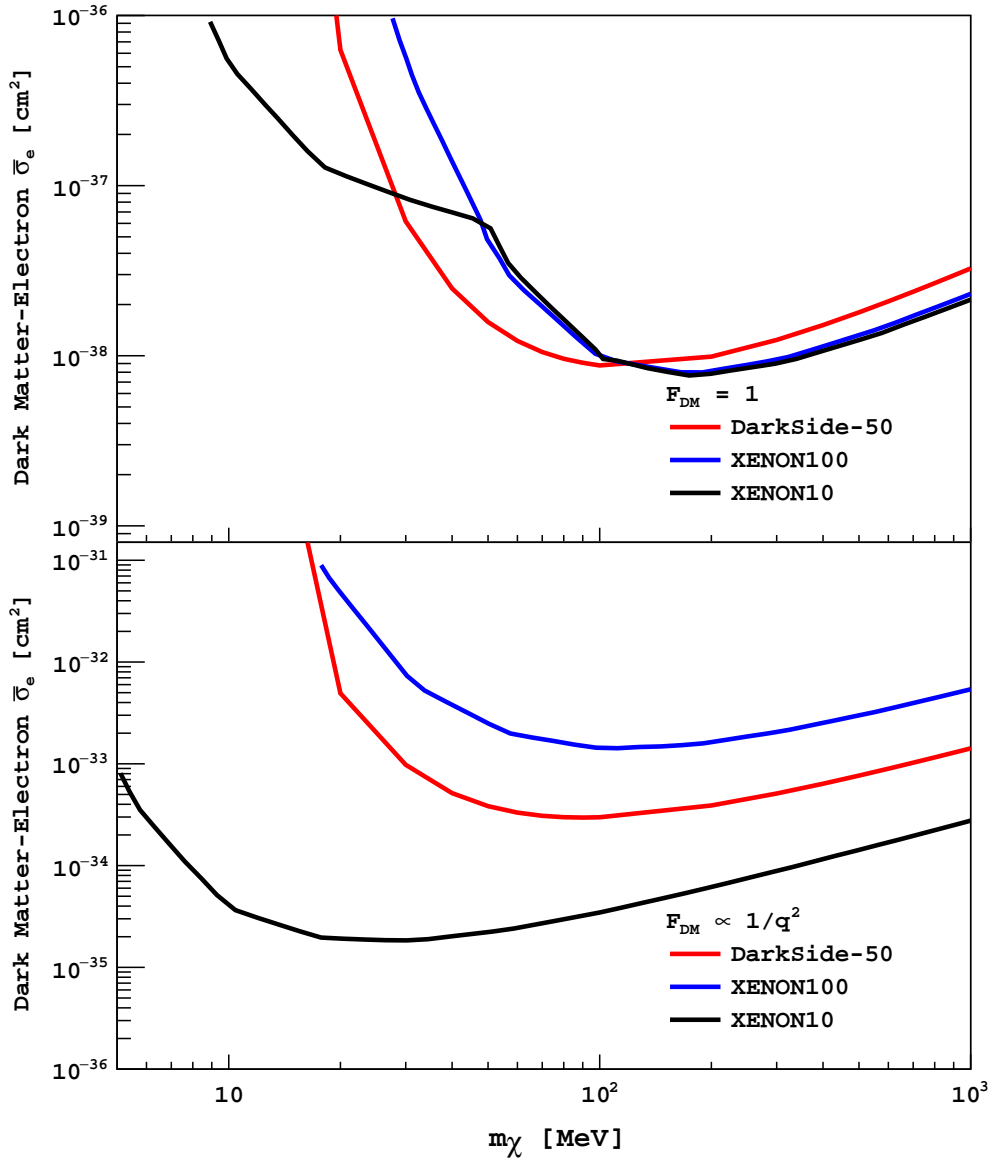


Figure 4.12: 90 % C.L. limits on the DM-electron scattering cross section for $F_{\text{DM}} = 1$ (top) and $F_{\text{DM}} \propto 1/q^2$ (bottom) for DS-50 (red) alongside limits calculated in [155] using data from XENON10 (black) and XENON100 (blue). Figure taken from [153].

Chapter 5

Neutrino-less Double Electron Capture on ^{36}Ar

This chapter gives an overview of some aspects of neutrino physics and some associated open questions. This is then followed by an attempt to answer the question of whether a neutrino is a Majorana particle, via a search for a rare process (neutrino-less double electron capture) which could potentially occur within the DarkSide-50 detector.

5.1 Neutrino : Majorana or Dirac Particle?

A Majorana fermion is a particle that is its own anti-particle. A fermion with mass must have two states of helicity, since it is possible to flip the helicity by moving into a sufficiently boosted frame of reference. It turns out that only left-handed neutrino states and only right-handed states for anti-neutrinos have been observed to date.

For massless fermions (moving at the speed of light), it is known that the chiral projectors are equivalent to the projectors on helicity components (which evaluate the component of spin in the direction of linear momentum). Thus for a massless fermion the helicity is the

same in any reference frame and it commutes with the Hamiltonian rendering it a useful quantum number.

Charge Conjugation, Parity and Time Reversal conservation requires that for any left-handed particle a right-handed antiparticle must exist with opposite charge. Moreover the right handed particle state may or may not exist. However, Parity transforms left and right fields into one another. Therefore the left-handedness of the weak interaction implies that parity is broken in the Standard Model. This symmetry breaking is most obvious in the case of the neutrino, since its parity partner does not exist. Prior to the discovery of neutrino oscillations [156,157], there was no evidence that neutrinos were massive and hence no requirement to extend physics beyond the Standard Model due to helicity. But, the mystery of the absence of a right-handed neutrino state must be resolved, and there are typically two competing hypotheses. Here we consider an experimental search which might rule out or confirm one of these hypotheses which proposes that the neutrino may be it's own antiparticle and hence would be a Majorana particle.

Neutrino-less double electron capture, though physically allowed, is predicted to be an extremely rare process, and has not been observed. It is one of the several possible β decay modes that could occur if, and only if, the neutrino is a Majorana particle.

Therefore neutrino-less double β decay process could be of extreme fundamental significance in particle physics. By definition it is the transition of a nucleus to another nucleus with an increase in proton number by two along with the release of two electrons, without neutrino emission.

$$(A, Z) \rightarrow (A, Z + 2) + 2e^- \quad (0\nu\beta\beta) \tag{5.1}$$

In this equation, there are no leptons on the left hand side, but there are two on the right side *i.e.*, the final state. Thus observation of $0\nu\beta\beta$ would show a violation of lepton number.

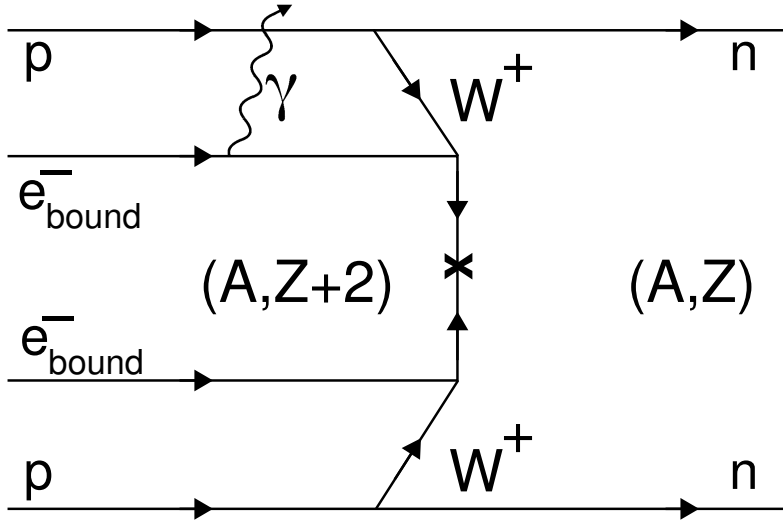


Figure 5.1: Neutrino-less double electron capture in the one photon mode. Figure taken from [158].

Lepton number violation can be considered similar to baryon number violation. Many theories exist which allow for lepton number violation, with a majority of them considering the possibility of light Majorana neutrino exchange.

It is possible that the mechanism that gives rise to $0\nu\beta\beta$ is connected to neutrino oscillation, massive Majorana neutrinos being perhaps the most well motivated hypothesis. Therefore it is possible to categorize $0\nu\beta\beta$ in two different classes; standard and non-standard. The former calls for the mediation of the interaction via a light, massive Majorana neutrino while the latter calls upon other Lepton number violating mechanisms, reducing the contribution from Majorana neutrinos to a negligible level.

Neutrino-less double beta decay can be observed only if ordinary beta decay is energetically prohibited. This is the case for some even-even nuclei (i.e. even proton and neutron numbers), whose ground states are energetically lower than their odd-odd neighbors. If the nucleus with an atomic number higher by one unit has a smaller binding energy (preventing beta decay from occurring), and the nucleus with atomic number higher by two units has a larger binding energy, the double beta decay process is allowed. In principle 35 nuclei can

undergo $0\nu\beta\beta$, though realistically only nine emerge as interesting candidates and these are under investigation. They are ^{48}Ca , ^{76}Ge , ^{82}Se , ^{96}Zr , ^{100}Mo , ^{116}Cd , ^{130}Te , ^{136}Xe , ^{150}Nd . There is no preferred isotope, and one has to find compromises between natural abundance, reasonably priced enrichment and the association with a well controlled experimental technique or the Q-value, because the rate for $0\nu\beta\beta$ decay is typically proportional to Q^5 . The experimental signal is the sum of energy of the two emitted electrons, which should equal the known Q-value. The neutrino-less mode has to be distinguished from 2 neutrino double beta decay

$$(A, Z) \rightarrow (A, Z + 2) + 2e^- + 2\bar{\nu}_e \quad (2\nu\beta\beta) \quad (5.2)$$

which is an irreducible background for the neutrino-less mode. The half-life of $2\nu\beta\beta$ is typically around 10^{19} - 10^{21} years (it is important to note that this process is allowed in the Standard Model), and has been observed for several isotopes.

Experiments searching for neutrinoless double beta decay need to be ultra-pure or heavily shielded and require a thorough understanding of the background, which includes, both radioactive and cosmogenic components. The energy released in the interaction should also be large compared to the natural radioactivity which includes many background gamma lines. (The most significant γ -lines in the decay chains of Uranium and Thorium are approximately 2.614 MeV)

In general, the decay rate for $0\nu\beta\beta$ can be factorized as;

$$\Gamma^{0\nu} = G_x(Q, Z) |\mathcal{M}_x(A, Z)\eta_x|^2 \quad (5.3)$$

Here η_x is a function of the particle physics parameters responsible for the decay. The nuclear matrix element $\mathcal{M}_x(A, Z)$ depends on the mechanism and the nuclear physics. The term $\mathcal{M}_x(A, Z)\eta_x$ can in fact be a sum of several terms, and therefore includes the possibility of destructive or constructive interference. Finally, $G_x(Q, Z)$ is a phase space factor which depends on energies and particle physics. For most of the processes in which only two electrons are emitted, the phase space factor can be considered almost independent of the

mechanism. The biggest effect on G occurs in double beta decay with Majoron emission, where the final state contains one or two additional particles.

It is known that electron capture (EC) always competes with the positron (β^+) emission process regardless of neutrino emission. Because of this, the double (β^+) decay modes can be either ($\beta^+\beta^+$), $EC\beta^+$ or $ECEC$. If double electron capture occurs without neutrino emission, there will be no particle in the final state other than the daughter atom. But, in order to conserve energy and angular momentum, there is a requirement for at least one more emitted particle. The simplest choice is the emission of a photon. ($ECEC\gamma$). In the calculation for regular EC, the assumption is that the 1s-electrons have the highest capture probability. But, if both of the $1s_{1/2}$ are captured, the solitary photon must somehow obtain angular momentum. However, a real photon always has a spin of 1, but the two electrons couple to a spin of zero, and thus this process is disallowed. If one electron from 1s shell and another electron is captured from a different orbital (having a lower probability), it allows a different mode, ($ECEC\gamma\gamma$). In other words, for $0^+ \rightarrow 0^+$ transitions, the capture of two K-shell electrons along with the emission of a single photon is forbidden because it would not conserve angular momentum. Thus the process most likely to occur, is captures from the K and L shells.

The half life is typically described by an equation such as :

$$T_{1/2}^{0\nu} = (G^{0\nu})^{-1} |M^{0\nu}|^{-2} |\langle m \rangle_{ee}|^{-2} \quad (5.4)$$

$M^{0\nu}$ is the nuclear matrix element (NME), and m_{ee} is the effective neutrino mass as defined as :

$$m_{ee} = \sum_{i=1}^3 U_{ei}^2 m_i; \quad (5.5)$$

where m_i are the light neutrino mass-eigenstates and U is the PMNS- matrix defined by ;

$$U = \begin{pmatrix} c_{12}c_{13} & s_{12}c_{13} & s_{13}e^{-i\delta} \\ -s_{12}c_{23} - c_{12}s_{23}s_{13}e^{i\delta} & c_{12}c_{23} - s_{12}s_{23}s_{13}e^{i\delta} & s_{23}c_{13} \\ s_{12}s_{23} - c_{12}c_{23}s_{13}e^{i\delta} & -c_{12}s_{23}s_{13}e^{i\delta} & c_{23}c_{13} \end{pmatrix} \cdot \text{diag} \left(1, e^{i\alpha}, e^{i(\beta+\delta)} \right) \quad (5.6)$$

In the above α and β are the Majorana phases and $s_{ij} = \sin \theta_{ij}$ and $c_{ij} = \cos \theta_{ij}$

The rate can be further expanded (following from the definition of the half-life in equation 5.4) into the following equation, with details well described in [159]:

$$\Gamma_{1s(2s) \times 2p} = \frac{\alpha G_F^4 g_A^4}{2^8 \pi^5 R^2} |M^{0\nu}|^2 |m_{ee}|^2 \tilde{Q} \left[|g_+(\tilde{Q})|^2 + |\tilde{g}_-(\tilde{Q})|^2 \right] \quad (5.7)$$

Here $\tilde{Q} = Q - \tilde{E}'_a - \tilde{E}'_b$ is the corrected Q value, $\alpha = \frac{e^2}{4\pi}$ is the fine structure constant, and $\tilde{g}_-(\tilde{Q})$ and $g_+(\tilde{Q})$ represent form factors.

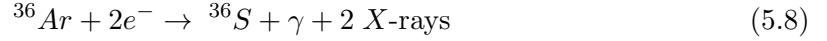
5.2 ^{36}Ar

Argon has over 20 known isotopes but only two (^{40}Ar , ^{38}Ar) are stable, and a third, ^{36}Ar , is observationally stable. The isotope ^{40}Ar comprises over 99.5% of natural Argon on the Earth, while ^{38}Ar accounts for $\sim 0.06\%$ and the abundance of ^{36}Ar is $\sim 0.334\%$.

In the Sun and in primordial star-forming clouds, argon mostly consists of ^{36}Ar ($> 85\%$). Moreover the ratio of the abundance of ^{36}Ar to ^{40}Ar in the atmosphere of the outer planets has been determined to be 8400 : 1 [160].

The possibility that ^{36}Ar originated from explosive nucleosynthesis in stars during core-collapse supernova events is confirmed by its detection in the Crab Nebula [161].

The radiative mode of $0\nu\text{ECEC}\gamma$ in ^{36}Ar provides a signature to search for $0\nu\beta\beta$ measuring the discrete value of the energy of the emitted photon. Two characteristic X-rays, with energies of 2.47 keV and 0.23 keV arising from the K and L shell captures respectively, are emitted in a cascade. The remainder of the energy from the reaction



produces the gamma ray with 431 keV energy.

5.2.1 Search in DS-50

The DS-50 TPC was filled with UAr in March 2015, with the earliest UAr data taken at 0 drift field (also referred to as null field data).

The search for the gamma ray, associated with the radiative decay of ^{36}Ar (see equation 5.8), involves determining its signature in the DS-50 detector via simulation while also evaluating the backgrounds present by performing a spectral fit.

5.2.2 Backgrounds

The main backgrounds to the search are the various radioactive components. These include components like ^{39}Ar and ^{85}Kr which are intrinsic to the argon in the TPC and also external contaminants (mostly gammas) arising from various detector materials such as the cryostat and PMTs.

5.2.2.1 Simulation Procedure

The procedure described here follows the one detailed in Chapter 4 Paolo Agnes's dissertation [80]. The full TPC spectra acquired during the AAr and the 70 day UAr campaigns are shown in Figure 5.4. At low energy, the ^{39}Ar β -decay is the dominant component in the AAr sample, while several gamma full absorption peaks are visible in both the datasets above

the ^{39}Ar endpoint. The spectra extend up to ~ 2.6 MeV and the peaks can be uniquely identified. In order to extract the residual ^{39}Ar activity in the UAr, it is imperative to understand and subtract from the UAr spectra, all the other components.

A fit procedure based on MC spectra was developed. In particular, G4DS was used to simulate all of the β and γ radioactivity arising from the detector components as listed below:

- TPC sensitive volume: ^{39}Ar , ^{85}Kr , ^{42}Ar chain and ^{222}Rn chain.
- PMTs: ^{60}Co , ^{40}K decays and ^{238}U , ^{232}Th and ^{235}U full decay chains. The ^{238}U and ^{232}Th chains are broken to account for possible deviations from secular equilibrium. It is believed that a majority of the activity comes from the boro-silicate glass stems in the PMTs.
- Cryostats: ^{60}Co , ^{40}K decays and ^{238}U , ^{232}Th and ^{235}U full decay chains. The ^{238}U and ^{232}Th chains are broken to account for possible deviations from secular equilibrium. A uniform distribution of the decays within the cryostat is assumed.
- Fused silica windows: ^{40}K decay and ^{238}U , ^{232}Th and ^{235}U full decay chains. Although the fused silica is expected to be more radiopure compared to the other detector components, it's proximity to the sensitive volume allows for production of signals in the TPC

The presence of ^{85}Kr in UAr was not expected, so there was no purification procedure undertaken before filling the detector. The ^{85}Kr β decay endpoint is at 687 keV and hence it is hard to differentiate the spectral shape from that of ^{39}Ar and a simultaneous fit did not converge before this component was added. The ^{85}Kr decay has a channel of $\beta + \gamma$ decay with a branching ratio of 0.434%. Here the β has an endpoint of 173 keV with a decay to the excited state of ^{85}Rb . The de-excitation of this excited state results in the emission of a 514 keV γ ray with $\tau_{1/2} = 1.015 \mu\text{s}$. The search for this $\beta + \gamma$ coincidence in the UAr

dataset (first performed with the 70 days data) facilitated the confirmation of the presence of ^{85}Kr in the LAr. The details for this search are documented [57].

A plausible contamination of ^{42}Ar was also considered. This is a nuclide of anthropogenic origin, even if its presence is not expected in the UAr. The ^{42}Ar decay ($\tau_{1/2} = 32.9$ y) leads to unstable ^{42}K ($\tau_{1/2} = 12.36$ h). Both these decays are β decays, with endpoints of 599 keV and 3525 keV respectively. The ^{42}K decay is accompanied by a 1524 keV gamma with 18% branching ratio.

Most of the simulated radioactivity, originating in various different materials, is actually due to the same decays or decay chains. This shows similarities in the TPC energy spectra.

Three observable quantities were identified as candidates to break the degeneracy between the various spectra. These are as follows:

- S1
- tdrift
- $S1_{late}$

S1 and tdrift were used for events with single scatters while $S1_{late}$ was used for events with multiple scatters in the LAr volume. $S1_{late}$ is defined as $(1 - f_{90}) \times S1$.

The multiple scatter spectrum enables the information with full absorption peaks of the various embedded gammas. The single scatter spectrum which is essentially a 2 dimensional distribution (S1 v/s drift time) allows for spatial information to be encoded. One may consider for example, that the drift time distributions for the radioactive components in the cryostat are different from that of the components in the PMTs. It is expected that the components from the PMTs populate the tails of the drift time distribution while the components from the cryostat are more evenly distributed in the z direction.

While the PMTs and cryostats produce a similar energy spectrum in the TPC, the two

components show different drift time distribution of the events. On the other hand, the contamination in the fused silica windows is closer to the TPC active volume. These show different features in the TPC energy spectrum when the events are concentrated at the top and at the bottom of the active volume as in the case of PMTs.

5.2.2.2 The $S1_{late}$ Spectrum

The ADC boards are expected to saturate in the first tens of nanoseconds of the ordinary scintillation pulse. This is because the fast component of the scintillation is clustered in the first 100 ns while the slow component is emitted over several microseconds.

The f_{90} parameter as previously introduced, is defined as :

$$f_{90} = \frac{\int_0^{90\text{ns}} S(t)dt}{\int_0^{7\mu\text{s}} S(t)dt} \quad (5.9)$$

The saturation of the ADC is expected to be carried away by the first 90 nanoseconds of the pulse and hence it is anticipated that the $S1_{late}$ variable is privy to very little saturation.

The loss of resolution from using the $S1_{late}$ variable is a recognizable pitfall. Therefore a choice is made to use the data acquired with the drift field turned off. In this case, a large fraction of the deposited energy should be translated into scintillation light *i.e.*, S1, since an S2 signal is absent. It is known that the S1 light yield of the TPC is higher for null-field as opposed to a field of 200 V/cm. The values for the LY are ~ 8 PE/keV and ~ 7 PE/keV respectively [35, 51]

The multiple pulse spectrum suffers from the non-uniformity generated by the optics of the internal LAr. The full absorption peaks are due to events other than single scatter events. The gamma ray dissipates its energy by multiple Compton scattering multiple times. Every interaction can occur at varying depths of the sensitive volume and the fact that the light collection efficiency is position-dependent inside the sensitive volume, has to be taken into account. Thus, a correction is applied in order to retrieve the detector resolution.

The $S1$ variable is corrected for z -dependence of the light collection efficiency according to the fit function shown in Fig 5.2

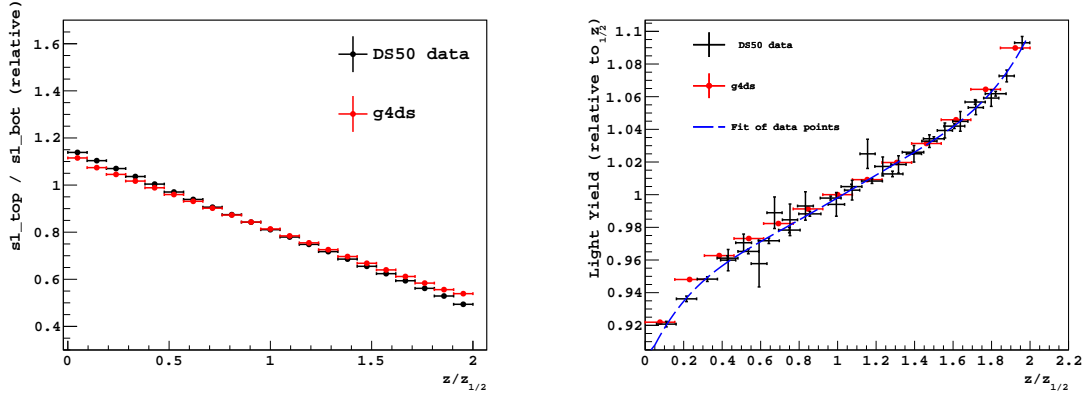


Figure 5.2: Relative light collection (left); and top-bottom ratio in light collection (right) as a function of the vertical position of an event. The normalization is relative to the centre of the TPC such that $z/z_{1/2} = 0$ corresponds to the top while $z/z_{1/2} = 2$ corresponds to the bottom. Figure taken from [80].

Without the drift field, there is of course no secondary scintillation and it is not straightforward to extract the depth at which the event occurred as one does usually using the drift time variable. Use is made of the z -dependence of the Top-Bottom Asymmetry (TBA) shown in Fig 5.2, in order to recover a weighted average position of the event.

To calculate the absolute light yield, some of the ^{83m}Kr calibration runs are also included in the dataset, in order to add data at low energy (41.5 keV). At high energy, the peaks of ^{208}Tl (2614 keV), ^{214}Bi (1764 keV), ^{40}K (1461 keV), ^{60}Co (1332 keV and 1173 keV) are visible. The sub-MeV energy region includes many gamma lines from the ^{232}Th , ^{238}U and ^{235}U decay chains and their identification is not straightforward. For instance, the 583 keV line of ^{208}Tl from the ^{232}Th chain overlaps with the 609 keV line of ^{214}Bi from the ^{238}U decay chain. At lower energy the density of gamma lines is larger and only the most prominent one is used (352 keV line from ^{214}Pb).

A fit was performed for each of the peaks using a Gaussian curve after subtracting the local background. The mean of the $S1_{late}$ value is then divided by the true energy in order

to derive the light yield. The light yield as a function of energy is then fit (shown in Figure 5.3), with the equation describing the dependence :

$$LY_{late} = \frac{6.52}{1 + 0.065 \cdot e^{-E/0.029}} - 5.058 \times 10^{-5} \cdot E \quad (5.10)$$

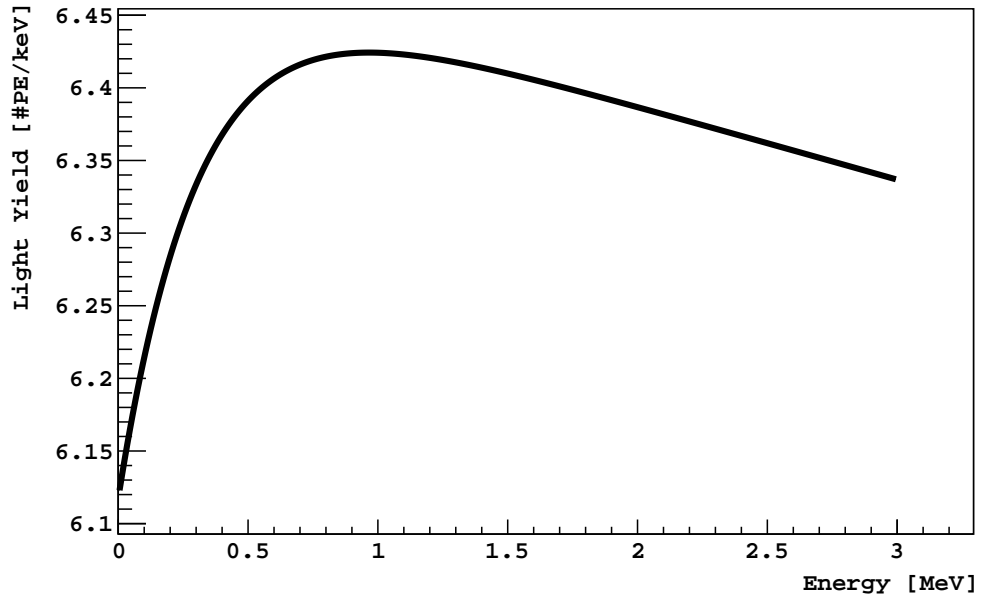


Figure 5.3: The light yield as a function of energy when the drift field is turned off.

Normalization of Spectra

The normalization between the S1 vs tdrift (field on, single scatter) distributions and S1late (field off) spectra is applied based on the different lifetime of the datasets. A few basic cuts are applied to the data (see Section 4.2.1 for details)

There are no further cuts applied to generate the all-pulse spectrum. To generate the (S1, tdrift) distributions, the removal of multiple scatter events accounting for the relative normalization of the datasets is necessary.

Systematic uncertainties can arise from a series of factors. Some of these are :

- A clustering algorithm (described in Section 3.2.1 of [80]) was used to estimate the number of reconstructed pulses in simulated data. The algorithm was tuned for a range of ($S1 < 1000$ PE) while the clustering condition may well be energy dependent.
- There is a non negligible probability for a scintillation pulse (S1 or S2) to induce an electron emission from the cathode (S3, or an echo). Having one or more echoes inside the acquisition window increases the number of reconstructed pulses, but this does not reflect the number of interactions in the sensitive volume. The echo pulses can be identified because of the deterministic time difference with respect to the pulse which initiated the echo.
- During the runs with the drift field turned on, the acquisition window is larger with respect to the one used in field off data. When field on data is analyzed, the minimum required time difference between two events is 1.35 ms. This implies that the probability of pile-up is different among the datasets and must be accounted in the calculation of the lifetime.

The aggregate of these effects is expected to have a %-level impact on the estimate of the normalization factor between the two datasets (single scatter field-on and multiple scatter field-off). In order to account for the difference, a “nuisance parameter“ for

each pair of spectra was introduced in the fit minimization procedure

The fit is performed via a χ^2 minimization. The χ^2 is computed simultaneously on the 2 dimensional (S1 vs drift time) histogram and the $S1_{late}$ spectrum. The nuisance parameters introduced above are used to weigh the ratio between single and multiple scattering for each background component. The fitting intervals (S1, drift time and $S1_{late}$) and the bin width of each histogram are modified to determine the impact on the fit result. The free parameters of the fit are the amplitude of each component and the central values of the “nuisance” parameter. A Gaussian constraint, with some given weight, included in the χ^2 , forces this parameter to be close to one. The user is allowed to:

- Choose which background components are included in the fit
- Set the initial value for each amplitude
- Fix the weight to be assigned to each nuisance parameter in order to have a maximum deviation of the order of a few %.

Figure 5.5 shows one fit example. Data is in dark blue (S1 and drift time) or black ($S1_{late}$), the sum of the components according to the fit results is in red. As already mentioned, the fitting interval for the S1 variable should not exceed 5000 PE, because the S1 variable does not include a correction for the PMT saturation. The drift time fit interval is (40, 336) μs and the $S1_{late}$ spectrum is fitted in the (1000, 22000) PE range. The results of the fit, performed with 12 background components and 24 free parameters, reveal low sensitivity to some components and some degree of degeneracy. Thus it was decided to include in the fitting procedure the knowledge of the specific activity of some detector components (most of these were γ counted). The possibility that the user could set the starting value of one or more component activities to the expected value from screening, was also included. A Gaussian constraint, included in the calculation of the χ^2 , is then applied, with a weight calculated from the error on the screening measurement. This fit does not take into account

uncertainties on the overall normalization as is the case for an extended maximum likelihood fit. Possible sources of systematic uncertainty associated with the fit procedure were identified as:

- Difference in statistics of the MC spectra. This difference arises due to the different probability of interactions inside the sensitive volume for gammas coming from different detector materials. Each simulation was required to have at least 2×10^4 events which deposit energy in the TPC. In some cases (^{39}Ar , ^{85}Kr) this number is larger than 2×10^6 events. Thus, statistical fluctuations for each background component can have varying impacts
- The composition of the χ^2 s from the histograms is dependent on the bin widths of each. The statistical errors on the MC spectra were included in the χ^2 calculation in order to compensate for the difference in statistics.

5.2.2.3 Best Fit Result

In this section the best fit results for the various activities are reported, specifically in the context of identifying any ^{36}Ar activity.

Figure 5.4 represents the fit that had been performed for field-off data collected prior to the 70 day UAr analysis [51]. See Section 4.2 for some details on the analysis. Essentially the procedure was repeated for a fit involving one more spectral component *i.e.*, of ^{36}Ar . This fit does not account for overall normalization of the number of events.

As seen in Figure 5.5 the resultant activity of ^{36}Ar is found to be null while the activity levels for the other components are in reasonable agreement with screening results [51] and other estimates [80, 89]. This implies that no evidence of neutrino-less double electron capture on ^{36}Ar was found, and at the very best, a limit can be placed on the half-life of such a process.

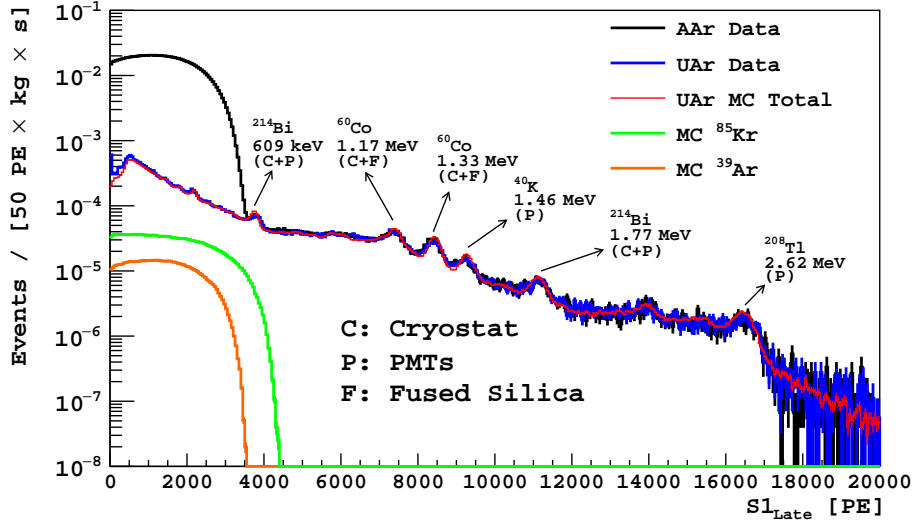


Figure 5.4: Measured field-off spectra for UAr (blue) and AAr (black) targets, normalized to exposure. Shown in the MC fit to the UAr data (red) and individual components of ^{85}Kr (green) and ^{39}Ar (orange) extracted from the fit. The data represents the ~ 4 day dataset collected and analyzed by DarkSide [51] right before the 70 day campaign. Figure taken from [51].

5.2.3 Extracting a Limit - Preliminary Results

A lower limit on the half-life of $0\nu\text{ECEC}$ on ^{36}Ar can be extracted by using a simplistic frequentist method. Essentially one needs to evaluate a list of quantities to be described. Suppose the number of events of the process that occur in the setup of the detector is given by \mathbf{S} . Here \mathbf{S} is simply given by the product of the activity of the sample and the exposure. The former is simply given by the inverse of the half-life multiplied by $\ln 2$. Here the half-life ($T_{1/2}$) is the quantity we want to determine, so we must find a way to flip the problem such that we have a handle on \mathbf{S} . The quantity of the sample can be easily calculated if we know the fraction of ^{36}Ar represented by (f_{36}) which has been measured by H. Back [162, 163]. It is required to multiply this fraction with the total mass of the liquid argon (M_{LAr}) which is the sample under investigation, and also by the livetime (t). Subsequently this quantity needs to be scaled by Avogadro's constant (N_A) divided by the molar mass of ^{40}Ar (m_{Ar}), which in turn gives the number of scattering centers. Finally it must be scaled

by the efficiency (ε) to find the number of such decays, which is obtained directly from MC (G4DS).

Putting all this together we have the following equation :

$$\mathbf{S} = \ln 2 \cdot \frac{\varepsilon_d}{T_{1/2}} \cdot \frac{N_A \cdot M_{LAr} \cdot f_{36} \cdot t}{m_{Ar}} \quad (5.11)$$

Inverting this in terms of the half-life, one obtains :

$$T_{1/2} = \ln 2 \cdot \frac{\varepsilon_d}{S} \cdot \frac{N_A \cdot M_{LAr} \cdot f_{36} \cdot t}{m_{Ar}} \quad (5.12)$$

The following quantities are known along with (m_{Ar}) and (N_A) :

- $t \sim 103.4$ hours
- $f_{36} \sim 0.0075\%$
- $M_{LAr} \sim 153$ kg
- $\varepsilon_d \sim 22\%$

Substituting these terms in one obtains the following : $T_{1/2} = \frac{3.38 \times 10^{20}}{S}$ years. So S must now be evaluated. This can be done if the problem is phrased in the following fashion : “How many signal events would need to be identified as background events such that a noticeable discrepancy can be observed between the modeled background and the new artificially generated spectrum?” This can be answered by choosing a desirable statistical significance level to evaluate the difference between the artificially built spectrum and the truly modeled background spectrum obtained from the fit.

The quantity is evaluated as a change in the χ^2

$$\Delta\chi^2(N) \equiv \sum_{i=\min\text{-bin}}^{\max\text{-bin}} \frac{[h_{background}(i) - h_{artificial}(i, N)]^2}{h_{background}(i)} \quad (5.13)$$

Here $h_{background}(i)$ represents the contents of the i^{th} bin of the histogram which approximates the background spectrum in $S1_{late}$. $h_{artificial}(i, N)$ represents the contents of the i^{th}

bin of the histogram which approximates the spectrum built by swapping N signal events for an equal amount of background events. Hence the quantity $\Delta\chi^2(N)$ is a function of N , and can be evaluated by varying N from 0 to a desired number which returns a sufficiently statistical deviation (predetermined to be 2.71 for one degree of freedom [26]).

From Figure 5.7 one obtains a value of $S = 261$ events and this gives the resultant half life as $T_{1/2} = 1.3 \times 10^{17}$ years

Currently the best limit on the $0\nu\text{ECEC}$ on ^{36}Ar has been set by the GERDA collaboration [158] where a lower limit of 3.6×10^{21} years with a 90% Bayesian credible interval is claimed.

The Quasi Random Phase Approximation calculations [159] indicate that the true half-life of this decay is $\sim 10^{38}$ years - which is consistent with the notion that ^{36}Ar is primordial in nature (See Section 5.2). The best limit from GERDA differs by 19 orders of magnitude from the calculated result. The result obtained here, through DS-50 data, is ~ 4 orders of magnitude higher than the current best limit. This difference can primarily be attributed to negligible presence of ^{36}Ar (~ 11 g) within the LAr used in DS-50 as opposed to ~ 298 kg in the GERDA setup.

It is expected that the experimental detection of $0\nu\text{ECEC}$ will be extremely challenging even in the coming years. Furthermore, finding the mechanism that dominates decay rates will require measurement for different isotopes and this also remains to be determined [164].

5.2.4 Uncertainties

Statistical uncertainties on the lower limit of the half-life of the decay were already folded in to the $\Delta\chi^2$ calculation. For the fitting procedure, the statistical uncertainties arising from the MC generated spectra were added in quadrature to the uncertainties arising from data. It is understood that the fit performed does not return a “reasonable” p-value according to standard convention. But extreme results are still plausible since the amount

of data is so large, and in fact the fit is in good agreement with screening results. Fits were performed on random subsets of data ($< 10^3$ events), and much better p-values were found as expected. Quoting directly from [165]; “All measures of goodness-of-fit suffer the same serious drawback. When the sample size is small, only the most aberrant behaviors will be identified as lack of fit. On the other hand, very large samples invariably produce statistically significant lack of fit. Yet the departure from the specified distributions may be very small and technically unimportant to the inferential conclusions.” Systematic uncertainties coming from the generation of MC spectra are extremely hard to estimate, and it is known that G4DS, or for that matter any MC, cannot capture the totality of the micro-physics of the DS-50 detector. Some checks, as prescribed by [166] were made and fits were re-performed, but indicated that the tuning of G4DS parameters was already optimal. Further, a variation of the light yield by $\pm 3\%$ produced significantly worse fits which suggested that the empirical function describing the light yield described the data well. Systematic uncertainties on the half-life of the decay can arise from uncertainties in any of the quantities that appear in equation 5.2.3. All of these quantities are measured to high precision and a $\sim 10\%$ level variation of these does not lead to a significant difference in the final result.

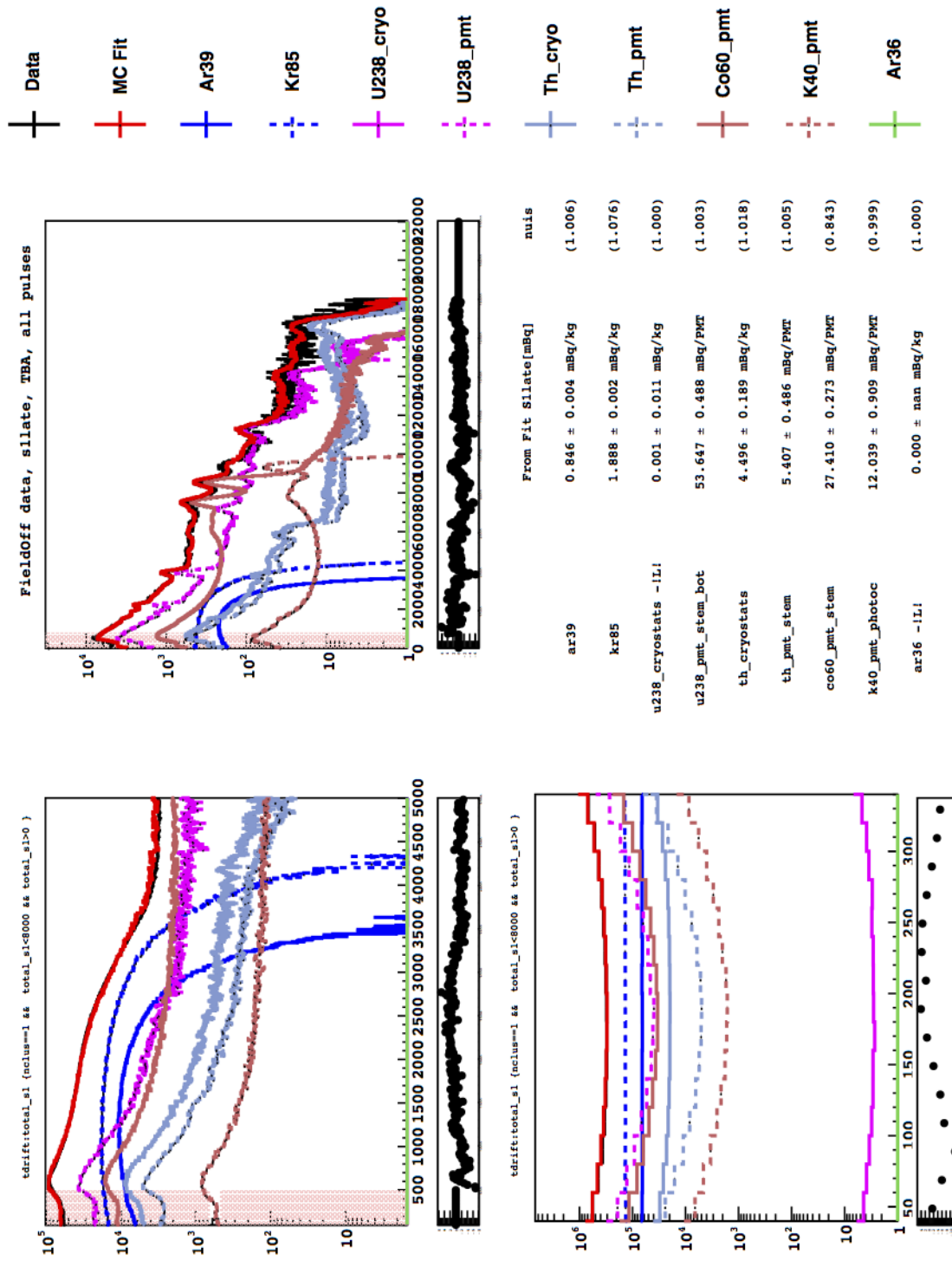


Figure 5.5: Best fit result. Top left shows the S1 distribution, bottom left shows the tdrift distribution and top right shows the $S1_{late}$ distribution. The data is in black while the fit is in red. The best fit result returns 0 activity of the ^{36}Ar decay.

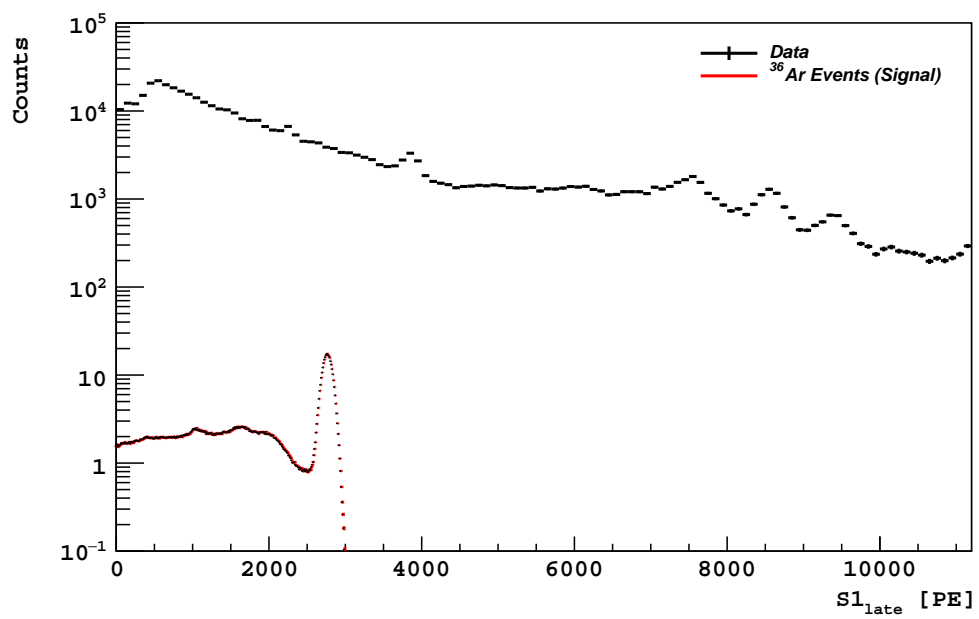


Figure 5.6: An arbitrary scaled version of ^{36}Ar decay spectrum superimposed on the $S1_{late}$ background spectrum.

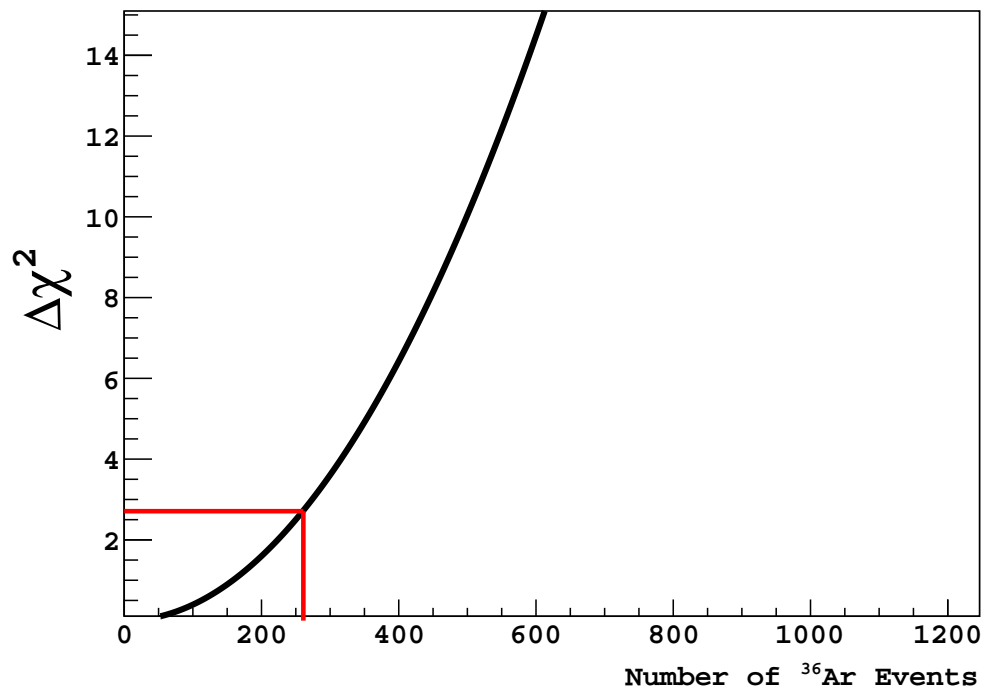


Figure 5.7: The change in χ^2 as a function of the addition of ^{36}Ar decay events. The horizontal red line indicates on the y-axis a change in χ^2 corresponding to 2.71 while the vertical red line indicates the number of events (261) that were required to induce this change.

Chapter 6

Search for Solar Axions

This chapter gives an overview of axions, which are a class of particles initially hypothesized to solve the strong CP problem but at the same time, are viable dark matter candidates. This is then followed by a search for axions coming from the Sun and potentially interacting in the DS-50 detector.

6.1 Motivation

The Strong CP Problem

The QCD Lagrangian can be written as :

$$\mathcal{L}_{QCD} = \mathcal{L}_{\text{pert}} + \theta \frac{g^2}{32\pi^2} G\tilde{G} \quad (6.1)$$

where the first term is the standard Lagrangian associated with QCD. The second term, however, is a result of non-perturbative effects. In the above, G is the gluon field-strength tensor and \tilde{G} is its dual. The second term actually violates CP, but experimentally it is known that the strong interaction does not, in fact, violate CP. The θ term can in principle

violate CP and give rise to an electric dipole moment associated with the neutron [167] ($d_n \approx 3.6 \times 10^{-16} \theta_{\text{QCD}} e \text{ cm}$) with e as electron charge. The dipole moment has been constrained at the 90% CL to be $|d_n| < 2.9 \times 10^{-26} e \text{ cm}$ which further indicates that $\theta < 10^{-10}$ [168].

It was realized by Weinberg [169] and Wilczek [170] that the Peccei-Quinn mechanism [171] introduced extremely light pseudo-scalar Nambu-Goldstone bosons. These bosons are called axions, and they receive mass because of QCD instanton effects [172]. It was realized that such extremely weakly interacting particles may well provide a cooling mechanism for stars. While their experimental detection becomes very challenging, they also become well-motivated dark matter candidates. These axions (or similar particles) could account for the correct relic density and halo dark matter, if they are produced with zero momentum by the so called misalignment mechanism [173].

6.2 Solar Axions

Solar axions would be produced by the Primakoff process, $\gamma + Ze \rightarrow Ze + a$ which is mediated by a virtual photon. CAST [174,175] provides the best limit on the axion-photon coupling, $g_{a\gamma}$ which is estimated to be $< 0.88 \times 10^{-10} \text{ GeV}$ at the 95% Confidence Level.

The axion luminosity given by L_a accounts for a negligible perturbation of the Sun if the coupling constant is below the limit set by CAST. But, for couplings larger than this limit, the energy loss demands a modification of the solar structure. To conserve the observed amount of surface energy emitted, the energy produced by nuclear burning needs to be increased. This implies that the energy producing regions need to heat up. The extra losses should have been operating for the lifetime of the Sun ($\sim 10^9$) years, and a solar model accounting for these mechanisms must match the present day radius and luminosity. This can be done by adjusting the unknown pre-solar helium abundance.

PQWW Axion The PQWW axion model introduces a complex scalar field, ϕ , to the Standard Model as a second Higgs doublet. The u-type quarks obtain mass from one Higgs field while the the other Higgs field gives mass to the d-type quarks. The representation of ϕ is then fixed in $SU(2) \times U(1)$. The complete Lagrangian is invariant under a global $U(1)_{PQ}$ symmetry, under chiral rotations. The PQ field couples via the Yukawa interactions giving mass to the fermions. The invariance of these terms under the $U(1)$ symmetry constrains the PQ charges of the fermions. Exactly like the normal Higgs field, φ has a symmetry breaking potential given by :

$$V(\varphi) = \lambda \left(|\varphi|^2 - \frac{f_a^2}{2} \right)^2 \quad (6.2)$$

which it obtains a vev (vacuum expectation value) of $\langle \varphi \rangle = f_a/\sqrt{2}$ at the Electroweak phase transition. Analogous to the Higgs field case, the scale of the vev is fixed at $f_a \approx 250$ GeV.

After the electro-weak symmetry breaking, there remain four real neutral scalar fields. The Z-boson acquires mass from one, one is the SM Higgs, one is the heavy radial φ field and the remaining is the angular φ field. The degree of freedom in the angular direction can be described as (after appropriate normalization) $\langle \varphi \rangle e^{i\phi/f_a}$. The field ϕ is the axion field and the axion is the Goldstone boson of the spontaneously broken $U(1)_{PQ}$ symmetry. All the axion couplings are subdued by the scale f_a which in the PQWW axion model is established to be the electro-weak vacuum expectation value. In this model, f_a is too small, hence the axion couplings are very large. Therefore this model has been excluded by experiments [176]. In the KSVZ and DFSZ models the PQ field is independent of the electro-weak scale. The decay constant hence becomes a free parameter in the model and is permitted to be large enough such that the models are not excluded. These axions are called invisible axions.

KSVZ Axion The KSVZ axion model [177, 178] requires the introduction of a heavy quark doublet, Q_L, Q_R where the subscript represents the charge under a chiral rotation.

The PQ scalar field, ϕ has a charge of 2 under chiral rotations, but now becomes a standard model singlet. The PQ field and heavy quarks interact via the Yukawa term (which is PQ-invariant). This provides the heavy quark mass :

$$\mathcal{L}_Y = -\lambda_Q \phi \bar{Q}_L Q_R + h.c \quad (6.3)$$

Here, λ_Q , the Yukawa coupling is a free parameter of the model. There is a global $U(1)_{PQ}$ symmetry which behaves as chiral rotation angle of $\alpha = \phi/f_a$ and hence shifts the axion field.

DFSZ Axion The DFSZ axion [179] couples to the Standard Model via the Higgs sector. Two Higgs doublets, H_u, H_d are present in this model. However, the complex scalar field φ is introduced as a singlet. The global $U(1)_{PQ}$ symmetry is spontaneously broken by the potential previously introduced in equation 6.2.

The Higgs fields and the PQ field interact via a scalar potential given by $V = \lambda_H \varphi^2 H_u H_d$. When the PQ symmetry is broken and φ obtains a vacuum expectation value, three parameters need to be tuned in order to match the observed standard model Higgs field and the eletro-weak vacuum expectation value. These tunable parameters are, the coupling constant λ_H , and the two parameters in the Higgs potential.

6.2.1 Axio-Electric Effect

The axio-electric effect [180–182] is analogous to the photo-electric effect where a boson (axion) is absorbed by a bound electron, which is subsequently emitted from the atom. See Figure 6.1 for a general diagram of this process.

Flux and Cross Section

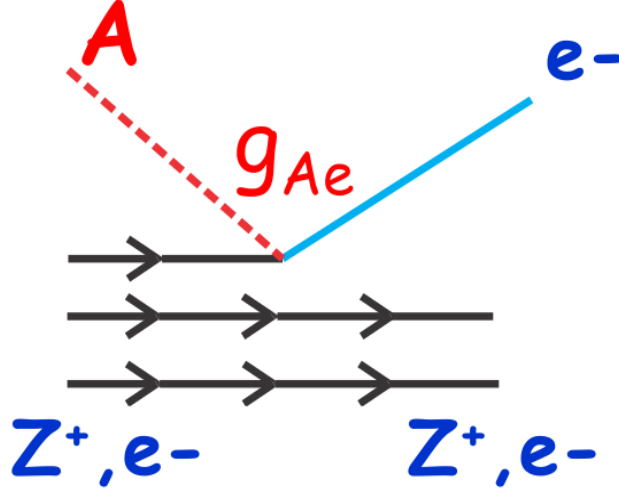


Figure 6.1: Axio-electric effect depicted by a sketch. Here g_{Ae} represents the coupling constant between electrons e and the axion A . Figure taken from [183].

The cross section for the axio-electric effect (σ_{Ae}) is given by the following equation :

$$\sigma_{Ae} = \sigma_{pe}(E_A) \frac{g_{Ae}^2}{\beta_A} \frac{3E_A^2}{16\pi\alpha_{em}m_e^2} \left(1 - \frac{\beta_A^{2/3}}{3}\right) \quad (6.4)$$

Here σ_{pe} refers to the photoelectric cross section. E_A represents the energy of the incoming axion, g_{Ae} is the axio-electric coupling constant, β_A is the velocity of the incoming axion. m_e is the mass of the electron and α_{em} is the fine structure constant. There are many processes that could lead to the production of axions in the Sun. The solar axion flux has been calculated previously [184, 185] and attempts to parameterize it have also been made [186]. The coupling of axions to electrons leads to various reactions that can contribute to the solar axion flux. Some of these critical reactions are called the ABC reactions : Atomic Axio-Recombination/De-excitation, axio-Bremsstrahlung in electron-Ion or electron-electron collisions, and Compton Scattering. It is now clear that electron-ion and electron-electron axio-bremsstrahlung are the largest contributors to the solar axion flux arising from the axio-electric coupling.

The flux used is valid for axions with masses $< 1 \text{ keV}/c^2$ without the need for significant corrections.

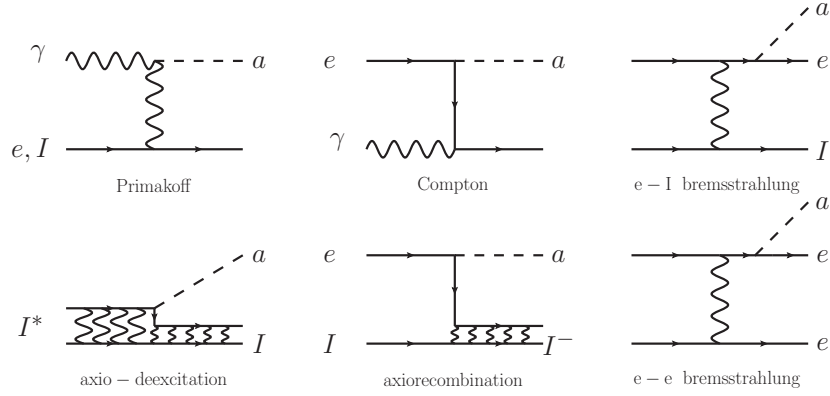


Figure 6.2: ABC reactions responsible for production of solar axions in non-hadronic models of axions. Figure taken from [184].

6.3 S1 Sensitivity Check

In this section the sensitivity of DS-50 to the axio-electric coupling constant is inspected. No treatment of systematic uncertainties is presented and hence a robust limit cannot be claimed. A simple statistical procedure is performed to extract a possible limit.

6.3.1 Rate in DS-50

The rate expected in a hypothetical LAr volume is calculated by computing the convolution of the solar axion differential flux (taken directly from [184]) as shown in Figure 6.3 and the cross section as a function of the incoming axion energy, which is described in equation 6.2.1.

The calculated differential rate as a function of incoming axion energy, in units of Counts $keV^{-1} kg^{-1} s^{-1}$ is then shown in Figure 6.4.

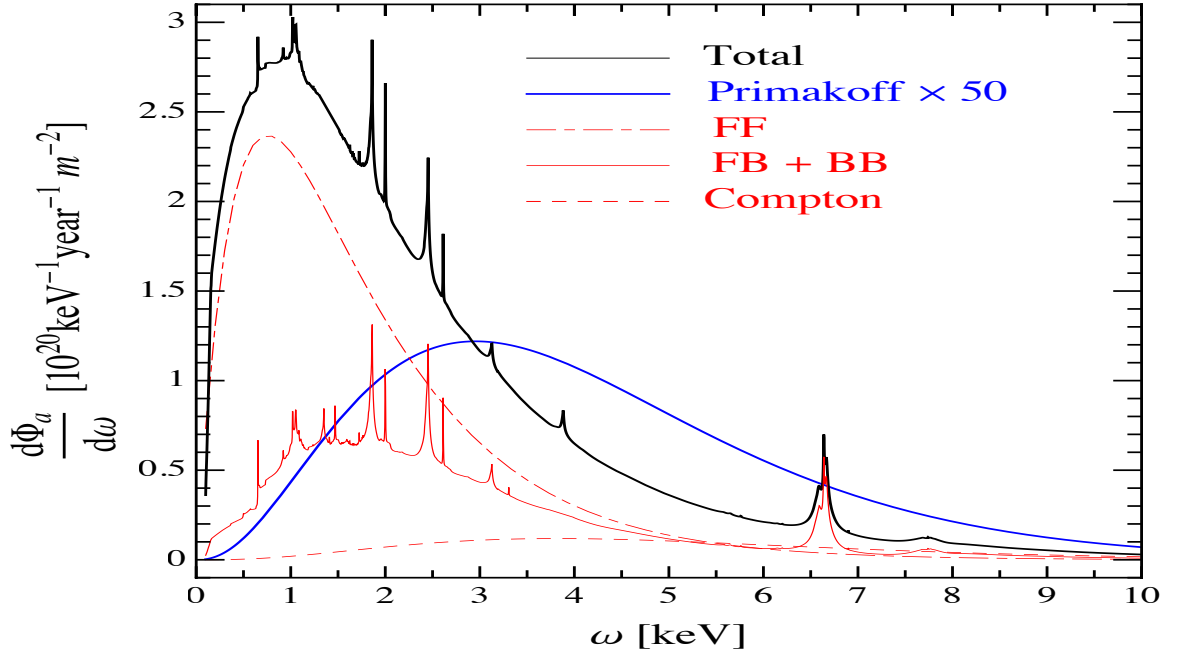


Figure 6.3: Solar axion flux as described by 4 contributing processes. Figure taken from [184].

To examine the rate expected in DS-50, it is necessary to fold this theoretical rate with the detector response. There are several ways to execute this. The one chosen here, involves passing this rate to G4DS to produce a differential rate as a function of electron recoil energy. The assumption made prior to this step is that all the energy of the axion is transferred to the recoiling electron of the argon atom. This is a relatively safe assumption since the ionization energy is typically \sim eV while the axion energy is \sim keV.

To state mathematically,

$$\frac{dR}{dE_A} = \frac{dR}{dE_{Er}} \quad (6.5)$$

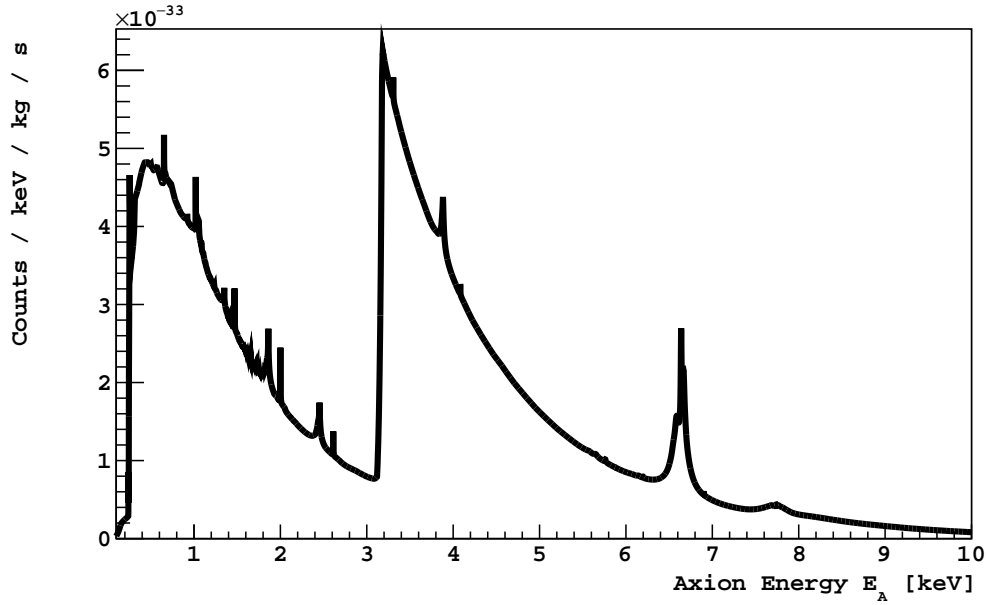


Figure 6.4: Theoretical rate of solar axions interacting in in DS-50 as a function of axion energy.

6.3.2 Data Set and Cuts

The dataset used for this search was the same as the one curated for 540 day WIMP search analysis [81]. The data were collected between April 30, 2015 and April 25, 2017. As discussed in Chapter 5, cuts made on the field-on data were basic quality cuts (discussed in Section 4.2.1), along with the following requirements:

- Single Scatter
- $S2 > 20$ PE
- f_{90} of S1 > 0.05
- f_{90} of S2 < 0.2

Very tight cuts on fiducial volume were made as shown in Figure 6.7. This is because at these low energies < 100 PE there are some unexplained backgrounds, mainly originating

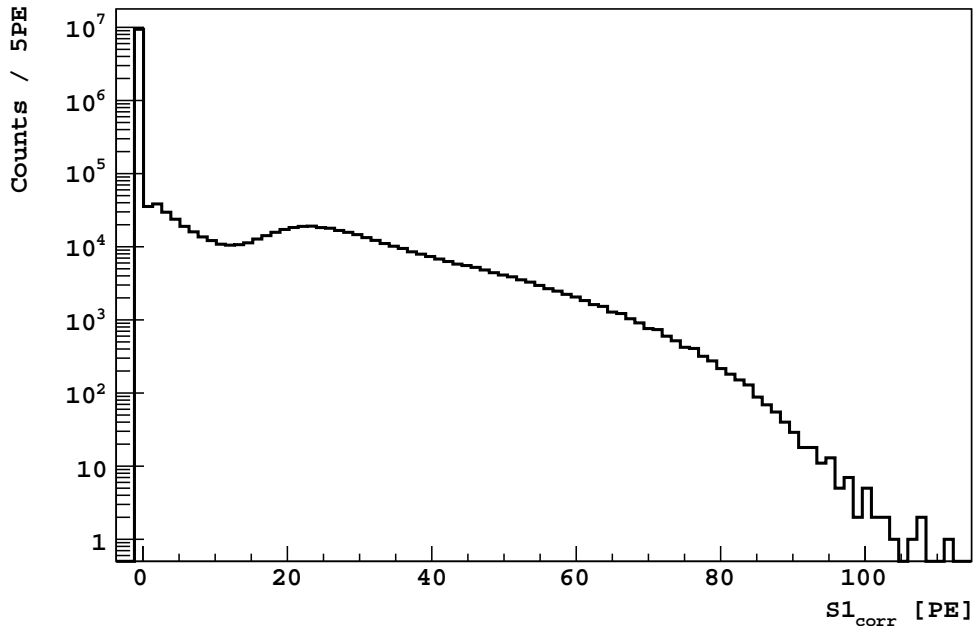


Figure 6.5: Full axion S1 spectrum after simulating 10 million events with detector effects through G4DS. It can be seen that a large number ($\sim 96\%$) of the events deposit too little energy in the sensitive volume and hence leave no detectable signal.

from the sides and the top or bottom of the detector. It is extremely arduous to model these components which could be very low energy gamma rays and unresolved scatters.

Various attempts were made to get data and MC to agree in terms of a spectral fit below 100 PE but it is clear that G4DS does not capture all the requirements. Even minor changes in the geometric description in G4DS could lead to the production of different S1 spectra.

In order to avoid this scenario, the idea of using tight fiducial cuts was employed. In particular the following cuts were used :

- Radius < 11 cm
- $180 \mu s < t_{drift} < 220 \mu s$

This produced reasonable agreement between data and MC. The main idea behind the cuts is that, at the very core of the detector the two major components contributing to the

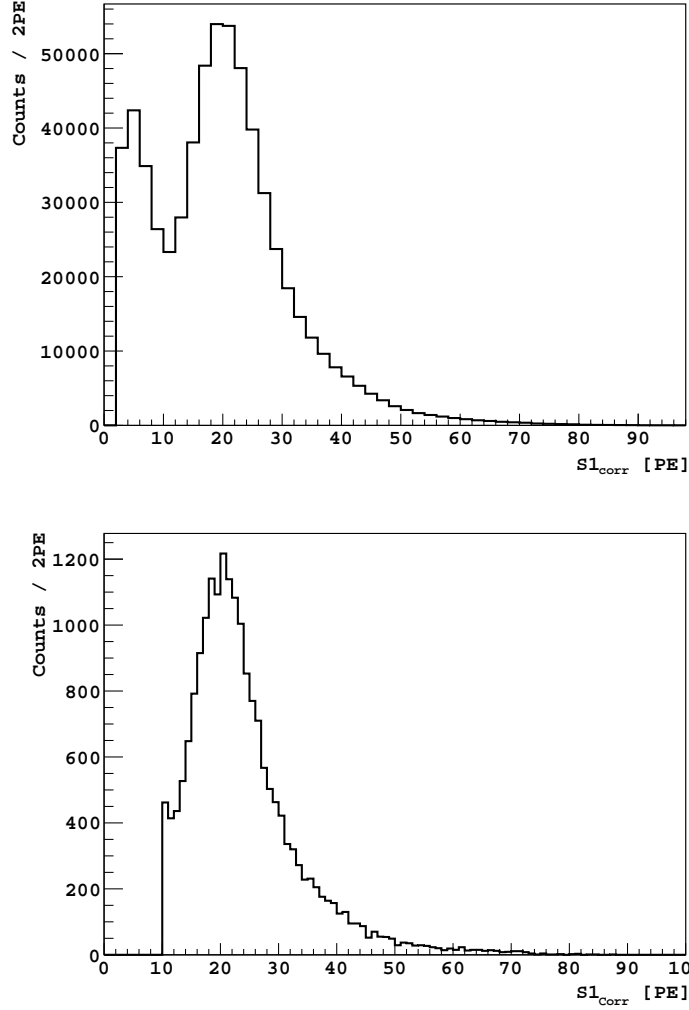


Figure 6.6: (top) Full axion S1 spectrum where the events leading to no light detection have been removed, and (bottom) spectrum used for fitting (events < 10 PE have been removed.)

background, should be the radioactivity inherent in the LAr, ^{39}Ar and ^{85}Kr . These have been produced using the technique described in Section 5.2.2.1.

6.3.3 Spectral Fitting

The spectral fitting procedure is similar to the one followed for the search for neutrino-less double electron capture on ^{36}Ar . The difference is that here one deals with the two dimensional spectrum of S1 and tdrift and not the $S1_{late}$ variable since the axion spectrum

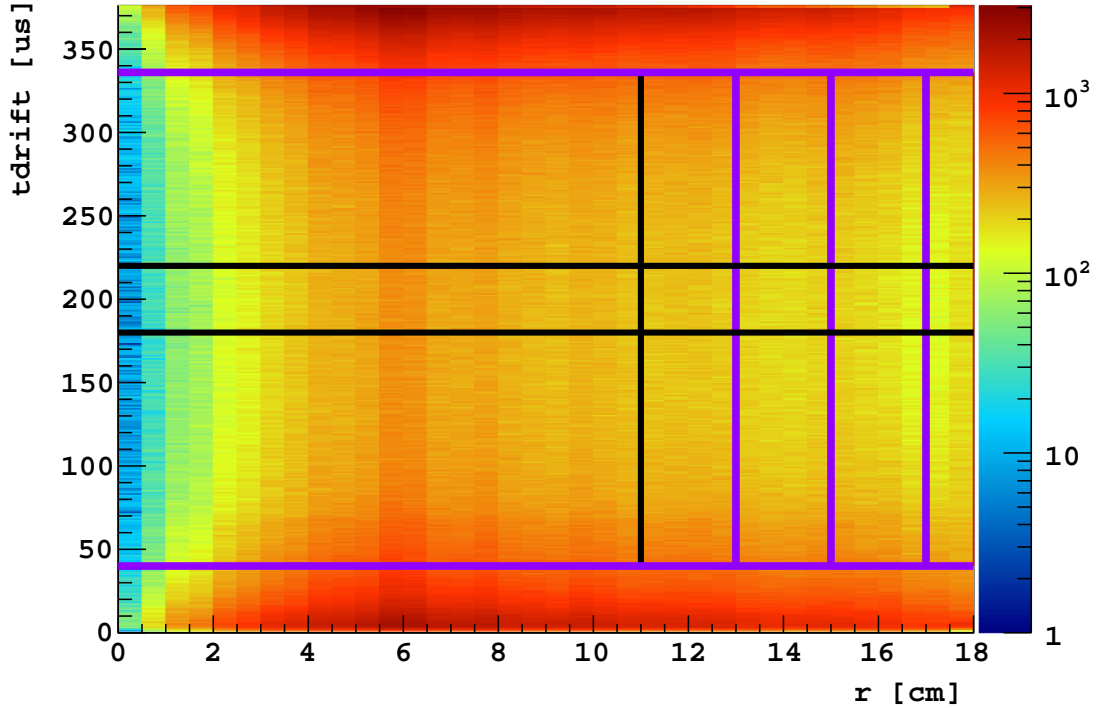


Figure 6.7: Fiducial cuts in $tdrift$ and xy direction indicated by the horizontal and vertical lines respectively for the 500 day dataset with basic cuts applied. The area contained between the two horizontal black lines ($180 < tdrift < 220$) and to the left of the vertical black line ($R < 11$ cm) was chosen as the final set of fiducial cuts to search for solar axions. The extreme upper and lower horizontal purple lines indicate the standard DS-50 $tdrift$ cuts. The colour scale represents the event count.

does not extend beyond 100 PE and there are no issues with saturation of the ADC. The fit is then performed in the range of (10,90) PE. It is assumed that the trigger efficiency above 10 PE is 100%. The activity of ^{85}Kr was constrained using a Gaussian distribution centred at the value measured from data using the analysis described in [57]. The results of the fit can be seen in Figure 6.8.

6.3.4 Preliminary Results

As done in Section 5.2.3, the sensitivity of DS-50 to identify the coupling constant is extracted in the same way.

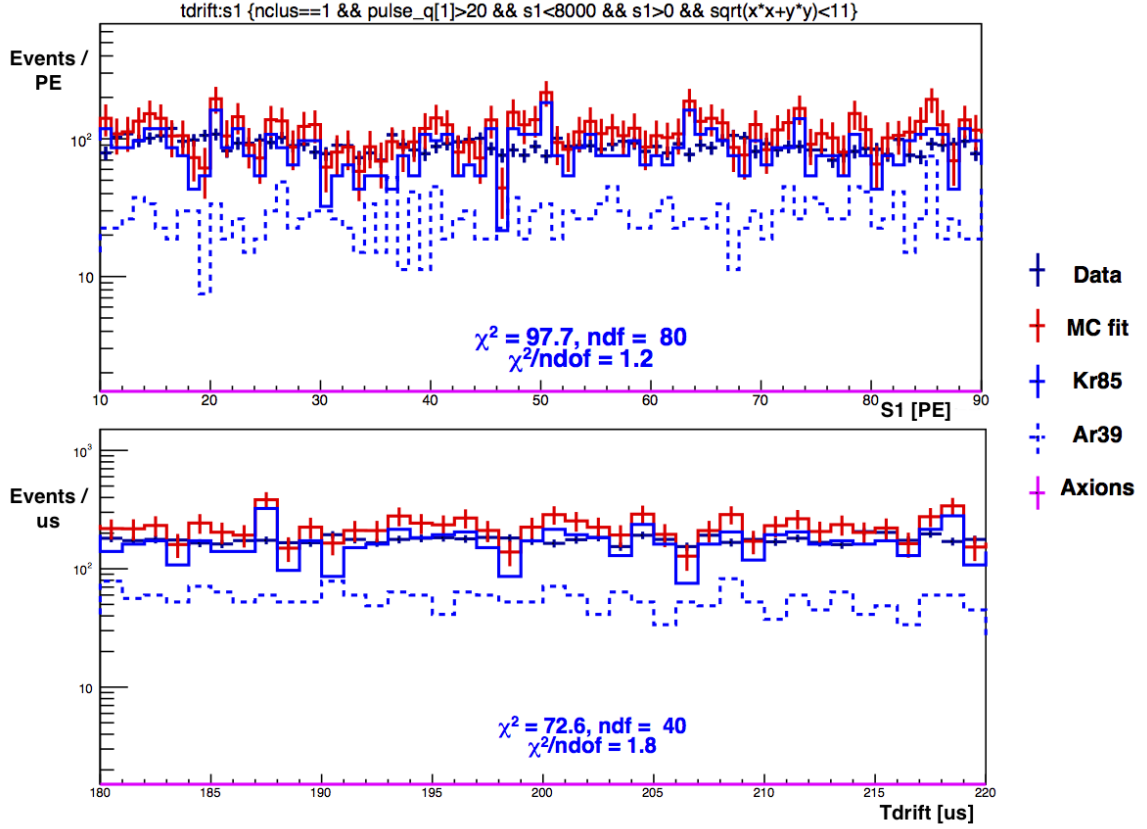


Figure 6.8: Simultaneous best fit spectrum in S1 and tdrift for single scatter events in the energy range of (10, 90) PE where the bulk of the axion spectrum above threshold can be observed. The best fit, without taking into account systematic uncertainties or overall normalization of event count, returns 0 axion events.

First, the following equation is formulated :

$$N = R \times A \times m \times T \times g_{Ae}^4 \times 10^{44} \quad (6.6)$$

Here N is number of events extracted from the “fit”; R is the calculated rate of axions interacting in a LAr volume given the solar axion flux; A is the acceptance of axion events in the fiducial volume; M is the fiducial mass of the detector used for the search; T is the livetime on which the analysis is carried out; and g_{Ae} is the coupling constant between axions and electrons. Since the calculation of the theoretical rate was done using a nominal value of the coupling $g_{Ae} = 10^{-11}$, a re-scaling is needed which is done by multiplying by the inverse of the fourth-power of this nominal coupling value which is 10^{44}

We know the following quantities :

- $T \approx 432$ days
- $A \approx 4\%$
- $M \approx 2.2$ kg
- $R \approx 2.5 \times 10^{-7} \text{ kg}^{-1} \text{ s}^{-1}$

Substituting these back into equation 6.3.4, the following equation is obtained which describes the limit on the coupling constant as a function of the number of events extracted from the procedure described above.

$$g_{Ae} \leq \left[\frac{N \times 10^{-44}}{R \times A \times M \times T} \right]^{0.25} \quad (6.7)$$

$$\implies g_{Ae} \leq N^{0.25} \times 1.22 \times 10^{-11}$$

To find the value of N, equation 5.2.3 can be invoked again :

$$\Delta\chi^2(N) \equiv \sum_{i=\text{min-bin}}^{\text{max-bin}} \frac{[h_{\text{background}}(i) - h_{\text{artificial}}(i, N)]^2}{h_{\text{background}}(i)} \quad (6.8)$$

From the fit, as seen in Figure 6.9, the value for N turns out to be 44 events. When substituted back into equation 6.3.4, a preliminary limit on the coupling constant is found to be:

$$g_{Ae} \leq 3.13 \times 10^{-11} \quad (6.9)$$

6.3.5 Uncertainties

Statistical uncertainties on the upper limit of the axio-electric coupling constant (g_{Ae}) were already folded in to the $\Delta\chi^2$ calculation. For the fitting procedure, the statistical

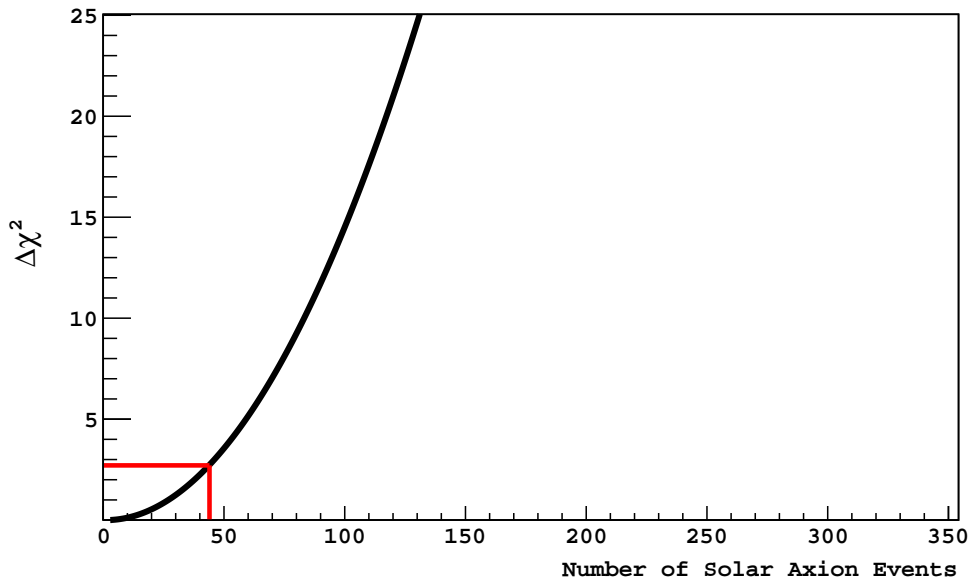


Figure 6.9: The change in χ^2 as a function of the addition of solar axion events. The horizontal red line indicates on the y-axis a change in χ^2 corresponding to 2.71 while the vertical red line indicates the number of events 44 that were required to induce this change.

uncertainties arising from the MC generated spectra were added in quadrature to the uncertainties arising from data. A simultaneous two-dimensional fit returns a reasonable p-value. Systematic uncertainties arising from the generation of MC spectra are extremely hard to estimate, and it is known that G4DS cannot capture the entirety of the micro-physics of the DS-50 detector. Some checks, as prescribed by [166] were made and fits were re-performed, but indicated that the tuning of G4DS parameters was already optimal. Further, a variation of the light yield by $\pm 3\%$ produced significantly worse fits which suggested that the empirical function describing the light yield described the data well. Systematic uncertainties on the coupling constant can arise from uncertainties in any of the quantities that fall in equation 6.3.4. A 10% relative and uncorrelated individual variation of any of these quantities (fiducial mass, acceptance or livetime) has a relative effect of $< 5\%$ on the coupling constant. Further systematic uncertainties arising from the determination of the shape of ^{39}Ar have not been investigated.

6.4 S2-Based Search

While a search for axions based on S1 is possible, the resolution in energy scale is much lower compared to the resolution available on an S2-only based search. Furthermore, inclusion of the various systematic uncertainties on the result in the previous section would lead to significantly less restrictive constraints. Hence, an analysis based on the S2-signal becomes a necessity. Such a search would follow most aspects of the analysis developed in [153] which is discussed briefly in Section 4.5.

6.4.1 Backgrounds

The backgrounds in such a search are the same as those arising in the search for sub-GeV dark matter particles scattering off electrons in LAr (discussed in Section 4.5). These consist of γ rays emitted from the cryostat or the PMT arrays. Moreover there is a significant contribution from the internal components which are primarily ^{39}Ar and ^{85}Kr .

6.4.2 The Electron Recoil Energy Scale

The electron recoil energy scale was initially developed in [153]. Subsequent tuning and re-modeling was performed, primarily by D.Franco [187], which heavily relies on the Thomas-Imel model [85].

The scale is based on the Doke energy variable which has been extensively discussed in [119] in the context of DS-50. Briefly, the energy deposited (E) in an event can be represented as a sum of two components (scintillation and ionization) as such

$$E = W \left(\frac{S1}{\varepsilon_1} + \frac{S2}{\varepsilon_2} \right) \quad (6.10)$$

where ε_1 is the exciton gain measured in units of PE/exciton while ε_2 is the charge gain

measured in units of PE/ e^- . W corresponds to the average energy required to produce an ion pair or an exciton. For LAr this has been measured to be ~ 19.5 eV [83]. To build the electron recoil energy scale, the data from ^{83m}Kr calibration is not used since the emission of two electrons induces a recombination effect which is not relevant to the calibration. The fit is made using the Doke points in the low-energy regime, with $\varepsilon_1 \sim 0.157$ PE/exciton and $\varepsilon_2 \sim 23$ PE/ e^- . Such a fit also provides good agreement from the two data points available from the emission of Auger electrons via K and L shell decay modes [188, 189]. The scale is shown in Figure 6.10.

The calculated axio-electric recoil spectrum is converted to the ionization spectrum measured in DS-50 using this scale conversion. The resulting ionization spectrum is then smeared assuming the ionization yield and recombination processes following a binomial distribution convolved with the detector response, measured from single electron events [132].

6.4.3 Profile Likelihood Fit

A binned profile likelihood fit is performed based on [137] via an implementation through the RooFit/RooStats [190] and HistFactory [191] packages following the procedure developed in [153]. It is worth describing the basic mechanism of the fit and corresponding test statistic by considering a simple example. The description here, follows that of [137].

Consider a simple experiment where each selected event measures the value of certain variables and subsequently the data can be represented by histograms. If for each event in the signal sample, a measurement of a variable x is made and a histogram \mathbf{n} is constructed such that $\mathbf{n} = (n_1, \dots, n_N)$ with the expectation value of the contents of the i -th bin given by $E[n_i] = \mu s_i + b_i$. Here the mean number of entries in the i -th bin from signal and

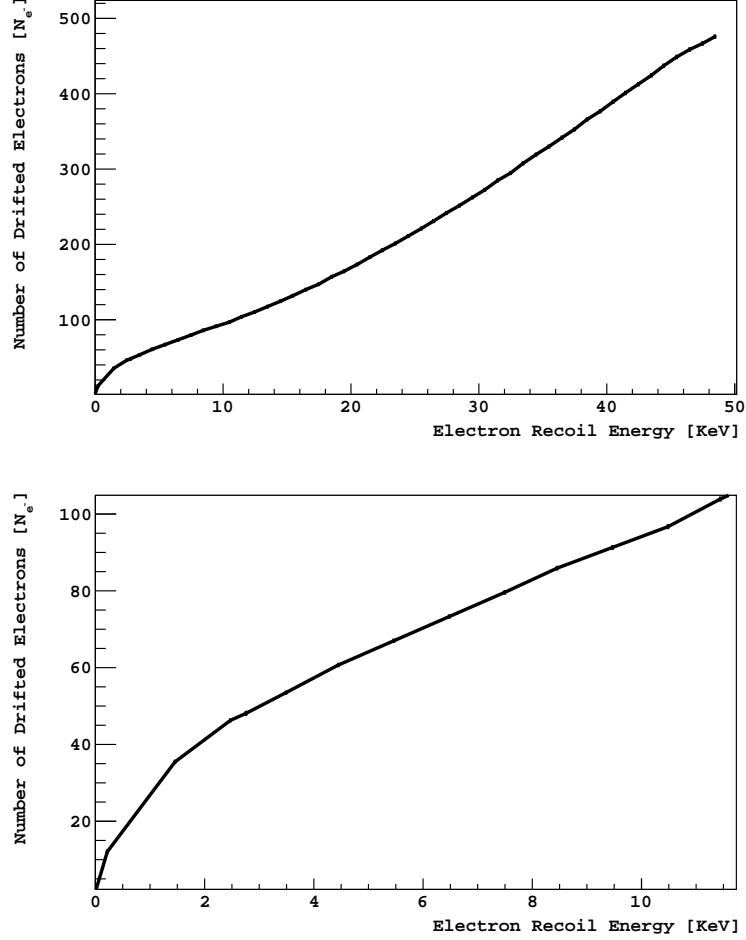


Figure 6.10: (top) The calibration curve used to convert electron recoil spectra to ionization spectra and (bottom) a zoomed-in version, relevant to generation of the axion spectrum.

background are :

$$s_i = s_{\text{tot}} \int_{\text{bini}} f_s(x; \theta_s) dx \quad (6.11)$$

$$b_i = b_{\text{tot}} \int_{\text{bini}} f_b(x; \theta_b) dx \quad (6.12)$$

respectively. The parameter μ defines the strength of the signal process with a value of 0 corresponding to a background-only hypothesis and the nominal value of 1 corresponding to the signal hypothesis. The probability density functions of the variable x are given by $f_S(x; \theta_s)$ and $f_b(x; \theta_b)$ for signal and background respectively. θ_s and θ_b represent parameters that characterize the shape of the pdfs. The terms b_{tot} and s_{tot} represent the mean

number of background and signal events, while the integrals determine the probabilities for an event to be found in the i -th bin. The nuisance parameters (parameters other than the parameter of interest) can be written as the vector $\theta = (\theta_s, \theta_b, b_{\text{tot}})$. Of course, the parameter of interest is the signal strength μ . Typically, additional measurements are made to further constrain the nuisance parameters. It is possible in some cases to select a sample of background only events and then further construct a histogram of the relevant variable as such $\mathbf{m} = (m_1, \dots, m_M)$. Thus the expectation value of the contents of the i -th bin is given by : $E[m_i] = u_i(\theta)$. Here u_i are the computable quantities which depend on the parameters θ . This construction is usually done to generate information on the background normalization parameter b_{tot} and perhaps even the signal and background shape parameters. Then, the likelihood function is the product of Poisson probabilities for all bins:

$$L(\mu, \theta) = \prod_{j=1}^N \frac{(\mu s_j + b_j)^{n_j}}{n_j!} e^{-(\mu s_j + b_j)} \prod_{k=1}^M \frac{u_k^{m_k}}{m_k!} e^{-u_k} \quad (6.13)$$

To be able to test a particular value of μ , the profile likelihood ratio defined by;

$$\lambda(\mu) = \frac{L(\mu, \hat{\theta})}{L(\hat{\mu}, \hat{\theta})} \quad (6.14)$$

is considered. The numerator is referred to as the profile likelihood function. $\hat{\theta}$ denotes the value of θ which maximizes the likelihood for the specifies value of μ . Thus it is also called the maximum-likelihood estimator of θ conditional on μ . The denominator, which is the unconditional likelihood function, is maximized. This implies that $\hat{\theta}$ and $\hat{\mu}$ are the maximum-likelihood estimators. The existence of nuisance parameters broadens the profile likelihood function (of μ). This reflects the loss of certainty on the measurement of μ , or the introduction of systematic uncertainties.

Using the definition of $\lambda(\mu)$ from 6.4.3, it is possible to interpret values of λ around 1 as reasonable agreement between data and the predicted value of μ . This can further be represented as the following test statistic :

$$t_\mu = -2 \ln \lambda(\mu) \quad (6.15)$$

Thus, lower values of t_μ correspond to agreement between data and the value of μ . It is further possible to compute the p-value to quantify this level of compatibility as:

$$p_\mu = \int_{t_{\mu,obs}}^{\infty} f(t_\mu|\mu) dt_\mu \quad (6.16)$$

where $t_{\mu,obs}$ represents the value of the test statistic observed from data and $f(t_\mu|\mu)$ represents the pdf of t_μ assuming a signal strength of μ .

Specifically to search for axions, an analysis threshold of $N_{e^-} = 4$, approximately equivalent to 0.01 keV_{ee}, is used. The background model used in the analysis is determined by a detailed MC simulation of the DS-50 setup. Spectral features at high energies are used to constrain the simulated radioactivity with the detector components to predict the background spectrum in the region of interest. During the analysis the overall normalization of the background model is constrained near its predicted value by a Gaussian nuisance term in the likelihood function. Additional Gaussian constraints on the background component are included based on the uncertainty of the fit and the uncertainty in the S2 to N_{e^-} conversion factor which is extracted from the single-electron data. An additional systematic uncertainty on the signal rate is set to account for uncertainties in the flux and cross section calculations. The fit is performed in the range of 4 and 100 drifted electrons. This range is chosen based on the fact that below 4 electrons the backgrounds are yet to be understood completely with ongoing work from DarkSide, while above 100 drifted electrons there is almost no contribution from the axion spectrum.

6.4.4 Preliminary Results

The results obtained from the best fit is shown in Figure 6.11. Further, Figure 6.12 shows the log-likelihood ratio as a two dimensional function of the cross section and the variance of the ionization yield. Figure 6.13 then shows the dependence log-likelihood ratio as a function of the cross section.

It is then possible to obtain from the log-likelihood ratio, the 90% Confidence Level

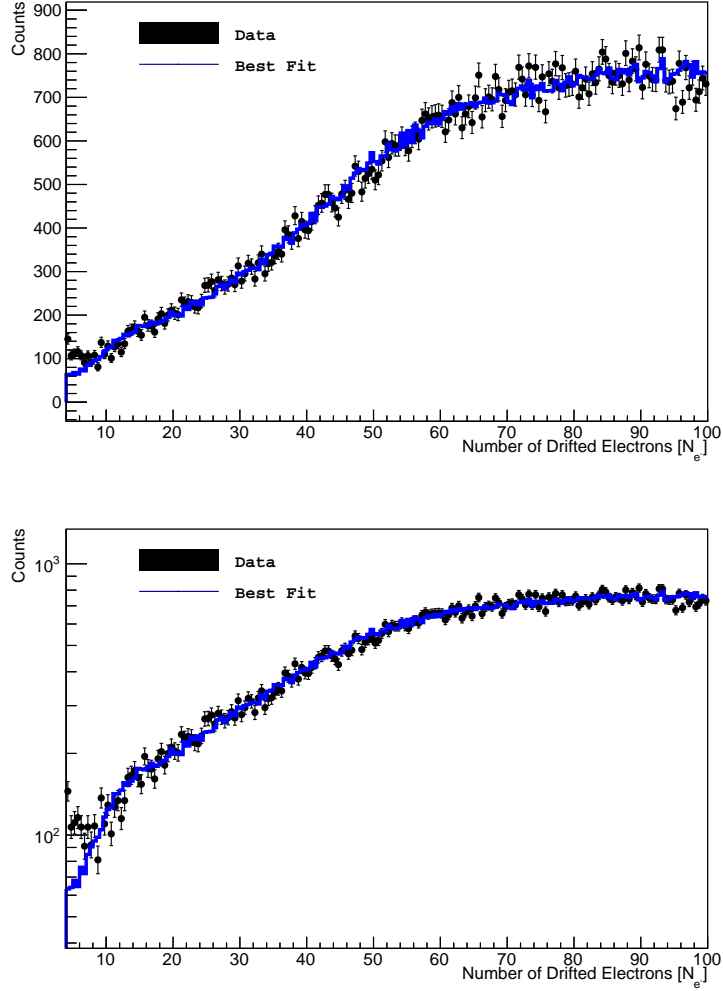


Figure 6.11: Best fit results, in linear (top) and logarithmic (bottom) scales.

limit on the cross section which can then further be translated to a limit on the coupling constant. The 90% CL on the cross section is found to be $4.26 \times 10^{-41} \text{ cm}^2$. The total axio-electric cross section, which was used to generate the input solar axion spectrum (with a nominal value of $g_{Ae} = 10^{-11}$) is $9.66 \times 10^{-44} \text{ cm}^2$. Hence to find the limit on the coupling constant (g_{Ae}), the following equation is used:

$$g_{Ae} \leq \left[\frac{4.26 \times 10^{-41} \text{ cm}^2}{9.66 \times 10^{-44} \text{ cm}^2} \right]^{0.25} \times 10^{-11} \quad (6.17)$$

$$\implies g_{Ae} \leq 4.6 \times 10^{-11} \quad (6.18)$$

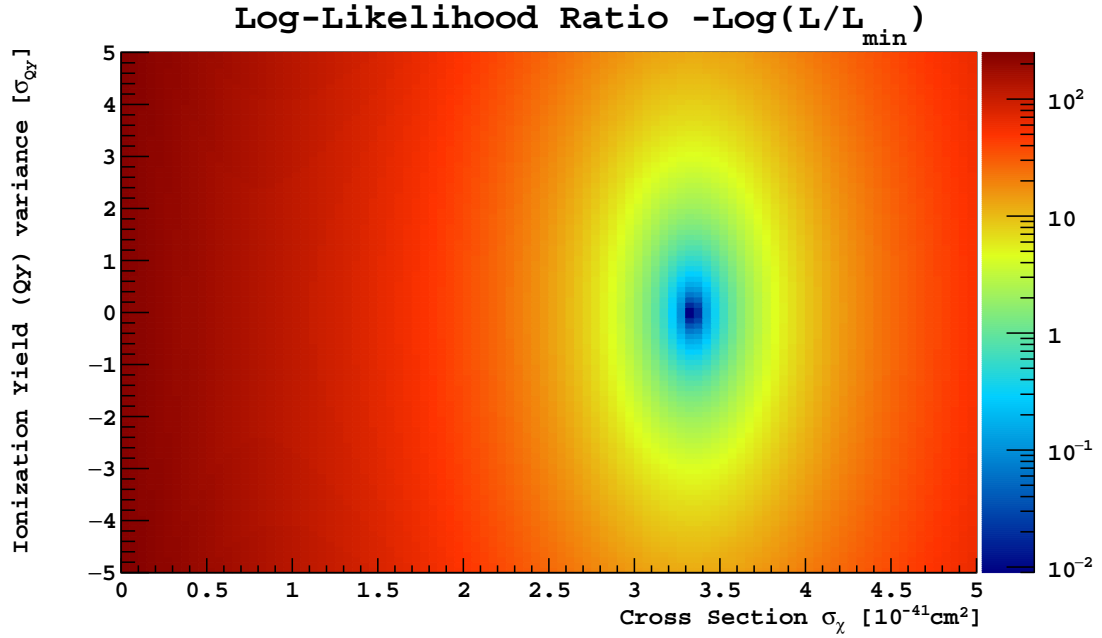


Figure 6.12: The Log-Likelihood ratio (depicted by the colour scale) shown as a function of the cross section and Ionization yield variance.

The result obtained here is approximately an order of magnitude higher than the constraint set by the LUX collaboration ($g_{Ae} \leq 3.5 \times 10^{-12}$) [192] and their results, among other experimental results are shown in Figure 6.14.

6.4.5 Possible Improvements

There is clearly some unexplained background at $4e^- \leq N_e \leq 7e^-$. Some of this may be explained by the tail of trapped electrons [132]. Moreover, there are improvements that are being made to the background model by D. Franco, P. Agnes and A. Navrer Agasson [193]. These include the possible addition of some new background components as well as accounting for the correct shape of the ^{39}Ar and ^{85}Kr β^- decay spectra, especially at low energies incorporating sub-atomic corrections, using the calculations provided in [194, 195].

Further, cryogenic distillation can be performed to reduce the ^{85}Kr background and a further suppression in the ^{39}Ar background is likely to be achieved in the next generation

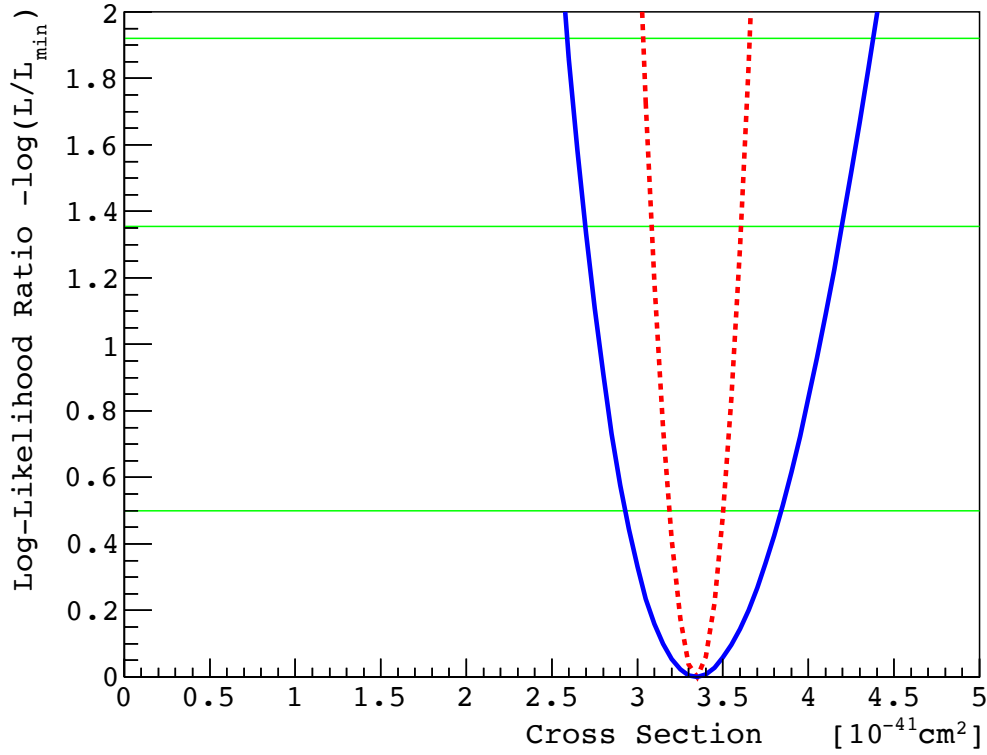


Figure 6.13: The log-likelihood ratio shown as a function of the parameter of interest which is the cross section scaled by the 4th power of the coupling constant. The red dashed line represents the likelihood ratio when the nuisance parameters are fixed at their minimum while the solid blue line represents the ratio when the nuisance parameters have been appropriately profiled. The three vertical lines represent from bottom to top represent the 68.27% , 90% and 95% Confidence Levels.

DarkSide detector [82]. But xenon has a higher photo-electric cross section than argon, and hence a higher axio-electric cross section, therefore argon-based experiments must have lower background rates than xenon-based ones to claim competitive limits.

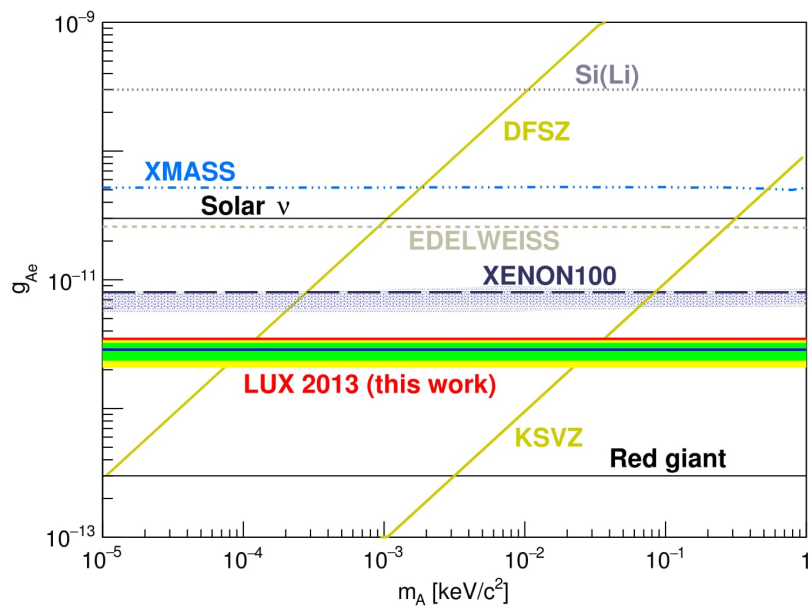


Figure 6.14: Various experimental constraints on the axio-electric coupling constant (g_{Ae} on the y-axis) shown as a function of axion mass (on the x-axis). Figure taken from [192].

Chapter 7

DarkSide : The Future

This chapter discusses the future of the DarkSide program and follows from the published technical design report of DS-20k [82] and the two most recent progress reports submitted to the LNGS scientific committee.

7.1 DarkSide-20k

The goal of DarkSide-20k [82] is to discover dark matter. It will build on the successful experience in operating DS-50. It will have an active mass of ~ 39 tonnes. DS-20k will have ultra-low backgrounds which can be measured in-situ.

7.1.1 Detector Overview

See Figure 7.1 for a schematic of the detector. The new concept is to host both the inner active detector vessel and the veto detector in a large LAr cryostat. The advantage would be that the inner vessel (containing UAr) would be immersed in a bath of LAr which would cancel hydro-static pressure and remove all thermal insulation requirements. This minimizes the amount of material required for the inner vessel and also reduces the amount

of radioactivity generated close to the sensitive volume. Most of the structural and possibly radioactive material will be situated at least 2 m away from the inner vessel. The conceptual design of the outer vessel is based on the experience obtained with the construction of similar vessels for the DUNE long baseline neutrino experiment [196, 197].

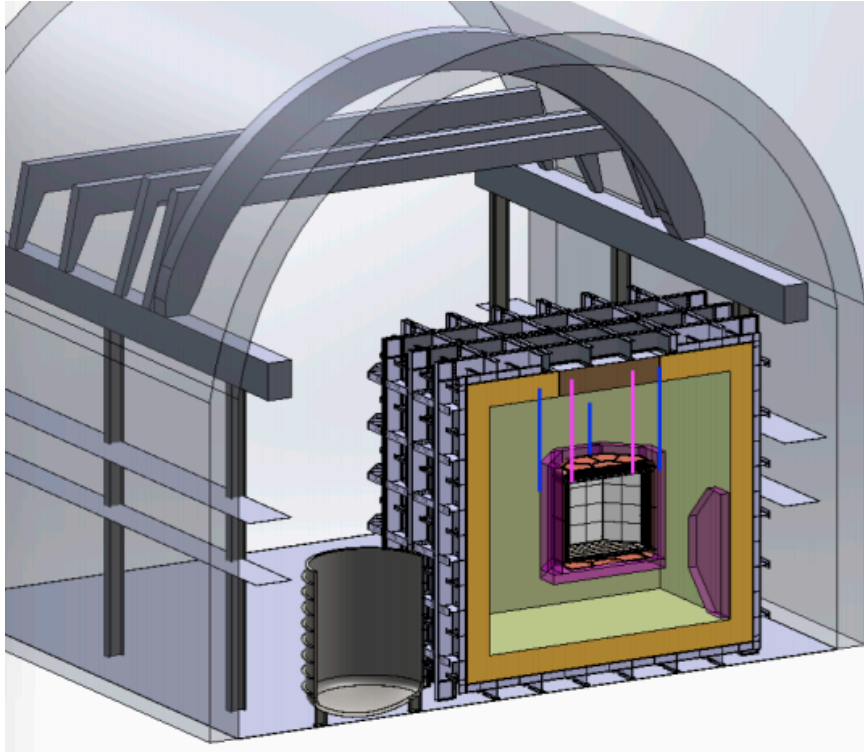


Figure 7.1: A 3D drawing of the DS-20K experiment. Figure taken from [198].

7.1.2 Backgrounds

The background sources are typically considered as internal or external. The former category consists primarily of radioactive contamination and neutrino interactions in the argon itself. External background refer to all other classes of backgrounds, arising from radioactive contamination of instruments, radioactive components and cosmogenic origin. The experience gained working with DS-50 will guide the background reduction of DS-20k. Electron recoil background are likely not to be a problem due to powerful discrimination power of

PSD. Radiogenic neutrons cannot be removed via PSD and the main source for these neutrons in DS-50 were the TPC PMTs. DS-20k will deploy SiPMs to readout scintillation light [199]. These SiPMs will be much more radio-pure than the PMTs previously used, while simultaneously providing better geometrical coverage, a higher quantum efficiency and a lower dark count. An irreducible background would arise from neutrino-induced coherent nuclear scattering. Atmospheric neutrinos and diffuse supernova neutrinos have sufficient energy to produce nuclear recoils in the WIMP search region. It is impossible to distinguish on an event-by-event basis, a coherent neutrino-nucleus scattering (CNNS) from a WIMP recoil. It is expected that 1.6 CNNS events would occur in a 100 tonne-year exposure for DS-20k. Even though this class of backgrounds is irreducible, it presents an opportunity to observe previously unseen phenomenon in LAr.

7.1.3 Underground Argon

The DarkSide collaboration has developed a strategy to increase the production of UAr to procure the requisite amount for DS-20k. The Urania project will extract more than 50 tonnes of UAr meeting the requirement of 47 tonnes for DarkSide-20k. The goal of the project is to construct a plant which is capable of extracting and purifying UAr at a high rate (up to 250 kg/day). The aim of the Aria project is to perform chemical purification of the UAr once it has been extracted by Urania. It will be done by employing a 300 m tall cryogenic distillation column. Aria can potentially further deplete the ^{39}Ar activity by a second column. The ultimate goal of the Aria project is to process ~ 150 kg/day of argon to achieve a further depletion factor between 10 and 100.

7.1.4 Sensitivity

Since WIMP interaction are expected to be extremely rare, it is essential to keep the instrumental background rate to less than 0.1 events for the total exposure. Figure 7.3

shows the number of WIMP-like events that need to be observed in order to reject the null hypothesis (background only) at the 5σ level as a function of the number of background events. DS-20k is expected to increase the current best sensitivity to $\sim 1.2 \times 10^{-47} \text{cm}^2$ for a WIMP of mass $1 \text{TeV}/c^2$ with an exposure of 100 ton-yr [82] (See Figure 7.2). Moreover limits on cross sections for low-mass WIMPs will also improve building on the techniques employed for DS-50.

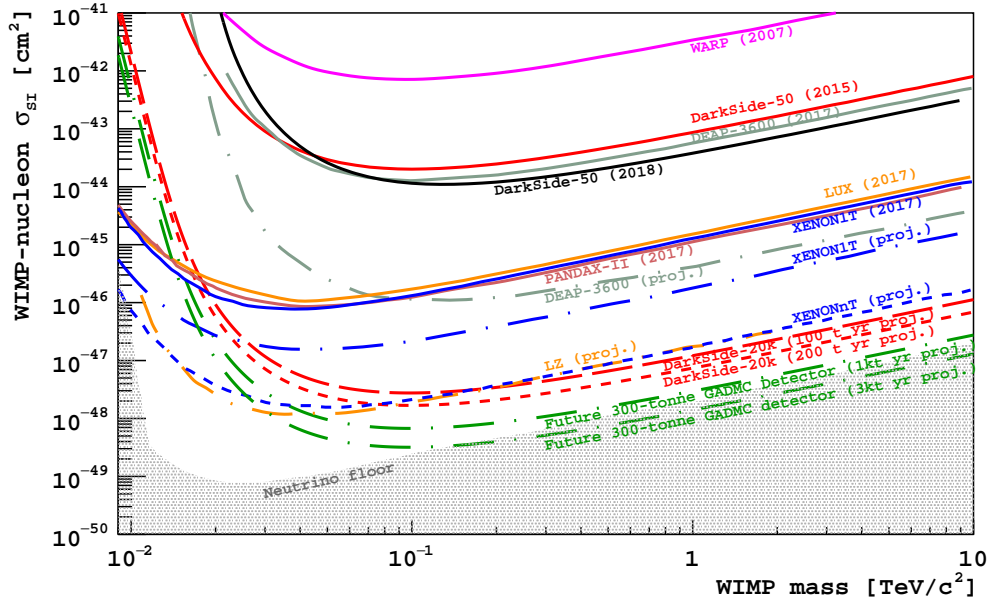


Figure 7.2: DM spin-independent cross-section vs. mass limits and sensitivities from previous argon-based results (including the DarkSide-50 532-live-day limit), current best limits produced by xenon-based experiments, and expected future sensitivities (dashed and/or dotted lines). The “neutrino floor” curve follows the definition of [200]. Figure taken from [82].

7.2 Cosmogenic Background Simulation

Since single elastic neutron scatters are indistinguishable from elastic WIMP scatters, background from all sources of neutrons must be reduced below the 0.1 events threshold. In order to determine the background arising from cosmogenic events, a FLUKA simulation was developed.

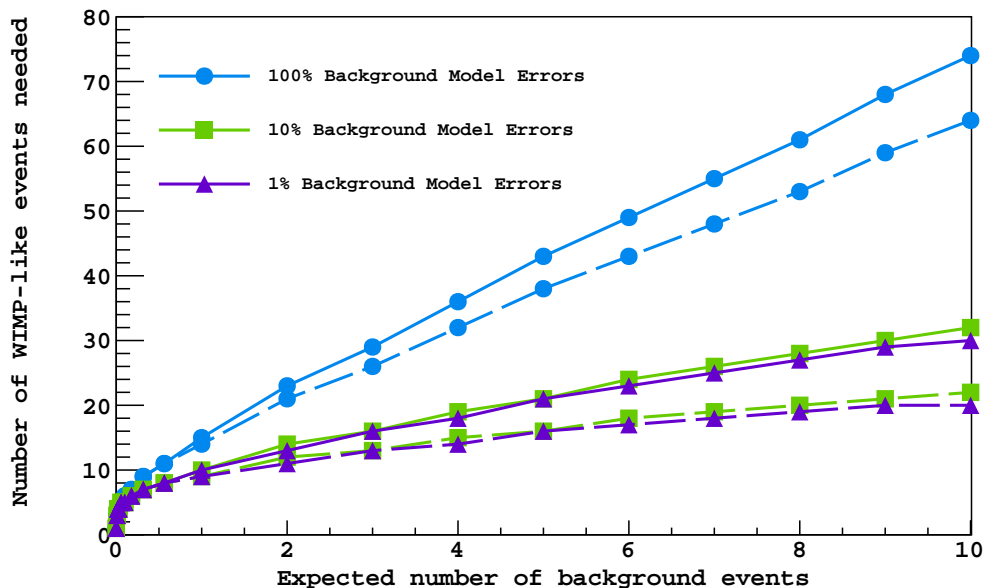


Figure 7.3: Number of dark matter-like events needed to claim a WIMP observation at the 5σ level, based on the predicted background rate of the experiment, in a linear-linear scale. Solid lines show the number of dark matter-like events needed, including backgrounds, while dashed lines show the number of dark matter events after subtraction of the expected background. Blue, green, and purple curves were made assuming uncertainty on the background model of 100%, 10%, and 1%, respectively. Figure taken from [82].

The geometry implemented in the simulation was based on the conceptual design of the experiment taken from [201]. The outer cryostat geometry was obtained from the CERN group responsible for the construction of the ProtoDUNE cryostat at CERN. The inner vessel was approximated by a series of cylindrical volumes (with their geometrical centers coinciding with the centre of the TPC) with approximately the right amount of material. It consists of the following (see Figure 7.4 for a visual of the implemented geometry):

- A cylindrical plastic shell with a height of 3.8 m and a radius of 2.05 m. The thickness of the scintillator was set at 30 cm. It was composed of acrylic.
- A cylindrical copper vessel with a height of 3.2 m and a radius of 1.75 m. The thickness was 1 cm.
- A cylindrical copper field cage with a height of 2.47 m and a radius of 1.46 m. The

thickness of which was 1 cm on the top and bottom and 5 mm on the sides.

- A cylindrical acrylic vessel with a height of 2.45 m and a radius of 1.455 m. The thickness of which was 2.5 cm above and below the TPC and 5 mm on the side.
- A cylindrical TPC with a height of 2.4 m and a radius of 1.45 m which contained ~ 22 tonnes of UAr.

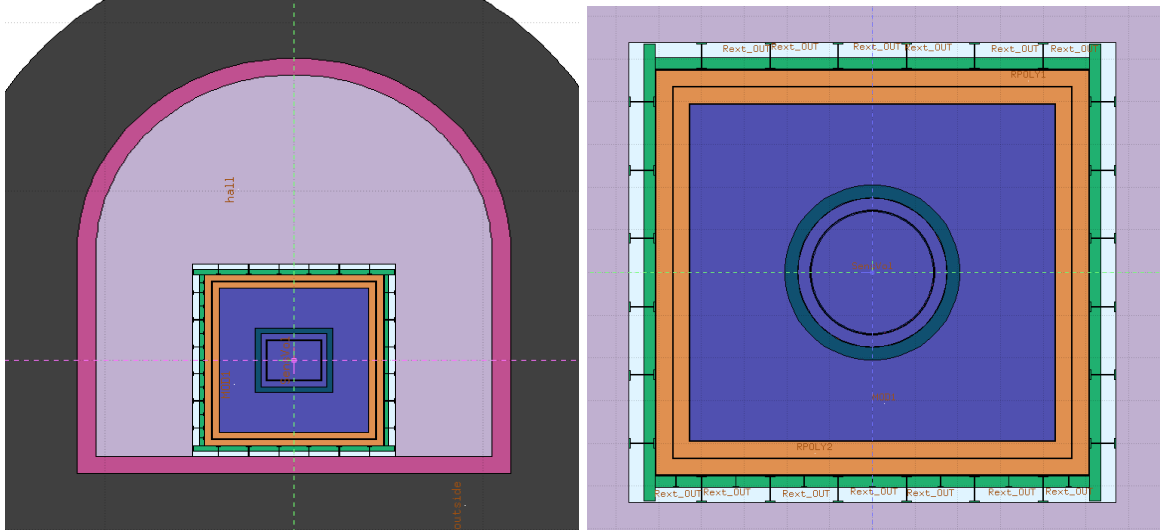


Figure 7.4: The conceptual design of DS20k implemented in FLUKA. (Left) The cross sectional view through Hall C. (Right) Cross sectional view through the bottom of the ProtoDUNE cryostat containing the TPC.

7.2.1 Prompt Background

The study to determine the background to DS-20k follows from that of Section 3.5 and again is based on [73, 108]

The latest datasets of cosmogenic events were prepared (by A. Empl) in context of the SABRE experiment [202]. These events were recorded on a cylindrical surface with 14 m diameter and 14 m height. This represents approximately the design of the Water Cherenkov Veto for the DS-20k baseline design [82].

The height of this virtual cylinder is sufficient to contain the entire protoDUNE [196]

based cryostat, however, in the horizontal direction, the corners of the cuboidal cryostat extend approximately 80 cm beyond the curved surface of the cylinder. For the current simulation then, all recorded particles were moved back along their trajectory to start the events from a cylindrical surface which completely encloses the cryostat.

The simulation is carried out in two technical steps. In the first step, the energy depositions in the outer LAr region and the plastic veto scintillator are recorded. All such particles which reach the outside of the sensitive volume (TPC) are frozen in place with their information written to an external file. In the second step of the FLUKA simulation, the particles which were previously frozen at the TPC are tracked further. Energy depositions from both steps are subsequently combined. In this fashion, it is possible to reject classes of events which are not of interest in order to focus on potentially critical events and further speed up the simulation. At this point, events are rejected if and only if they satisfy the following three conditions :

- There are more than 6 particles that reach the TPC
- The summed kinetic energy of the particles reaching the TPC is > 1 GeV
- There is a direct muon tracked as entering the sensitive LAr volume.

For the initial study of potential cosmogenic backgrounds, a subset of events was selected for which not more than two particles reached the TPC and at least one of these particles was a neutron. Without any further energy considerations, a total of 420 ± 2.5 events per year are predicted satisfying these constraints.

7.2.2 Results

The results are shown in Figure 7.5. The total livetime of the simulation is ≈ 194 years. There were no potential background events found. Therefore, a 90% CL upper limit on the cosmogenic background can be placed at $< 2.3/194 = 0.01$ events/year.

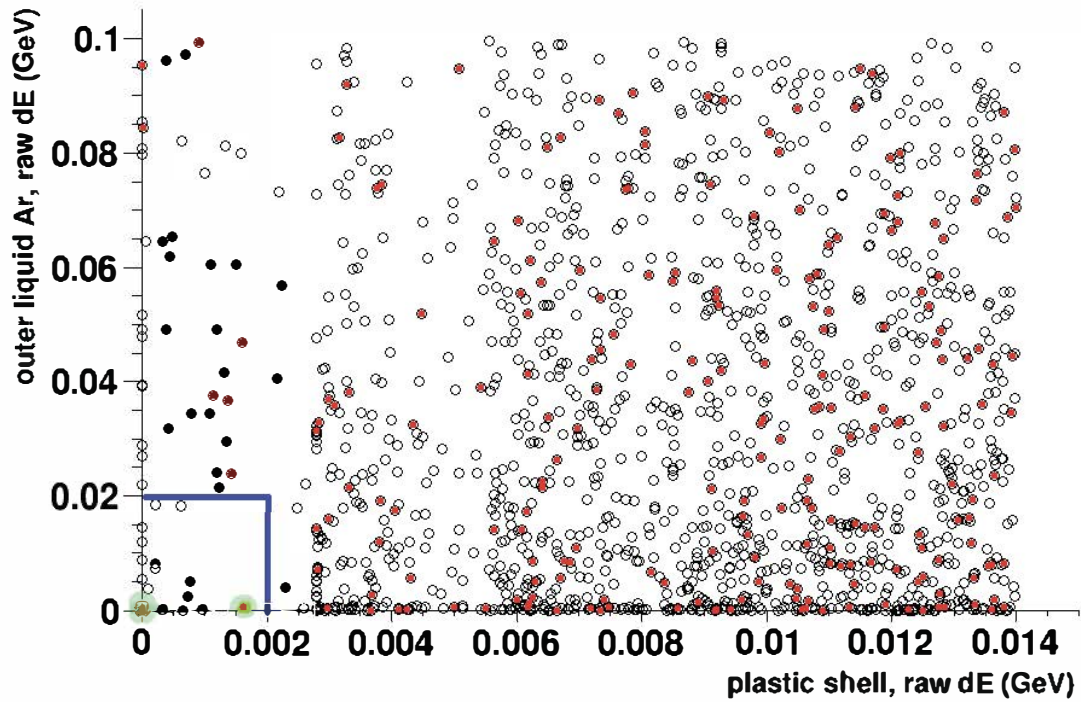


Figure 7.5: Two dimensional distribution of events with their energy deposit in the plastic scintillator on the x-axis and the energy deposit in the outer LAr volume on the y-axis. These are results for a simulated livetime of ~ 194 years. Red dots correspond to events that deposited non-zero but < 1 MeV in the sensitive volume. The blue lines correspond to the nominal cuts on the energy deposits in the outer detectors. The three highlighted events correspond to potentially critical events that could not be vetoed solely on the basis of energy deposits in the outer detectors. They are vetoed based on their multiple interactions inside the sensitive volume.

Chapter 8

Summary and Future Outlook

Astronomical observations have made it clear that a large fraction of the matter in the universe is dark. The nature of dark matter is yet unknown with a host of theories hoping to provide a description for what it is. To test various hypotheses, a large number of detectors exploiting different technologies have been developed in the last couple of decades.

One of the most well motivated candidates for particle dark matter are Weakly Interacting Massive Particles (WIMPs) and liquid noble gas detectors have recently demonstrated enormous progress in this research. Among LAr detectors, the DS-50 detector has led the search for high-mass WIMPs by utilizing argon from underground sources. DS-50 has successfully accumulated ≈ 1.7 years of livetime while operating in a background-free mode.

In Section 2.3, I summarized the procedure to calibrate the single photoelectron response of the TPC PMTs, which was revisited and improved to reduce uncertainty.

The DarkSide collaboration was able to demonstrate the results of a background-free blind analysis performed on 532 live-days of collected WIMP search data. Section 4.3 summarizes this result.

In order to suppress backgrounds, a veto strategy (summarized in Chapter 2) was developed by the DarkSide collaboration. This veto system was used to identify cosmogenic events among other classes of background. I evaluated the efficiency of the veto system to reject cosmogenic background using a Monte-Carlo simulation developed for DS-50. Moreover, I made a prediction for the number of cosmogenic neutrons potentially creating WIMP-like signals for the 532-day blind analysis with this MC, which was detailed in 3.5.

DS-50 has also set the world's most sensitive limit for low-mass WIMP-nucleon spin-independent scattering, spanning masses in the range of 1.8 and 6.0 GeV/ c^2 . At the same time, it has set the most sensitive limit for WIMP-electron scattering for WIMP masses in the range of 30 to 50 MeV/ c^2 . This was mentioned in Chapter 4.

Chapter 7 discusses the plans of the DarkSide collaboration to build the DS-20k detector which will have a fiducial mass 400 times that of DS-50. It will also have lower instrumental and internal backgrounds by utilizing SiPMs (instead of PMTs) and purification of the argon via the Urania and Aria projects.

Furthermore, a new veto concept allows the relocation of a large fraction of the radioactive material to distances greater than 2 m from the sensitive volume. I evaluated, via MC, the efficiency of the DS-20k veto system to reject cosmogenic neutrons, which may mimic WIMP signals. I discussed this in Section 7.2.

While DarkSide has demonstrated detector technology that is sensitive to WIMPs, In Chapters 5 and 6, I indicated that other rare event searches such as neutrino-less double electron capture (0ν ECEC) and axion-electron scattering, could be performed using the same detector. This was made possible due to its high quality, low-background and stable operation in the last few years, and especially due the use of UAr. These searches could lead to the discovery of yet unobserved phenomena, expanding the horizon of particle physics.

I analyzed data to look for signals of such interactions, but no evidence for the signals was found. Hence, a lower limit was placed on the half-life of the 0ν ECEC on ^{36}Ar at

$T_{1/2} > 1.3 \times 10^{17}$ years (Section 5.2.2). Similarly, an upper limit was placed on the coupling constant associated with the interaction of axions and electrons at $g_{Ae} < 4.6 \times 10^{-11}$ (Section 6.4).

With further research and developments leading to improvements in background-reduction techniques, it may be possible to find answers to some open problems in particle physics and cosmology.

Bibliography

- [1] F. Zwicky. Die Rotverschiebung von extragalaktischen Nebeln. *Helvetica Physica Acta*, 6:110–127, 1933.
- [2] Vera C. Rubin. Dark matter in spiral galaxies. *Scientific American*, 248(6):96–109, 1983.
- [3] T. S. van Albada, J. N. Bahcall, K. Begeman, and R. Sancisi. Distribution of dark matter in the spiral galaxy NGC 3198. *The Astrophysical Journal*, 295:305–313, August 1985.
- [4] D. Coe. Dark Matter Halo Mass Profiles. *arXiv:1005.0411*, May 2010.
- [5] J. F. Navarro, C. S. Frenk, and S. D. M. White. The Structure of Cold Dark Matter Halos. *The Astrophysical Journal*, 462:563, May 1996.
- [6] NASA, ESA, and J. Richard, Abell 2218, (2008). <https://www.spacetelescope.org/images/heic0814a/>. Accessed: 2018-10-01.
- [7] Douglas Clowe, Marusac Bradac, Anthony H. Gonzalez, Maxim Markevitch, Scott W. Randall, Christine Jones, and Dennis Zaritsky. A direct empirical proof of the existence of dark matter. *The Astrophysical Journal Letters*, 648(2):L109, 2006.
- [8] X-ray: NASA Markevitch et al. ; Lensing map: NASA D.Clowe et al. ; Optical: NASA; D.Clowe et al. <https://apod.nasa.gov/apod/ap170115.html>. Accessed: 2018-10-01.
- [9] M. Arnaud, M. and et al.. Planck 2013 results. I. Overview of products and scientific results. *Journal of Astronomy and Astrophysics*, 571:A1, November 2014.
- [10] Michael S. Turner and J. Anthony Tyson. Cosmology at the millennium. *Rev. Mod. Phys.*, 71:S145–S164, Mar 1999.
- [11] A. H. Guth. Inflationary universe: A possible solution to the horizon and flatness problems. *Phys. Rev. D.*, 23:347–356, January 1981.
- [12] W. Rindler. Visual horizons in world models. *MNRAS*, 116:662, 1956.
- [13] S. Hawking and W. Israel. *General Relativity: an Einstein Centenary Survey*. March 2010.

- [14] D. J. Fixsen. The temperature of the cosmic microwave background. *The Astrophysical Journal*, 707(2):916, 2009.
- [15] C. L. Bennett et al. Nine-year Wilkinson Microwave Anisotropy Probe (WMAP) observations: Final maps and results. *The Astrophysical Journal Supplement Series*, 208(2):20, 2013.
- [16] Gerard Jungman, Marc Kamionkowski, and Kim Griest. Supersymmetric dark matter. *Physics Reports*, 267(5):195 – 373, 1996.
- [17] Jonathan L. Feng. Dark Matter Candidates from Particle Physics and Methods of Detection. *Ann. Rev. Astron. Astrophys.*, 48:495–545, 2010.
- [18] Scott Dodelson and Lawrence M. Widrow. Sterile neutrinos as dark matter. *Phys. Rev. Lett.*, 72:17–20, Jan 1994.
- [19] Andrea Albert. Observational and theoretical motivation for particle dark matter. In *Searching for Dark Matter with Cosmic Gamma Rays*, 2053-2571, pages 2–1 to 2–15. Morgan Claypool Publishers, 2016.
- [20] M. Milgrom. A modification of the Newtonian dynamics as a possible alternative to the hidden mass hypothesis. *The Astrophysics Journal*, 270:365–370, July 1983.
- [21] Erik Verlinde. Emergent Gravity and the Dark Universe. *SciPost Phys.*, 2(3):016, 2017.
- [22] Erik Verlinde. On the origin of gravity and the laws of Newton. *Journal of High Energy Physics*, 2011(4):29, Apr 2011.
- [23] J. D. Lewin and P. F. Smith. Review of mathematics, numerical factors, and corrections for dark matter experiments based on elastic nuclear recoil. *Astropart. Phys.*, 6:87–112, 1996.
- [24] Sunil Golwala. *Exclusion Limits on the WIMP-Nucleon Elastic-Scattering Cross Section from the Cryogenic Dark Matter Search*. PhD thesis, UC Berkeley, 2000.
- [25] V Chepel and H Arajo. Liquid noble gas detectors for low energy particle physics. *Journal of Instrumentation*, 8(04):R04001, 2013.
- [26] C. Patrignani et al. Review of Particle Physics. *Chin. Phys.*, C40(10):100001, 2016.
- [27] S. Fukuda et al. The Super-Kamiokande detector. *Nuclear Instruments and Methods in Physics Research Section A: Accelerators, Spectrometers, Detectors and Associated Equipment*, 501(2):418 – 462, 2003.
- [28] J Ahrens et al. Sensitivity of the IceCube detector to astrophysical sources of high energy muon neutrinos. *Astroparticle Physics*, 20(5):507 – 532, 2004.
- [29] V. Bonvicini et al. The PAMELA experiment in space. *Nuclear Instruments and Methods in Physics Research Section A: Accelerators, Spectrometers, Detectors and Associated Equipment*, 461(1):262 – 268, 2001. 8th Pisa Meeting on Advanced Detectors.

- [30] Jorge Casaus. The AMS-02 experiment on the ISS. *Journal of Physics: Conference Series*, 171(1):012045, 2009.
- [31] Jan Conrad. Indirect Detection of WIMP Dark Matter: a compact review. In *Interplay between Particle and Astroparticle physics (IPA2014) London, United Kingdom, August 18-22, 2014*, 2014.
- [32] P. A. Amaudruz et al. First results from the DEAP-3600 dark matter search with argon at SNOLAB. *Phys. Rev. Lett.*, 121(7):071801, 2018.
- [33] Mark Boulay, Bei Cai, and the DEAP/CLEAN Collaboration. Dark matter search at SNOLAB with DEAP-1 and DEAP/CLEAN-3600. *Journal of Physics: Conference Series*, 136(4):042081, 2008.
- [34] G.J. Alner et al. First limits on WIMP nuclear recoil signals in ZEPLIN-II: A two-phase xenon detector for dark matter detection. *Astroparticle Physics*, 28(3):287 – 302, 2007.
- [35] P. Agnes et al. First results from the DarkSide-50 dark matter experiment at Laboratori Nazionali del Gran Sasso. *Physics Letters, Section B: Nuclear, Elementary Particle and High-Energy Physics*, 2015.
- [36] J. Angle et al. First results from the XENON10 dark matter experiment at the Gran Sasso National Laboratory. *Phys. Rev. Lett.*, 100:021303, Jan 2008.
- [37] D. S. Akerib et al. Improved limits on scattering of weakly interacting massive particles from reanalysis of 2013 LUX data. *Phys. Rev. Lett.*, 116:161301, Apr 2016.
- [38] The CDMS-II Collaboration. Dark matter search results from the CDMS-II experiment. *Science*, 2010.
- [39] A Benoit et al. Improved exclusion limits from the EDELWEISS WIMP search. *Physics Letters B*, 545(1):43 – 49, 2002.
- [40] M. Bravin et al. The CRESST dark matter search. *Astropart. Phys.*, 12:107–114, 1999.
- [41] N. Boukhira, I. Boussaroque, M. DiMarco, R. Gornea, C. Leroy, L. Lessard, J.-P. Martin, and V. Zacek. Search for dark matter with the picasso experiment. *Nuclear Physics B - Proceedings Supplements*, 110:103 – 105, 2002.
- [42] E. Behnke et al. First dark matter search results from a 4-kg CF₃I bubble chamber operated in a deep underground site. *Phys. Rev. D*, 86:052001, Sep 2012.
- [43] R. Bernabei et al. Final model independent results of DAMA/LIBRA-phase1 and perspectives of phase2. *Physics of Particles and Nuclei*, 46(2):138–146, Mar 2015.
- [44] J. H. Davis. Fitting the annual modulation in DAMA with neutrons from muons and neutrinos. *Phys. Rev. Lett.*, 113:081302, Aug 2014.
- [45] E. Aprile et al. Dark Matter Search Results from a one tonne×year Exposure of XENON1T. *Phys. Rev. Lett.*, 121(11):111302, 2018.

- [46] D. M. Mei, Z. B. Yin, L. C. Stonehill, and A. Hime. A model of nuclear recoil scintillation efficiency in noble liquids. *Astroparticle Physics*, 30(1):12–17, 2008.
- [47] Tadayoshi Doke et al. Absolute scintillation yields in liquid argon and xenon for various particles. *Japanese Journal of Applied Physics, Part 1: Regular Papers and Short Notes and Review Papers*, 41(3 A):1538–1545, 2002.
- [48] J. Lindhard, V. Nielsen, M. Scharff, and P.V. Thomsen. Integral equations governing radiation effects. (notes on atomic collisions, iii). *Kgl. Danske Videnskab., Selskab. Mat. Fys. Medd.*
- [49] H. O. Back et al. First Large Scale Production of Low Radioactivity Argon From Underground Sources. *arXiv:1204.6024*, April 2012.
- [50] H. O. Back et al. First Commissioning of a Cryogenic Distillation Column for Low Radioactivity Underground Argon. *arXiv:1204.6061*, April 2012.
- [51] P. Agnes et al. Results from the first use of low radioactivity argon in a dark matter search. *Physical Review D*, 93(8):081101, 2016.
- [52] E.H. Bellamy et al. Absolute calibration and monitoring of a spectrometric channel using a photomultiplier. *Nuclear Instruments and Methods in Physics Research Section A: Accelerators, Spectrometers, Detectors and Associated Equipment*, 339(3):468 – 476, 1994.
- [53] R. Dossi, A. Ianni, G. Ranucci, and O.Ju. Smirnov. Methods for precise photoelectron counting with photomultipliers. *Nuclear Instruments and Methods in Physics Research Section A: Accelerators, Spectrometers, Detectors and Associated Equipment*, 451(3):623 – 637, 2000.
- [54] I. Chirikov-Zorin, I. Fedorko, A. Menzione, M. Pikna, I. Skora, and S. Tokr. Method for precise analysis of the metal package photomultiplier single photoelectron spectra. *Nuclear Instruments and Methods in Physics Research Section A: Accelerators, Spectrometers, Detectors and Associated Equipment*, 456(3):310 – 324, 2001.
- [55] R. Saldanha, L. Grandi, Y. Guardincerri, and T. Wester. Model independent approach to the single photoelectron calibration of photomultiplier tubes. *Nuclear Instruments and Methods in Physics Research Section A: Accelerators, Spectrometers, Detectors and Associated Equipment*, 863:35 – 46, 2017.
- [56] C. Green, J. Kowalkowski, M. Paterno, M. Fischler, L. Garren, and Q. Lu. The Art Framework. *J. Phys. Conf. Ser.*, 396:022020, 2012.
- [57] Alden Fan. *Results from the DarkSide-50 Dark Matter Experiment*. PhD thesis, UCLA, May 2016.
- [58] P. Agnes et al. The veto system of the DarkSide-50 experiment. *Journal of Instrumentation*, 11(3), 2016.
- [59] I. Berلمان. *Handbook of fluorescence spectra of Aromatic Molecules*. Elsevier Science, 2012.

- [60] Alex Wright, Pablo Mosteiro, Ben Loer, and Frank Calaprice. A highly efficient neutron veto for dark matter experiments. *Nuclear Instruments and Methods in Physics Research Section A: Accelerators, Spectrometers, Detectors and Associated Equipment*, 644(1):18 – 26, 2011.
- [61] M.B. Chadwick et al.. ENDF/B-VII.1 nuclear data for science and technology: Cross sections, covariances, fission product yields and decay data. *Nuclear Data Sheets*, 112(12):2887 – 2996, 2011. Special Issue on ENDF/B-VII.1 Library.
- [62] M. Chen et al. Quenching of undesired fluorescence in a liquid scintillator particle detector. *Nuclear Instruments and Methods in Physics Research Section A: Accelerators, Spectrometers, Detectors and Associated Equipment*, 420(1):189 – 201, 1999.
- [63] F. Elisei et al. Measurements of liquid scintillator properties for the borexino detector. *Nuclear Instruments and Methods in Physics Research Section A: Accelerators, Spectrometers, Detectors and Associated Equipment*, 400(1):53 – 68, 1997.
- [64] S. Westerdale, E. Shields, and F. Calaprice. A prototype neutron veto for dark matter detectors. *Astroparticle Physics*, 79:10 – 22, 2016.
- [65] E. K. Shields. *SABRE: A search for dark matter and a test of the DAMA/LIBRA annual-modulation result using thallium-doped sodium-iodide scintillation detectors*. PhD thesis, Princeton University, 2015.
- [66] Shawn Westerdale. *A Study of Nuclear Recoil Backgrounds in Dark Matter Detectors*. PhD thesis, Princeton University, May 2016.
- [67] Hamamatsu Corporation. Large photocathode area photomultiplier tubes. https://www.hamamatsu.com/resources/pdf/etd/LARGE_AREA_PMT_TPMH1286E.pdf, 2008. [Online; accessed Sept-2018].
- [68] P. Agnes et al. The electronics and data acquisition system for the DarkSide-50 veto detectors. *Journal of Instrumentation*, 11(12), 2016.
- [69] A. Brigatti, A. Ianni, P. Lombardi, G. Ranucci, and O.Ju. Smirnov. The photomultiplier tube testing facility for the borexino experiment at lngs. *Nuclear Instruments and Methods in Physics Research Section A: Accelerators, Spectrometers, Detectors and Associated Equipment*, 537(3):521 – 536, 2005.
- [70] B Caccianiga et al. A multiplexed optical-fiber system for the pmt calibration of the borexino experiment. *Nuclear Instruments and Methods in Physics Research Section A: Accelerators, Spectrometers, Detectors and Associated Equipment*, 496(2):353 – 361, 2003.
- [71] P. Agnes et al. CALIS - A CALibration Insertion System for the DarkSide-50 dark matter search experiment. *Journal of Instrumentation*, 12(12):T12004, 2017.
- [72] G. Bellini et al. Cosmic-muon flux and annual modulation in Borexino at 3800 m water-equivalent depth. *J. Cosmol. Astropart. Phys.*, 2012(05):15, 2012.

- [73] A. Empl, E. V. Hungerford, R. Jasim, and P. Mosteiro. A FLUKA study of underground cosmogenic neutron production. *Journal of Cosmology and Astroparticle Physics*, 2014(8), 2014.
- [74] G. Alimonti et al. A large-scale low-background liquid scintillation detector: The counting test facility at Gran Sasso. *Nuclear Instruments and Methods in Physics Research, Section A: Accelerators, Spectrometers, Detectors and Associated Equipment*, 406(3):411–426, 1998.
- [75] M. Janecek. Reflectivity Spectra for Commonly Used Reflectors. *IEEE Trans. Nucl. Sci.*, 59.
- [76] F.P. An et al. The muon system of the Daya Bay reactor antineutrino experiment. *Nuclear Instruments and Methods in Physics Research Section A: Accelerators, Spectrometers, Detectors and Associated Equipment*, 773:8 – 20, 2015.
- [77] G Alimonti et al.. A large-scale low-background liquid scintillation detector: the counting test facility at Gran Sasso. *Nuclear Instruments and Methods in Physics Research Section A: Accelerators, Spectrometers, Detectors and Associated Equipment*, 406(3):411 – 426, 1998.
- [78] Thorsten Gluesenkamp. Illustration of the Cherenkov effect. <https://bit.ly/2Ppm7yv>. Accessed: 2018-10-02.
- [79] P. Agnes et al. Simulation of argon response and light detection in the DarkSide-50 dual phase TPC. *Journal of Instrumentation*, 12(10), 2017.
- [80] Paolo Agnes. *Direct Search for Dark Matter with the DarkSide Experiment*. PhD thesis, APC, Paris, 2016.
- [81] P. Agnes et al. DarkSide-50 532-day dark matter search with low-radioactivity argon. *Phys. Rev. D*, 98:102006, Nov 2018.
- [82] C. E. Aalseth et al. Darksided-20k: A 20 tonne two-phase LAr TPC for direct dark matter detection at lngs. *The European Physical Journal Plus*, 133(3):131, Mar 2018.
- [83] Tadayoshi Doke, Akira Hitachi, Jun Kikuchi, Kimiaki Masuda, Hiroyuki Okada, and Eido Shibamura. Absolute scintillation yields in liquid argon and xenon for various particles. *Japanese Journal of Applied Physics*, 41(3R):1538, 2002.
- [84] M Szydagis et al. NEST: a comprehensive model for scintillation yield in liquid xenon. *Journal of Instrumentation*, 6(10):P10002, 2011.
- [85] J. Thomas and D. A. Imel. Recombination of electron-ion pairs in liquid argon and liquid xenon. *Phys. Rev. A*, 36:614–616, Jul 1987.
- [86] Tadayoshi Doke, Henry J. Crawford, Akira Hitachi, Jun Kikuchi, Peter J. Lindstrom, Kimiaki Masuda, Eido Shibamura, and Tan Takahashi. Let dependence of scintillation yields in liquid argon. *Nuclear Instruments and Methods in Physics Research Section A: Accelerators, Spectrometers, Detectors and Associated Equipment*, 269(1):291 – 296, 1988.

- [87] Chris Stanford. *Alphas and Surface Backgrounds in Liquid Argon Dark Matter Detectors*. PhD thesis, Princeton University, December 2017.
- [88] Xin Xiang. *Cherenkov Related Backgrounds in DarkSide-50 Experiment*. PhD thesis, Princeton University, 2018.
- [89] Guangyong Koh. *A Dark Matter Search With DarkSide-50*. PhD thesis, Princeton University, 2018.
- [90] B. Singh and J. A. Cameron. Nuclear Data Sheets for $A = 39$. *Nuclear Data Sheets*, 107:225–354, February 2006.
- [91] O. G. Ryajskaya and G. T. Zatsepin. Depth-intensity curve of nuclear events induced by muons. *International Cosmic Ray Conference*, 2:987, 1965.
- [92] A. Ferrari, P. R. Sala, A. Fasso, J. Ranft, Organisation Européenne, Pour La, Recherche Nuclaire, Alfredo Ferrari, Paola R. Sala, Alberto Fass, and Johannes Ranft. FLUKA: a multi-particle transport code. In *CERN 2005-10 (2005), INFN/TC 05/11, SLAC-R-773*.
- [93] T. T. Böhlen, F. Cerutti, M. P. W. Chin, A. Fassò, A. Ferrari, P. G. Ortega, A. Mairani, P. R. Sala, G. Smirnov, and V. Vlachoudis. The FLUKA Code: Developments and Challenges for High Energy and Medical Applications. *Nuclear Data Sheets*, 120:211–214, June 2014.
- [94] A. Capella, U. Sukhatme, C.-I. Tan, and J. Tran Thanh Van. Dual parton model. *Physics Reports*, 236(4):225 – 329, 1994.
- [95] R. J. Glauber and G. Matthiae. High-energy scattering of protons by nuclei. *Nucl. Phys.*, B21:135–157, 1970.
- [96] V. N. Gribov. Glauber corrections and the interaction between high-energy hadrons and nuclei. *Sov. Phys. JETP*, 29:483–487, 1969. [*Zh. Eksp. Teor. Fiz.*56,892(1969)].
- [97] A. Fasso et al. The Physics models of FLUKA: Status and recent developments. *eConf*, C0303241:MOMT005, 2003.
- [98] J. Ranft. Dual parton model at cosmic ray energies. *Phys. Rev. D*, 51:64–84, Jan 1995.
- [99] Heinz Sorge, Horst Stcker, and Walter Greiner. Relativistic quantum molecular dynamics approach to nuclear collisions at ultrarelativistic energies. *Nuclear Physics A*, 498:567 – 576, 1989.
- [100] H. Sorge. Flavor production in Pb (160A GeV) on Pb collisions: Effect of color ropes and hadronic rescattering. *Phys. Rev. C*, 52:3291–3314, Dec 1995.
- [101] I. Cervesato, E. Fabrici, E. Gadioli, E. Gadioli-Erba, and M. Galmarini. Light particle emission in Boltzmann master equation theory of pre-equilibrium reactions. *Phys. Rev.*, C45:2369–2378, 1992.

- [102] L.B. Bezrukov and E.V. Bugaev. Nucleon shadowing effects in photonuclear interactions. *Sov. J. Nucl. Phys. (Engl. Transl.); (United States)*.
- [103] M. Brugger, A. Ferrari, S. Roesler, and L. Ulrici. Validation of the fluka monte carlo code for predicting induced radioactivity at high-energy accelerators. *Nuclear Instruments and Methods in Physics Research Section A: Accelerators, Spectrometers, Detectors and Associated Equipment*, 562(2):814 – 818, 2006. Proceedings of the 7th International Conference on Accelerator Applications.
- [104] G. et al. Alimonti. The Borexino detector at the Laboratori Nazionali del Gran Sasso. *Nuclear Instruments and Methods in Physics Research, Section A: Accelerators, Spectrometers, Detectors and Associated Equipment*, 600(3):568–593, 2009.
- [105] S. Cecchini and M. Spurio. Atmospheric muons: experimental aspects. *Geoscientific Instrumentation, Methods and Data Systems Discussions*, 2:603–641, August 2012.
- [106] S. P. Ahlen et al. Muon astronomy with the MACRO detector. *Astrophys. J.*, 412:301–311, 1993.
- [107] Muon astronomy with the MACRO detector at Gran Sasso. *Nuclear Physics B (Proceedings Supplements)*, 28(1):385–388, 1992.
- [108] G. Bellini et al. Cosmogenic backgrounds in Borexino at 3800 m water-equivalent depth. *Journal of Cosmology and Astroparticle Physics*, 2013(8), 2013.
- [109] Giuseppe Battistoni, Annarita Margiotta, Silvia Muraro, and Maximiliano Sioli. Fluka as a new high energy cosmic ray generator. *Nuclear Instruments and Methods in Physics Research Section A: Accelerators, Spectrometers, Detectors and Associated Equipment*, 626-627:S191 – S192, 2011.
- [110] J. T. Hong et al. Multiple muon measurements with MACRO. In *8th International Symposium on Very High Energy Cosmic Ray Interactions (ISVHECRI 1994) Tokyo, Japan, July 24-30, 1994*, pages 711–722, 1994.
- [111] N. Agafonova et al. Measurement of the atmospheric muon charge ratio with the OPERA detector. *The European Physical Journal C*, 67(1):25–37, May 2010.
- [112] M. Ambrosio et al. Vertical muon intensity measured with macro at the gran sasso laboratory. *Phys. Rev. D*, 52:3793–3802, Oct 1995.
- [113] Riznia Jenifa Jasim. *Monte Carlo evaluation of the cosmogenic neutron background at Gran Sasso*. PhD thesis, University of Houston, January 2011.
- [114] Kevin B. McCarty. *The Borexino Nylon Film and the Third Counting Test Facility*. PhD thesis, Princeton University, 2006.
- [115] W. H. Lippincott, K. J. Coakley, D. Gastler, A. Hime, E. Kearns, D. N. McKinsey, J. A. Nikkel, and L. C. Stonehill. Scintillation time dependence and pulse shape discrimination in liquid argon. *Phys. Rev. C*, 78:035801, Sep 2008.
- [116] T. Alexander et al. Observation of the dependence on drift field of scintillation from nuclear recoils in liquid argon. *Phys. Rev. D*, 88:092006, Nov 2013.

- [117] H. Cao et al. Measurement of scintillation and ionization yield and scintillation pulse shape from nuclear recoils in liquid argon. *Phys. Rev. D*, 91:092007, May 2015.
- [118] D. V. Hinkley. On the ratio of two correlated normal random variables. *Biometrika*, 56(3):635–639, 1969.
- [119] Luca Pagani. *Direct dark matter detection with the DarkSide-50 experiment*. PhD thesis, Genoa U., 2017.
- [120] S. Yellin. Some ways of combining optimum interval upper limits. *arXiv:1105.2928*, May 2011.
- [121] E. Aprile et al. Dark matter results from 225 live days of XENON100 data. *Phys. Rev. Lett.*, 109:181301, Nov 2012.
- [122] X Xiao et al. Low-mass dark matter search results from full exposure of the PandaX-I experiment. *Phys. Rev. D*, 92:052004, Sep 2015.
- [123] R. Agnese et al. Improved WIMP-search reach of the CDMS-II germanium data. *Phys. Rev. D*, 92:072003, Oct 2015.
- [124] C. Amole et al. Dark matter search results from the PICO-2L C₃F₈ bubble chamber. *Phys. Rev. Lett.*, 114:231302, Jun 2015.
- [125] D. Y. Akimov et al. WIMP-nucleon cross-section results from the second science run of ZEPLIN-III. *Physics Letters B*, 709(1):14 – 20, 2012.
- [126] P Benetti et al. First results from a dark matter search with liquid argon at 87K in the gran sasso underground laboratory. *Astroparticle Physics*, 28(6):495 – 507, 2008.
- [127] Alissa Monte. *Alpha Radiation Studies and Related Backgrounds in the DarkSide-50 Detector*. PhD thesis, UMass Amherst, September 2018.
- [128] T. Johnson. Negative log likelihood s1 pattern rejector (DocDB 2105) [internal access], 2017.
- [129] Hao Qian. *Neutron Veto Efficiency of the DarkSide-50 Detector*. PhD thesis, Princeton University, 2018.
- [130] D. S. Akerib et al. Results from a search for dark matter in the complete lux exposure. *Phys. Rev. Lett.*, 118:021303, Jan 2017.
- [131] Xiangyi Cui et al. Dark matter results from 54-ton-day exposure of PandaX-II experiment. *Phys. Rev. Lett.*, 119:181302, Oct 2017.
- [132] P. Agnes et al. Low-Mass Dark Matter Search with the DarkSide-50 Experiment. *Phys. Rev. Lett.*, 121(8):081307, 2018.
- [133] Erin E. Ludert. *Detailed Characterization of Nuclear Recoil Pulse Shape Discrimination in the Darkside-50 Direct Dark Matter Experiment*. PhD thesis, University of Hawaii at Mnoa, 2017.

- [134] P. Agnes et al. Measurement of the liquid argon energy response to nuclear and electronic recoils. *Phys. Rev. D*, 97:112005, Jun 2018.
- [135] Fedor Bezrukov, Felix Kahlhoefer, and Manfred Lindner. Interplay between scintillation and ionization in liquid xenon dark matter searches. *Astroparticle Physics*, 35(3):119 – 127, 2011.
- [136] T. H. Joshi, S. Sangiorgio, A. Bernstein, M. Foxe, C. Hagmann, I. Jovanovic, K. Kazkaz, V. Mozin, E. B. Norman, S. V. Pereverzev, F. Rebassoo, and P. Sorensen. First measurement of the ionization yield of nuclear recoils in liquid argon. *Phys. Rev. Lett.*, 112:171303, May 2014.
- [137] Glen Cowan, Kyle Cranmer, Eilam Gross, and Ofer Vitells. Asymptotic formulae for likelihood-based tests of new physics. *The European Physical Journal C*, 71(2):1554, Feb 2011.
- [138] R. Agnese et al. Low-mass dark matter search with CDMSlite. *Phys. Rev. D*, 97:022002, Jan 2018.
- [139] L. Hehn et al. Improved EDELWEISS-III sensitivity for low-mass WIMPs using a profile likelihood approach. *The European Physical Journal C*, 76(10):548, Oct 2016.
- [140] E. Aprile et al. Low-mass dark matter search using ionization signals in XENON100. *Phys. Rev. D*, 94:092001, Nov 2016.
- [141] R. Agnese et al. Search for low-mass weakly interacting massive particles using voltage-assisted calorimetric ionization detection in the SuperCDMS experiment. *Phys. Rev. Lett.*, 112:041302, Jan 2014.
- [142] R. Agnese et al. Search for low-mass weakly interacting massive particles with SuperCDMS. *Phys. Rev. Lett.*, 112:241302, Jun 2014.
- [143] Andi Tan et al. Dark matter results from first 98.7 days of data from the PandaX-II experiment. *Phys. Rev. Lett.*, 117:121303, Sep 2016.
- [144] H. Jiang et al. Limits on light weakly interacting massive particles from the first 102.8 kg \times day data of the CDEX-10 experiment. *Phys. Rev. Lett.*, 120:241301, Jun 2018.
- [145] A. Aguilar-Arevalo et al. Search for low-mass WIMPs in a 0.6 kg day exposure of the DAMIC experiment at SNOLAB. *Phys. Rev. D*, 94:082006, Oct 2016.
- [146] G. Angloher et al. Results on light dark matter particles with a low-threshold CRESST-II detector. *The European Physical Journal C*, 76(1):25, Jan 2016.
- [147] C. Amole et al. Dark Matter Search Results from the PICO-60 C₃F₈ Bubble Chamber. *Phys. Rev. Lett.*, 118:251301, Jun 2017.
- [148] E. Behnke et al. Final results of the PICASSO dark matter search experiment. *Astroparticle Physics*, 90:85 – 92, 2017.

- [149] C. Savage, G. Gelmini, P. Gondolo, and K. Freese. Compatibility of DAMA/LIBRA dark matter detection with other searches. *Journal of Cosmology and Astroparticle Physics*, 2009(04):010, 2009.
- [150] C. E. Aalseth, P. S. Barbeau, J. Colaresi, J. I. Collar, J. Diaz Leon, J. E. Fast, N. E. Fields, T. W. Hossbach, A. Knecht, M. S. Kos, M. G. Marino, H. S. Miley, M. L. Miller, J. L. Orrell, and K. M. Yocum. CoGeNT: A search for low-mass dark matter using p -type point contact germanium detectors. *Phys. Rev. D*, 88:012002, Jul 2013.
- [151] G. Angloher et al. Results from 730 kg days of the CRESST-II dark matter search. *The European Physical Journal C*, 72(4):1971, Apr 2012.
- [152] R. Agnese et al. Silicon detector dark matter results from the final exposure of CDMS-II. *Phys. Rev. Lett.*, 111:251301, Dec 2013.
- [153] P. Agnes et al. Constraints on sub-GeV dark matter–electron scattering from the DarkSide-50 experiment. *Phys. Rev. Lett.*, 121:111303, Sep 2018.
- [154] S. Kubota, A. Nakamoto, T. Takahashi, S. Konno, T. Hamada, M. Miyajima, A. Hitachi, E. Shibamura, and T. Doke. Evidence of the existence of exciton states in liquid argon and exciton-enhanced ionization from xenon doping. *Phys. Rev. B*, 13:1649–1653, Feb 1976.
- [155] Rouven Essig, Tomer Volansky, and Tien-Tien Yu. New constraints and prospects for sub-GeV dark matter scattering off electrons in xenon. *Phys. Rev. D*, 96:043017, Aug 2017.
- [156] Y. Fukuda et al. Evidence for oscillation of atmospheric neutrinos. *Phys. Rev. Lett.*, 81:1562–1567, Aug 1998.
- [157] Q. R. Ahmad et al. Direct evidence for neutrino flavor transformation from neutral-current interactions in the sudbury neutrino observatory. *Phys. Rev. Lett.*, 89:011301, Jun 2002.
- [158] M. Agostini et al. Limit on the radiative neutrinoless double electron capture of ^{36}Ar from GERDA Phase I. *The European Physical Journal C*, 76(12):652, Nov 2016.
- [159] Alexander Merle. *The Mysteries of Leptons : New Physics and unexplained Phenomena*. PhD thesis, Ruperto-Carola University of Heidelberg, December 2009.
- [160] A. G. W. Cameron. Elemental and isotopic abundances of the volatile elements in the outer planets. *Space Science Reviews*, 14(3):392–400, Mar 1973.
- [161] M. J. Barlow, B. M. Swinyard, P. J. Owen, J. Cernicharo, H. L. Gomez, R. J. Ivison, O. Krause, T. L. Lim, M. Matsuura, S. Miller, G. Olofsson, and E. T. Polehampton. Detection of a noble gas molecular ion, $^{36}\text{ArH}^+$, in the crab nebula. *Science*, 342(6164):1343–1345, 2013.
- [162] H. O. Back. Low radioactivity argon for rare event searches. <https://indico.cern.ch/event/606690/contributions/2623442/attachments/1498273/2332413/UAr-TAUP2017-HenningBack.pdf>, 2017. [Online; accessed 19-Nov-2018].

- [163] Philippe Sarda, Thomas Staudacher, and Claude J. Allegre. $^{40}\text{Ar}:$ ^{36}Ar in MORB glasses: constraints on atmosphere and mantle evolution. *Earth and Planetary Science Letters*, 72(4):357 – 375, 1985.
- [164] F. Deppisch and H. Pas. Pinning down the mechanism of neutrinoless double beta decay with measurements in different nuclei. *Phys. Rev. Lett.*, 98:232501, 2007.
- [165] R. A. Johnson and D. W. Wichern. *Applied Multivariate Statistical Analysis*. Prentice-Hall, Inc., Upper Saddle River, NJ, USA, 1988.
- [166] Roger Barlow. Systematic errors: Facts and fictions. In *Advanced Statistical Techniques in Particle Physics. Proceedings, Conference, Durham, UK, March 18-22, 2002*, pages 134–144, 2002.
- [167] R.J. Crewther, P. Di Vecchia, G. Veneziano, and E. Witten. Chiral estimate of the electric dipole moment of the neutron in quantum chromodynamics. *Physics Letters B*, 88(1):123 – 127, 1979.
- [168] C. A. Baker, D. D. Doyle, P. Geltenbort, K. Green, M. G. D. van der Grinten, P. G. Harris, P. Iaydjiev, S. N. Ivanov, D. J. R. May, J. M. Pendlebury, J. D. Richardson, D. Shiers, and K. F. Smith. Improved experimental limit on the electric dipole moment of the neutron. *Phys. Rev. Lett.*, 97:131801, Sep 2006.
- [169] Steven Weinberg. A new light boson? *Phys. Rev. Lett.*, 40:223–226, Jan 1978.
- [170] F. Wilczek. Problem of strong P and T invariance in the presence of instantons. *Phys. Rev. Lett.*, 40:279–282, Jan 1978.
- [171] R. D. Peccei and Helen R. Quinn. CP conservation in the presence of pseudoparticles. *Phys. Rev. Lett.*, 38:1440–1443, Jun 1977.
- [172] M.A. Shifman, A.I. Vainshtein, and V.I. Zakharov. Can confinement ensure natural CP invariance of strong interactions? *Nuclear Physics B*, 166(3):493 – 506, 1980.
- [173] Olivier Wantz and E. P S Shellard. Axion cosmology revisited. *Physical Review D - Particles, Fields, Gravitation and Cosmology*, 82(12), 2010.
- [174] J. Ruz, J. K. Vogel, and M. J. Pivovarov. Recent Constraints on axion-photon and axion-electron Coupling with the CAST Experiment. In *Physics Procedia*, volume 61, pages 153–156, 2015.
- [175] K. Barth et al. CAST constraints on the axion-electron coupling. *Journal of Cosmology and Astroparticle Physics*, 2013(5), 2013.
- [176] G. 't Hooft. Computation of the quantum effects due to a four-dimensional pseudoparticle. *Phys. Rev. D*, 14:3432–3450, Dec 1976.
- [177] Jihn E. Kim. Weak-interaction singlet and strong CP invariance. *Phys. Rev. Lett.*, 43:103–107, Jul 1979.
- [178] M.A. Shifman, A.I. Vainshtein, and V.I. Zakharov. Can confinement ensure natural CP invariance of strong interactions? *Nuclear Physics B*, 166(3):493 – 506, 1980.

- [179] Michael Dine, Willy Fischler, and Mark Srednicki. A simple solution to the strong cp problem with a harmless axion. *Physics Letters B*, 104(3):199 – 202, 1981.
- [180] A. Derevianko, V. A. Dzuba, V. V. Flambaum, and M. Pospelov. Axio-electric effect. *Phys. Rev.*, D82:065006, 2010.
- [181] Savas Dimopoulos, Joshua Frieman, Bryan W. Lynn, and Glenn D. Starkman. Axio-recombination: A new mechanism for stellar axion production. *Physics Letters B*, 179(3):223 – 227, 1986.
- [182] Maxim Pospelov, Adam Ritz, and Mikhail Voloshin. Bosonic super-WIMPs as keV-scale dark matter. *Phys. Rev. D*, 78:115012, Dec 2008.
- [183] Paolo Beltrame. First axion results from the XENON100 experiment. <http://www.physics.purdue.edu/darkmatters/xenon1t/?tag=axions>. Accessed: 2010-09-30.
- [184] Javier Redondo. Solar axion flux from the axion-electron coupling. *Journal of Cosmology and Astroparticle Physics*, 2013(12), 2013.
- [185] F. T. Avignone, III, R. J. Creswick, J. D. Vergados, P. Pirinen, P. C. Srivastava, and J. Suhonen. Estimating the flux of the 14.4 keV solar axions. *Journal of Cosmology and Astroparticle Physics*, 1:021, January 2018.
- [186] A. V. Derbin, A. S. Kayunov, V. V. Muratova, D. A. Semenov, and E. V. Unzhakov. Constraints on the axion-electron coupling for solar axions produced by a compton process and bremsstrahlung. *Phys. Rev. D*, 83:023505, Jan 2011.
- [187] D Franco et al. Background model for axions (DocDB 2751) [internal access], 2018.
- [188] M. Foxe, C. Hagmann, I. Jovanovic, A. Bernstein, K. Kazkaz, V. Mozin, S.V. Pereverzev, S. Sangiorgio, and P. Sorensen. Low-energy (<10keV) electron ionization and recombination model for a liquid argon detector. *Nuclear Instruments and Methods in Physics Research Section A: Accelerators, Spectrometers, Detectors and Associated Equipment*, 771:88 – 92, 2015.
- [189] V. I. Barsanov et al. Artificial neutrino source based on the ^{37}Ar isotope. *Physics of Atomic Nuclei*, 70(2):300–310, Feb 2007.
- [190] L. Moneta, K. Cranmer, G. Schott, and W. Verkerke. The RooStats project. In *Proceedings of the 13th International Workshop on Advanced Computing and Analysis Techniques in Physics Research. February 22-27, 2010, Jaipur, India*. <http://acat2010.cern.ch/>. Published online at “<http://pos.sissa.it/cgi-bin/reader/conf.cgi?confid=93>” & <http://pos.sissa.it/cgi-bin/reader/conf.cgi?confid=93>, id.57, page 57, 2010.
- [191] Kyle Cranmer, George Lewis, Lorenzo Moneta, Akira Shibata, and Wouter Verkerke. HistFactory: A tool for creating statistical models for use with RooFit and RooStats. Technical Report CERN-OPEN-2012-016, New York U., New York, Jan 2012.
- [192] D. S. Akerib et al. First searches for axions and axion-like particles with the LUX experiment. *Phys. Rev. Lett.*, 118:261301, Jun 2017.

- [193] D Franco et al. Improving the background model (DocDB 2754) [internal access], 2018.
- [194] X. Mougeot and C. Bisch. Consistent calculation of the screening and exchange effects in allowed β^- transitions. *Phys. Rev. A*, 90:012501, Jul 2014.
- [195] Leendert Hayen, Nathal Severijns, Kazimierz Bodek, Dagmara Rozpedzik, and Xavier Mougeot. High precision analytical description of the allowed β spectrum shape. *Rev. Mod. Phys.*, 90:015008, Mar 2018.
- [196] B. Abi et al. The Single-Phase ProtoDUNE Technical Design Report. *arXiv:1706.07081*, June 2017.
- [197] R. Acciarri et al. Long-Baseline Neutrino Facility (LBNF) and Deep Underground Neutrino Experiment (DUNE) Conceptual Design Report Volume 1: The LBNF and DUNE Projects. *arXiv:1601.05471*, January 2016.
- [198] DarkSide Collaboration. DarkSide-20k Progress Report for the XLIX LNGS Scientific Committee meeting, March 26-27 [internal access], 2018.
- [199] C. E. Aalseth et al. Cryogenic characterization of FBK RGB-HD SiPMs. *Journal of Instrumentation*, 12(09):P09030, 2017.
- [200] J. Billard, E. Figueroa-Feliciano, and L. Strigari. Implication of neutrino backgrounds on the reach of next generation dark matter direct detection experiments. *Phys. Rev. D*, 89:023524, Jan 2014.
- [201] Giuliana Fiorillo. Darkside-20k and the future liquid argon dark matter program. <https://indico.cern.ch/event/653314/contributions/2825769/attachments/1606239/2548583/Fiorillo-DM2018.pdf>, 2018. [Online; accessed 23-Feb-2018].
- [202] M. Antonello et al. The SABRE project and the SABRE PoP. *arXiv:1806.09340*, June 2018.